# Improving the position resolution of Highly Segmented HPGe Detectors using Pulse Shape Analysis Methods

Thesis submitted in accordance with the requirements of
the University of Liverpool for the degree of Doctor in Philosophy

by

**Martina Descovich**

Oliver Lodge Laboratory

November 2002

*A mio padre*

εἰκῇ κεχυμένων ὁ κάλλιστος κόσμος

*Da cose a caso sparse la natura bellissima del cosmo*
(Eraclito, fragm. 124)

## Acknowledgement

This work would have been never possible without the help of many people, now I would like to take the opportunity to thank them all. I apologise in advance if I miss somebody out.

I start by thanking my supervisor and Head of Department Prof. Paul Nolan for allowing me the opportunity to carry on this research at the University of Liverpool. I would also like to thank Prof. Dario Bisello for encouraging me to pursue a Ph.D. I am in deep gratitude to Andy Boston for his essential help throughout the entire course of this work and for his time in proof reading this thesis. I'd also like to thank him for having been such a good friend and guide over the last three years.

I would like to thank the whole nuclear physics group (both past and present), the students, especially Neil, Helen, Chris, Jenny, Sebastian and Gerard, the postdocs and staff members, in particular, John Cresswell, Janet Sampson, Eddie Paul, Rodi Herzberg, John Hemingway, Robert Page, Jim Thornhill and Terry Burns. I cannot express thanks enough to Hannah for her sincere friendship and her constant support both at work and in everyday life.

I take this opportunity to thank all my colleagues in the TMR network, the UK $\gamma$-ray tracking collaboration at the University of Surrey and at the Daresbury Laboratory, the Euroball group at the GSI and the GRETA collaboration in Berkeley. Special thanks go to Dino Bazzacco, Thorsten Kröll, Franco Camera and Oliver Wieland. I would also like to thank Jose Javier for all the shared problems.

I would like to thank all the friend I have made during the course of my Ph.D. In particular, I would like to thank Pascale (I have learnt a lot from living with you), Joanna and Stefano (tra italiani e' un'altra cosa), Nieves, Shara, Lavinia, Liam and Andrea.

Un grazie di cuore merita Luca con cui ho trascorso i piu' bei weekend di questi tre anni.

Prima di concludere i miei ringraziamenti vorrei ricordare la mia famiglia e i miei amici veneziani per l'affetto e il supporto sempre dimostratomi. In modo particolare vorrei ringraziare Paola, Carlotta, Pier, Angelo ed infine Elisabetta, per la fantastica amicizia che ci lega da piu' di dodici anni.

# Abstract

This work presents an approach for determining the interaction position of $\gamma$ rays in highly segmented HPGe detectors. A precise knowledge of the interaction position enables the effective granularity of the detector to be substantially improved and a calibration of the detector response as a function of position to be performed. An improved position resolution is fundamental for the development of arrays of $\gamma$ ray tracking detectors.

The performance of a highly segmented germanium detector (TIGRE) has been characterised. TIGRE consists of a large volume coaxial high-purity n-type germanium crystal with a 24-fold segmented outer contact. Due to its high granularity and its fast electronics, TIGRE represents a unique example of a tracking detector, having low noise output signals, fast rise time and good energy resolution. In order to calibrate the response of the detector as a function of the interaction position, a dedicated scanning apparatus has been developed and the front surface of the detector has been scanned.

The method developed for position determination is based on the digital analysis of the preamplifier signal, whose features are position dependent. A two-dimensional position resolution is accomplished by combining the radial position information, contained in the rise time of the pulse shape leading edge, with the azimuthal position information, carried by the magnitude of the transient charge signals induced in the spectator segments. Utilising this method, a position resolution of 0.6 mm, both radially and along the azimuthal direction, can be achieved in the most sensitive part of the detector.

# Contents


**1 Introduction** **1**

**2 Principles of radiation detection** **5**

2.1 Introduction . . . . . 5

2.2 The interaction of photons with matter . . . . . 5

2.2.1 Photoelectric effect . . . . . 6

2.2.2 Compton scattering . . . . . 6

2.2.3 Pair production . . . . . 8

2.2.4 Attenuation coefficients . . . . . 9

2.3 Production of charge carriers . . . . . 10

2.4 The choice of a $\gamma$-ray detector material . . . . . 11

2.5 Properties of germanium . . . . . 12

2.5.1 The $p-n$ Junction . . . . . 15

2.5.2 Detector geometry . . . . . 17

2.5.3 Electric field calculation . . . . . 19

2.6 The signal generation process . . . . . 20

2.6.1 The influence of the anisotropic drift velocity on the charge collection process . . . . . 23

2.7 Detector operational characteristics . . . . . 26

2.7.1 Preamplifier . . . . . 26

2.7.2 Noise performance . . . . . 28

2.7.3 Energy resolution . . . . . 29

2.7.4 Efficiency . . . . . 32

2.7.5 Time resolution . . . 32
2.8 Compton suppressed detectors . . . 33
2.9 Multi-element detectors . . . 33
2.9.1 Composite and segmented detector capabilities . . . 35

**3 Gamma-ray tracking detector arrays 39**
3.1 The development of detectors for nuclear spectroscopy . . . 39
3.2 The observational limit . . . 40
3.3 The concept of $\gamma$-ray tracking . . . 42

**4 Experimental measurements 49**
4.1 Experimental setup . . . 49
4.1.1 The 6×4 prototype detector . . . 49
4.1.2 Digital signal processing system . . . 51
4.1.3 The scanning apparatus . . . 53
4.2 Detector performance . . . 58
4.2.1 Energy resolution measurements . . . 59
4.2.2 Efficiency measurements . . . 60
4.2.3 Preamplifier response . . . 60
4.2.4 Noise evaluation . . . 62
4.3 The scan . . . 65
4.3.1 Experimental Details . . . 65
4.3.2 The detector response to radiation events . . . 65
4.3.3 Position of the segment boundaries . . . 75
4.3.4 Scattering probability between adjacent segments . . . 82

**5 The concept of pulse shape analysis 84**
5.1 Basic principle . . . 85
5.2 The method . . . 88
5.2.1 Example pulse shapes . . . 90
5.3 The algorithm . . . 90
5.3.1 Pulse processing routine . . . 93
5.3.2 Current signals for position determination . . . 99

5.4 Position resolution . . . . . 100
5.4.1 Intrinsic limits . . . . . 103
5.5 Energy information . . . . . 104
5.6 Position information . . . . . 107
5.6.1 T30, T60 and T90 distributions . . . . . 107
5.6.2 Analysis of the current pulses . . . . . 122

**6 Conclusions** **133**
6.1 Future work . . . . . 134

**A Monte Carlo simulation** **136**
A.1 Characteristics of photon interaction . . . . . 137
A.1.1 Fold distributions . . . . . 138
A.1.2 Energy distribution . . . . . 139
A.2 Comparison with the experimental measurements . . . . . 144

# List of Figures

1.1 Map of the bound nuclear system as a function of the proton number Z and the neutron number N [Dob02]. The black points forming the "valley of stability" are the stable nuclei. By adding either protons or neutrons, one moves away from the valley of stability towards the drip lines, where the nuclei become unbound. The yellow points represent unstable nuclei that are known experimentally. The green points indicate radioactive nuclei with very large or very small N/Z ratios that have not yet been accessed. While the proton drip line has been investigated experimentally up to Z=83, the neutron drip line has been predicted, on the basis of nuclear models, only for the lightest nuclei. Of particular interest are neutron-rich nuclei towards the neutron drip line, proton-rich nuclei at and beyond the proton drip line and the extension of the N=Z line, since they provide a tool to investigate the origin and evolution of nuclear matter in the universe. These nuclei known as "exotic nuclei" can only be produced in reactions induced by radioactive ion beams. 2

2.1 A schematic sketch of the photoelectric effect. . . . . 6

2.2 Quantities involved in a Compton scattering interaction. The $\gamma$ ray transfers part of its energy to an atomic electron which, in turn, releases that energy in the Ge crystal. 7

2.3 Schematic sketch of pair production interaction. . . . . 8

2.4 The relative importance of the three major interaction mechanisms. The lines show the values of Z and $h\nu$ for which the two neighbouring effects are equal. . . . . 9

2.5 Energy level diagrams for a metal, a semiconductor and an insulator. Even at T=0 K, metals have partially occupied bands (shaded). For semiconductors and insulators the Fermi level lies between the occupied valence band and the unoccupied conduction band. . . . . 12

2.6 Crystal structure of germanium showing the tetrahedral bonding and the lattice vector, $a_{1,2,3}$, (top) and the lattice planes (bottom), labelled by Miller indices. . . 13

2.7 Schematic representation of a $p-n$ junction in thermal equilibrium: (a) Semiconductor crystal, $p$-type on one side and $n$-type on the other side. (b) Band scheme in the imaginary case of total decoupling of the two sides. $E_C$ and $E_V$ indicates the bottom of the conduction and the top of the valence band, $E_A$ and $E_D$ represent the ground states of the acceptors and donors; $E_F$ is the Fermi level. (c) Band scheme of the $p-n$ junction when the two sides are in thermal equilibrium with one other. The transition from the $p$ to the $n$ region is assumed to be abrupt. The position of the conduction and valence edges are denoted $E^n_{C,V}$ on the $n$-side and $E^p_{C,V}$ on the $p$-side. In the region of the junction an electrostatic potential is induced. (d) The fixed space charge $\rho(x)$ in the region of the junction due to the ionised impurities. This region is free from charge carriers and therefore is also known as the *depletion region* [Iba95b]. . . . . 16

2.8 Schematic illustration of a planar $n$-type detector; the $n^+$ contact is lithium drifted and $p^+$ one is boron implanted. The secondary charge carriers produced in the depleted region, instead of recombining, drift towards the electrodes, the electrons towards the anode and the holes toward the cathode. . . . . 18

2.9 Cross section and front view of a $n$-type coaxial closed-ended bulletised germanium detector; the $n^+$ lithium drifted and $p^+$ boron implanted contacts are indicated. . 19

2.10 (a) Determination of the induced current by the weighting field concept, illustrated on a planar multielectrode strip configuration. The weighting field is defined conceptually as the field for unity potential on the sensing electrode S (switch in position W) and zero potential on all other electrodes. In actual operation, the sensing electrode is connected to a charge amplifier and a uniform operating field is applied to the detector by connecting the opposite electrode to a voltage source (switch in position M). The weighting field calculated numerically for this case is shown as a plot of equipotential lines in (b) for the left half of the electrode structure in (a). Two examples of charge transit from top to bottom are shown. The induced current pulse shapes, resulting from Eq. 2.34 for a localised charge moving at a constant velocity, are shown at the bottom of the figure. Charge $q$ traversing the full distance between the electrodes along line 1 is observed as $Q = -q$, while the current decreases with distance from electrode 1, as the electrostatic coupling decreases. For a charge moving along line 2, the induced charge is zero if the measurement time is longer than the transit time. For a short measurement time a net induced charge is observed (the induced current pulse shape is bipolar, since the weighting-field direction changes along the path). . . . . 22

2.11 Calculated band-structure of Ge in the reciprocal space representation. The band gap, $E_g$, is determined by states with different $\vec{k}$ [Sin01]. . . . . 23

2.12 Experimental field dependences of the electron drift velocity in germanium along the $\langle 111 \rangle$ and $\langle 100 \rangle$ directions at a temperature of 80 K and the simulated drift velocity for a field oriented along the $\langle 110 \rangle$ direction (taken from [Aga01].) . . . . . 24

2.13 Charge carrier trajectories in a closed-ended HPGe detector, from interactions of $\gamma$-ray quanta in the front part (A) and in the coaxial part (B) of the Ge detector. The upper drawing shows a full spatial representation and the lower drawings show front views [Mih00]. . . . . 25

2.14 Simplified diagram of a resistive feedback charge sensitive preamplifier configuration. The output pulse amplitude is proportional the charge produced by the $\gamma$-ray interaction. The time constant $R_f C_f$ determines the decay rate of tail of the output pulse [Kno00b]. . . . . 26

2.15 Sketch of a preamplifier signal consisting of a fast leading edge and a slow exponential tail. . . . . 27
2.16 Reference system describing the direction of the $\gamma$-ray emission with respect to the front face of the detector. The position of the $\gamma$ interaction $(r_\gamma, \varphi_\gamma)$ is defined in cylindrical coordinates. . . . . 31
2.17 A schematic diagram of a Compton suppressed detector, showing a germanium crystal inside its BGO suppression shield. The shield suppresses the Compton scattered $\gamma$ rays that escape from the germanium and also acts as a collimation system, to prevent the scattering of $\gamma$ rays from a Ge detector to its neighbor. . . . . 33
2.18 Un-suppressed and suppressed $^{60}$Co spectra, measured with a standard HPGe detector. In the insert, the y-axis has been rescaled to show the detail of the background, while the full photopeak intensity relative to the background indicates the overall quality of the spectrum. . . . . 34
2.19 Schematic picture of the 16-fold Clover detector. The peculiarity of this detector is that is both composite and segmented. . . . . 35
2.20 Schematic front face of original Clover and segmented Exogam Clover. The segmented detector enables Compton scattered (a) and multiple hits events (b) to be distinguished. . . . . 37
2.21 Advantages in using segmented detectors as Compton polarimeter. . . . . 37

3.1 Observational limit for various values of the total photopeak efficiency and resolving power as a function of the fold. The observational limit for two existing arrays, Nordball and Euroball, is compared to the value predicted for a new array based on the concept of $\gamma$-ray tracking (taken from [Mih00b]). . . . . 41
3.2 Cross-section of the Euroball array compared to a germanium Shell built from 120 closely packed detectors. . . . . 43
3.3 The 36-fold segmented, encapsulated Ge detector, as planned for AGATA. . . . . 44
3.4 The geometrical configurations proposed for the GRETA (left) and AGATA (right) arrays. . . . . 45
3.5 A schematic illustration of the scattering path of a $\gamma$ ray in the detector material. 47

4.1 Photographs of the 6×4 prototype detector: the detector complete with the aluminium cryostat housing the crystal, the preamplifier board and the cryostat (left); the germanium crystal with the electrical segmentation pattern (right). . . . . 50
4.2 Geometry of the 6×4 prototype detector. . . . . 50
4.3 A block diagram representing the components of a digital signal processing chain, compared to the conventional analogue electronics solution. In the analogue electronics approach, the energy is extracted by means of a shaping amplifier and the time is obtained through a timing filter amplifier (TFA) and a constant fraction discriminator (CFD). In the digital approach, the preamplifier signal is digitized using FADC units; the data are processed by means of a pulse shape analysis (PSA) routine. The information provided is the input to a $\gamma$-ray tracking algorithm (GRT). 52
4.4 Schematic view of the scanning apparatus. . . . . 54
4.5 The geometry of the heavy metal collimator (left); the number of detected $\gamma$ rays as a function of the distance form the centre of the collimator (right). . . . . 55
4.6 Block diagram of a cM62 card, showing two channels provided by an AD40 module. 56
4.7 Schematic view of the data acquisition system. . . . . 56
4.8 Energy resolution results for the 24 position channels of the 6×4-fold detector at 122 keV and 1332 keV. The measurements have been taken by using a shaping time constant of 6 $\mu$s on the spectroscopy amplifier. . . . . 59
4.9 Relative efficiency curve as a function of the $\gamma$-ray energy. . . . . 62
4.10 The centre contact preamplifier response to a precision pulses generator digitized with a fast scope having a sampling frequency of 1 GHz. . . . . 63
4.11 Noise signals from a typical outer contact preamplifier, digitized with a 12 bit dynamic range FADC at a sampling rate of 100 MHz (top), its power spectrum (middle) and its integrated power(bottom). . . . . 64
4.12 Sensitivity map of the 6×4 detector to full energy events. The top part shows the number of 662 keV events as a function of the source position in a 3D-surface map representation, while the bottom part shows a 2D-contour map, where the number of counts is given by the colour scheme. . . . . 67

4.13 Energy spectra measured from the centre contact (left) and from typical outer contact signals, namely A1, B1, C1, D1. The narrow and the wide gate widths are indicated. The low energy tail of the full energy peak from A1, D1 and from the centre contact signals can be attributed to incomplete charge collection. . . . . 68

4.14 Maps of the segment sensitivity for slice A (top left), slice B (top right), slice C (bottom left) and slice D (bottom right). The photopeak events were selected using a narrow energy gate on the 662 keV $\gamma$-ray line from the centre contact and a wide energy gate on the 662 keV $\gamma$-ray line from the outer contacts. The white arrows indicate the probable crystallographic directions labelled by the Miller indices. . . 70

4.15 Maps of the segment sensitivity for slice A (top left), slice B (top right), slice C (bottom left) and slice D (bottom right). The photopeak events were selected using a wide energy gate both on the centre and on the outer contacts. The white arrows indicate the probable crystallographic directions labelled by the Miller indices. . . 71

4.16 Maps of the segment sensitivity for slice A (top left), slice B (top right), slice C (bottom left) and slice D (bottom right). The photopeak events were selected using a wide energy gate on the centre and a narrow energy gate on the outer contacts. The white arrows indicate the probable crystallographic directions labelled by the Miller indices. . . . . 72

4.17 Geometry of slice D. For technical reasons, a layer of 9 mm of "dead" germanium is placed at the back of the detector: the centre electrode is 9 mm longer than the sum of the length of the outer electrodes. . . . . 73

4.18 Maps of the Compton scattering sensitivity for slice A (top left), slice B (top right), slice C (bottom left) and slice D (bottom right). The number of full-energy events involving an interaction in more than one segment has been plotted as a function of the collimator position. The white arrows indicate the probable crystallographic directions labelled by the Miller indices. . . . . 74

4.19 Frequency distribution of the amplitude of the transient charge signal measured as the absolute maximum of a typical outer contact signal. The amplitude values are expressed in arbitrary units, because no calibration or gain matching procedures have been applied to the data. The threshold defining an image charge as large or small is indicated. . . . . 75

4.20 Photopeak efficiency map at different depths in slice A. Events occurring at different depths were selected using the amplitude of transient charge signals induced in slice B: a small image charge induced in the B-contact corresponds to an interaction occurring in the front part of slice A, on the contrary, a large image charge corresponds to an interaction occurring in the back part of slice A, close to the boundary with B. 76
4.21 Compton scattering efficiency map in the back part (left) and in the front part (right) of the slice A. . . . . 77
4.22 Photopeak efficiency map at two depths in slice B: near slice C selecting large image charges in the C-contacts (top left) or small image charges in the A-contacts (top right), and near slice A selecting large image charges in the A-contacts (bottom left) or small image charges in the C-contacts (bottom right). . . . . 78
4.23 Photopeak efficiency map at two depths in slice C: near slice D selecting large image charges in the D-contacts (top left) or small image charges in the B-contacts (top right), and near slice B selecting large image charges in the B-contacts (bottom left) or small image charges in the D-contacts (bottom right). . . . . 79
4.24 Photopeak efficiency map at two depths in slice D: near slice C selecting large image charges in the C-contacts (left) and at the back selecting small image charges in the C-contacts (right). . . . . 80
4.25 Four known positions of the scanning table (right) and the corresponding hit-pattern spectra (left). . . . . 80
4.26 Photopeak efficiency map of segment A1 (top left), B1 (top right), C1 (bottom left) and D1 (bottom right). The front part of segment D1 is placed at a distance of 6 cm from the collimator. . . . . 81
4.27 Scattering profile for fold-2 events involving segments A2-A3 (top left), A3-A4 (top right), B2-B3 (bottom left), B3-B4 (bottom right). . . . . 82
4.28 Scattering profile for fold-3 events involving segments A1-A2-A3 (top left), A3-A4-A5 (top right), B1-B2-B3 (bottom left), B3-B4-B5 (bottom right). . . . . 83

5.1 A schematic illustration of the leading edge of the centre contact preamplifier signal for three different interaction positions and the corresponding transient charge signals induced in the spectator segment. . . . . 85

5.2 The charge (top) and current (bottom) preamplifier signals with the parameters used in the analysis. . . . . 88
5.3 A simulation of the scattering path of the $\gamma$ ray in the detector volume, produced with the MCNP code [Mcn94] (left). A schematic front view of the detector, the segment hit by the $\gamma$ ray and the transient charge signal induced in two adjacent segments, called *left* and *right*, are indicated (right). . . . . 89
5.4 Examples of charge signals corresponding to the three different interaction positions. The figure number (1), (2) and (3) corresponds to positions (1), (2) and (3), respectively. For each interaction position, the real charge signal from contact B3, corresponding to a fully absorbed $\gamma$ ray, and the respective transient charge signal induced on the nine adjacent segments, are shown. The preamplifier pulses are displayed as digitized by the FADCs, the sampling unit corresponds to 25 ns. A typical amplitude of a 662 keV $\gamma$ ray is 800 mV. . . . . 91
5.5 Example of current signals obtained as time derivatives of the charge signals for position (1) shown in Fig. 5.4. . . . . 92
5.6 Flow chart of the pulse shape analysis algorithms. . . . . 93
5.7 Example of a pulse shape digitized at 100 MHz. The effect of the data points interpolation is shown. . . . . 94
5.8 Pulses from the centre contact digitized with the 100 MHz card (one sample every 10 ns) and from an typical outer segment digitized with the 40 MHz card (one sample every 25 ns) are presented in the top left and bottom left part, respectively. The same pulses after smoothing have a sampling interval of 2 ns and 5 ns, respectively; they are presented in the top right and bottom right part. . . . . 95
5.9 The original charge signal measured from a typical outer contact preamplifier (at 40 MHz) and the charge signal obtained following the application of the MWD routine. The MWD works almost as a trapezoidal filter; the total charge deposited by the $\gamma$-ray interaction is calculated as the average value between the start and the end of the flat top of the deconvolved pulse. In this example, a window of 420 data points (corresponding to a time window of 10.5 $\mu$s) has been used in the deconvolution step. 97

5.10 Example of current signal calculated utilising the parabolic fit method. The parabolic function was calculated using three (left) and twenty seven (right) data points in the fit. . . . . 99
5.11 Comparison between the current pulse shape calculated using the parabolic fit (solid line) and the time derivative (dashed line) routine, for the centre (left) and for the outer contact B3 (right). The two methods provide a very similar result for the leading edge of the pulse, but the parabolic fit method helps in reducing the noise oscillations in the baseline (zoom). . . . . 100
5.12 Measured set of charge pulses from the inner contact signal, digitized at 100 MHz, at three different interaction positions: close to the centre (top left), at intermediate radius (top middle) and close to the outside (top right). The averaged signal is shown for each position. In the bottom part of the plot the corresponding current signal are shown. . . . . 102
5.13 As above, but the set of pulses have been measured from a typical outer contact, digitized at 40 MHz. . . . . 102
5.14 A typical energy spectrum obtained from contact B3 using a deconvolution window of 11.25 $\mu$s. . . . . 105
5.15 FWHM of the 662 keV peak, measured by using the MWD method from a typical outer contact signal (B3), as a function of the width of the deconvolution window. A window of $\sim$8 $\mu$s is required in order to obtain good energy resolution. . . . . 105
5.16 Plot of the FWHM as a function of the number of smoothing points used in the parabolic fit algorithm. The best energy resolution achieved corresponds to 27 fitting points. The errors on energy resolution measurements are typically $\leq$5 %. . . . . 106

5.17 Distribution of T30 (top left), T60 (top right) and T90 (bottom right) values, measured on the centre contact signal, as a function of the radial position of the interaction. Full energy interactions occurring in any segment of slice B of the detector have been considered. The colour scale indicates the number of times that the same value has been measured. The frequency distributions have been normalised for the solid angle. The higher number of counts at mid radii (yellow blob in the plot) is statistical: the photopeak efficiency is higher in this part of the detector and decreases towards the centre and towards the edge. The T30 distribution decreases as the interaction radius increases, until it reaches a saturation value; the T60 and T90 distributions present the characteristic V-shape, with minimum at intermediate radii. The scale of the number of counts is reduced following the normalisation. . . 109

5.18 T30 distributions as a function of the radial position of the interaction, measured from outer contact B3 (left) and C3 (right). The frequency distributions have been normalised for the solid angle. . . . . 110

5.19 T90 distributions as a function of the radial position of the interaction, measured from contact B3 (left) and C3 (right). The frequency distribution has been normalised for the solid angle. . . . . 110

5.20 These plots show the T30 (left) and T90 (middle) distribution as a function of the radial position of the interaction, measured from contact A3, and the schematic electric field distribution in the front slice of the detector (right). . . . . 111

5.21 These plots show the T30 (left) and T90 (middle) distribution as a function of the radial position of the interaction, measured from contact D3, and the schematic electric field distribution in the back slice of the detector (right). . . . . 111

5.22 The T30 (left) and T90 (right) distribution at five different radial distances, namely 8 mm, 11 mm, 16 mm 21 mm and 28 mm, from the surface of the centre contact. The rise time values have been measured from the centre contact signal, in correspondence to photopeak events in any of the segments of slice B. All the data from the fine scan have been considered in the analysis. . . . . 112

5.23 These plots show the T30 distribution measured from outer contact B3 (left) and C3 (right), at five different radial distance, namely 8 mm, 11 mm, 16 mm, 21 mm and 28 mm, from the surface of the centre contact. Only photopeak events have been considered in the analysis. . . . . 113

5.24 These plots show the T90 distribution measured from outer contact B3 (left) and C3 (right), at five different radial distance, namely 8 mm, 11 mm, 16 mm, 21 mm and 28 mm, from the surface of the centre contact. Only photopeak events have been considered in the analysis. . . . . 113

5.25 The plots show T30 (left) and T90 (right) centre contact values as a function of the radial position. The rise time values have been calculated as the centroid of the rise time distributions obtained by taking slices, at given radii, of the 2D-plots shown in Fig. 5.17. The errors have been estimated, point by point, on the basis of the spread of the rise time values at each given radius (see Fig. 5.22). . . . . 114

5.26 The plots show T30 (left) and T90 (right) outer contact (B3) values as a function of the radial position. The rise time values have been calculated as the centroid of the rise time distributions obtained by taking slices, at given radii, of the the 2D-plot shown in figures 5.18 and 5.19. The errors have been estimated, point by point, on the basis of the spread of the rise time values at each given radius (see figures 5.23 and 5.24). . . . . 115

5.27 T30 versus T90 values, calculated for 100 pulse shapes at the known collimator radial distance of 27 mm. The pulse shapes were measured from the centre contact signal. For the 100 pulse shapes, the average T90 value is 194.77±2.57 ns, the average T30 value is 47.97±2.62, where the errors have been extracted from the fit ($\sigma_y$). . . . . 117

5.28 For the 100 pulse shapes, the radial position of the interaction from the T30 fit has been plotted versus that from the T90 fit, for $r$ >19 mm. The errors have been extracted from equation 5.22. . . . . 117

5.29 Polar plots showing the rise time T30 (top), T60 (middle) and T90 (bottom) as a function of the position of the scanning table. The results refer to $\gamma$-ray events fully absorbed within a single segment and measured from the centre contact signal. The units of the colour scale are nanoseconds. . . . . 119

5.30 T30 polar plots corresponding to photopeak events in slice A (top left), slice B (top right), slice C (bottom left) and slice D (bottom right). The T30 rise time values have been measured from the centre contact. The units of the colour scale are nanoseconds. . . . . 120
5.31 T60 polar plots corresponding to photopeak events in slice A (top left), slice B (top right), slice C (bottom left) and slice D (bottom right). The T60 rise time values have been measured from the centre contact. The units of the colour scale are nanoseconds. . . . . 121
5.32 T90 polar plots corresponding to photopeak events in slice A (top left), slice B (top right), slice C (bottom left) and slice D (bottom right). The T90 rise time values have been measured from the centre contact. The units of the colour scale are nanoseconds. . . . . 122
5.33 Variation of the T90 rise time as a function of the azimuthal angle $\phi$. The angle was measured, in degrees, starting from the boundary between sector-3 and sector-4. These results correspond to the T90 values measured from the centre contact signal, in correspondence with a fold-1 full energy event in slice B. . . . . 123
5.34 Polar plot showing the time-to-maximum of the current pulses measured from the centre contact. The units of the colour scale are nanoseconds. . . . . 123
5.35 Polar plot showing the asymmetry distributions as a function of the position of the collimator, measured for slice A (left) and C (right). . . . . 125
5.36 Asymmetry values as a function of the azimuthal angle $\phi$ of the interaction, measured on contact A2 at two different radii, namely 1.4 cm and 2.5 cm (left), and C2 at three different radii, namely 1.4 cm, 2.5 cm and 3.1 cm (right). The angle $\phi$ is 0° at the boundary between sector one and sector two, 60° at the boundary between sector two and three. . . . . 125
5.37 A qualitative indication of the achievable position resolution. The pixels show, at each given position, the uncertainty in the 2D-position determination. By performing pulse shape analysis, ∼290 unique positions can be distinguished. The cube on the right part gives an indication of the average position resolution. The figures are not in scale. . . . . 129
5.38 The nine collimator positions within sector two considered in the analysis. . . . . 130

5.39 2-dimensional position response of sector 2: the time-to-maximum of the current pulse is plotted against the asymmetry for the nine positions of Fig. 5.38. The spatial coordinates of each position are indicated on the top and on the right hand side of the graph. The highlighted areas indicate the general trend of the data. . . 130

5.40 2-dimensional position response of sector 2: the T30-time is plotted against the T90-time for the same nine positions of the scanning table. The spatial coordinates of each position are indicated on the top and on the right hand side of the graph. The spatial coordinates of each position are indicated on the top and on the right hand side of the graph. The highlighted areas indicate the general trend of the data. . . 131

A.1 Geometry of the detector calculated in the simulation. . . . . 137

A.2 Fraction of full energy events as a function of the $\gamma$-ray energy. Uncertainties in the measurements are statistical and typically $\leq$10%. . . . . 138

A.3 Relative strength of possible interaction mechanisms leading to a full energy event in the TIGRE detector. . . . . 139

A.4 Fold distribution at various $\gamma$-ray energies. . . . . 140

A.5 The fraction of full energy events where the first interaction is also the main interaction is plotted versus the energy of the incident $\gamma$ ray. . . . . 141

A.6 Scattering path of a $\gamma$ ray inside the detector material, where the first interaction is not the main interaction. . . . . 141

A.7 Average distance between the first and main interaction for full energy events in which the first interaction is not the main interaction. . . . . 142

A.8 The average angular separation between the first and main interaction, for full energy events in which the first interaction is not the main interactions. The angular separation was calculated by considering a source-detector distance of 16 cm. . . . 143

A.9 Fraction of fold-2 events where the first hit segment is also the segment in which most of the initial $\gamma$-ray energy has been released. Both all events and only photopeak events have been considered. . . . . 144

A.10 Simulated (left) and experimental (right) add-back spectra for different fold activated. . . . . 146

# List of Tables


2.1 Physical properties of germanium [GER]. . . . . 14

3.1 Predicted performances for a $\gamma$-ray tracking array, as reported in [Aga01]. . . . . 46

4.1 Gain and offset values of the outer contact preamplifiers. . . . . 58

4.2 Energy resolution results at 122 and 1332 keV for the outer contact signals. . . . . 61

4.3 The table summarises the sensitivity results obtained for each slice of the detector, using different gates on the energy of centre and outer contact signal. A *wide* gate indicates an energy window of 50 keV around the 662 keV $\gamma$-line, a *narrow* gate defines an energy window of 15 keV (see Fig. 4.13). . . . . 69

5.1 The rise time values as a function of the radial position have been fitted with a straight line. The parameters extracted from the centre contact and from a typical outer contact (B3) are reported here. The $\chi^2$ gives an indication on the quality of the fit. . . . . 116

5.2 Radial position of the interaction obtained from the specified fit. The results are consistent with a radial position of 27 mm. . . . . 118

5.3 Asymmetry versus angular position of the interaction. The parameters extracted from the outer contacts C2 and A2 are here reported. The notation FADCu stands for the FADC arbitrary units. . . . . 126

5.4 2D-position resolution values, calculated at the radial distances of 14 mm, 25 mm and 31 mm. The radial position resolution ($\Delta r$) correspond to the uncertainty on the radial position determination, while the angular position resolution ($\Delta\phi$) corresponds to the uncertainty on the angular position determination. The results for the angular position resolution are presented both in degrees and in millimeters. 128

A.1 Fraction of events having the first interaction in a given slice. . . . . 143
A.2 Hit pattern distribution at 662 keV. . . . . 145
A.3 Fold distribution at 662 keV. . . . . 145
A.4 Peak-to-total ratio for different fold activated. Fold one event corresponds to the energy spectrum in all the germanium crystal if only one contact is involved in the $\gamma$-ray event, while fold two (three, etc.) corresponds to the energy spectrum recovered by adding-back the two (three, etc.) partial energies deposited in the segments involved in the $\gamma$-ray event. . . . . 146

# Chapter 1

# Introduction

A principal aim of nuclear structure research is to achieve a quantitative understanding of the nature of strongly interacting matter and to develop a comprehensive theoretical model of the nucleus, a many body quantal system. Significant advances in the knowledge of nucleon-nucleon interactions and the behaviour of individual nucleons in the many body nuclear system have come from studying nuclear excitation through the detection of by-products of nuclear reactions.

At present, the behaviour of nuclei near the valley of stability and, to a lesser extent, that of proton-rich nuclei, has been studied, as described in Fig. 1.1. Although numerous experimental approaches are available nowadays, many fundamental questions still remain unanswered, especially the behaviour of nuclei under the extreme condition of isospin [Kra88]. In the next decade, the major challenge for nuclear spectroscopy will be to explore the "terra incognita" that lies far from the valley of stability, in an attempt to describe nuclear forces and effective interactions in the regime of weak binding. This will provide a powerful tool to address questions concerning the mechanism of binding in radioactive nuclei including:

- the breakdown and modification of shell structure [Dob96],
- the existence of n-p pairing interactions and density-dependent pairing forces [Kel01, Sat01],
- the phenomenon of nuclear magnetism [Frau01],

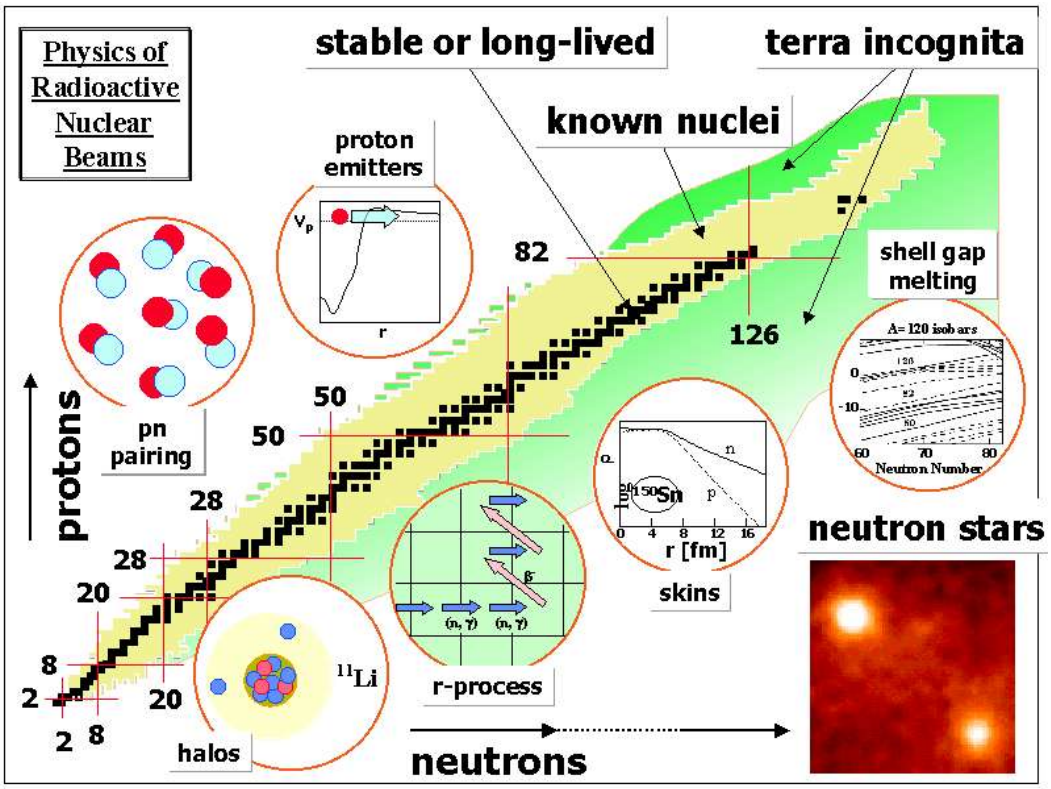


Figure 1.1: Map of the bound nuclear system as a function of the proton number Z and the neutron number N [Dob02]. The black points forming the "valley of stability" are the stable nuclei. By adding either protons or neutrons, one moves away from the valley of stability towards the drip lines, where the nuclei become unbound. The yellow points represent unstable nuclei that are known experimentally. The green points indicate radioactive nuclei with very large or very small N/Z ratios that have not yet been accessed. While the proton drip line has been investigated experimentally up to Z=83, the neutron drip line has been predicted, on the basis of nuclear models, only for the lightest nuclei. Of particular interest are neutron-rich nuclei towards the neutron drip line, proton-rich nuclei at and beyond the proton drip line and the extension of the N=Z line, since they provide a tool to investigate the origin and evolution of nuclear matter in the universe. These nuclei known as "exotic nuclei" can only be produced in reactions induced by radioactive ion beams.

- proton radioactivity [Davi98],
- the possible clustering in neutron skins and halo nuclei [Sme99],
- the description of soft collective modes of excitation and chaotic phenomena [Vol02],
- the prediction of a new island of stability for super-heavy elements [Kor02].

Furthermore, the study of exotic nuclei will add to the understanding of important astrophysical synthesis such as the r- and rp- processes [Bro02]. For a general review on these topics, the reader is referred to [Ber02, Mark01] and references therein.

In order to address such a challenging scientific programme, a new generation of experiments is required, focused on the use of radioactive ion beams (RIBs). The use of radioactive beams will allow access to new isotopes and increase the production rates of nuclei that can presently be populated only with very low cross sections. Radioactive ion beams are already available at laboratories such as ORNL (HRIBF) [ORN], MSU (NSCL) [MSU], TRIUMF (ISAC) [Poi99], GANIL (SPIRAL) [Lie97] and CERN (REX-ISOLDE) [Kes01]. Future RIB facilities such as RIA (the Rare Isotope Accelerator) [RIA], CASIM (SIRIUS) [CAS], TRIUMF (ISAC II) [Pasi01] and the GSI upgrade [GSI] are emerging now.

These facilities will enable new experiments to be designed embracing a wide energy range and variety of nuclear reactions. Although essentially different, all these experiments share the problems associated with the use of radioactive ion beams: low production rates, high background radioactivity and large Doppler effects. Therefore, improvements in the sensitivity of the detection system become essential to the success of such a fascinating scientific program.

This work describes the initial R&D efforts towards the development of highly sensitive detector technology and the associated electronics, suitable for forming an integral part of the aforementioned project. The research objective is to characterise the response function of a closed-ended coaxial germanium semiconductor detector in order to provide the information necessary for input into a $\gamma$-ray tracking algorithm. A dedicated scanning apparatus, which allows a calibration of the detector response as a function of the interaction position of a $\gamma$-ray photon, has been built and the frontal surface of detector has been scanned. The principal aims of the detector scan were:

- to investigate the response function of the detector to collimated radiation: this will provide information on the interaction and charge collection processes in germanium detectors;
- to define the characteristic features of the pulse shapes at each known interaction position and to develop a method to extract them;
- to prove the feasibility of performing pulse shape analysis as a tool to improve the position resolution of the detector.

# Chapter 2

# Principles of radiation detection

## 2.1 Introduction

The operating principle of a semiconductor detector is based on the generation of an electrical signal, which is proportional to the energy of the incident radiation. In order to probe the structure of the nucleus, by-products following a nuclear reaction have to be studied. In this work the field of $\gamma$-ray spectroscopy will be discussed. A thorough knowledge of the interaction mechanisms of photons with matter and of the basic principles of radiation detection is essential to a good understanding of the response function of the detector. In this chapter the following topics will be discussed: the interaction mechanisms of photons with matter and the generation of the secondary charge carriers; the signal generation process and the influence of the crystal orientation on the transport properties; the choice of germanium as detector material and the features of germanium detectors.

## 2.2 The interaction of photons with matter

Photons interact with matter by transferring all or part of their energy to the atomic electrons of the material. Typically, the absorption of a $\gamma$ ray requires one or more interactions in the detector material. In the energy range from $\sim$10 keV to a few MeV the main interaction processes of photons with matter are the photoelectric effect, Compton scattering and pair production.

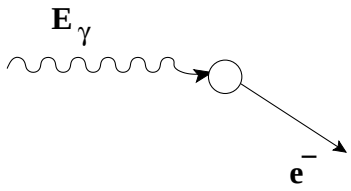


Figure 2.1: A schematic sketch of the photoelectric effect.

### 2.2.1 Photoelectric effect

The photoelectric effect is the the dominant interaction mechanism for low energy photons (up to 200 keV for Ge). In the photoelectric absorption process, the photon completely transfers its energy to a bound atomic electron, which is then ejected by the atom (Fig. 2.1). The kinetic energy of the outgoing photo-electron is given by:

$$E_{e^-} = E_\gamma - E_b, \tag{2.1}$$

where $E_b$ is the binding energy of the electron and $E_\gamma = h\nu$. The vacancy left in the atomic shell is filled through electron rearrangement and the excitation energy is then carried away in the form of a characteristic X-ray or Auger electrons. Theoretical calculations for the cross section for the photoelectric absorption provide the following expression [Dav68]:

$$\sigma_{ph} \approx constant \times \frac{Z^n}{E^{\sim 3}}, \tag{2.2}$$

where $n$ is a number between 4 and 5. The cross section for photoelectric absorption is hence larger for higher Z materials and it decreases as the $\gamma$-ray energy increases.

### 2.2.2 Compton scattering

Compton scattering is the predominant interaction mechanism between ~200 keV and 5-6 MeV. As sketched in Fig. 2.2, the incoming $\gamma$ ray transfers a fraction of its initial energy to a weakly bound electron, which is ejected by the atom (recoil electron), and the scattered $\gamma$ ray is deflected through an angle $\theta$ that ranges between $0^\circ$ and $180^\circ$. Assuming that at the instant of scattering the electron is unbound and at rest, the energy of the scattered

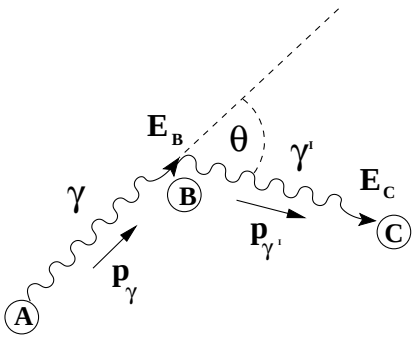


Figure 2.2: Quantities involved in a Compton scattering interaction. The $\gamma$ ray transfers part of its energy to an atomic electron which, in turn, releases that energy in the Ge crystal.

photon, $E_{\gamma^I}$, is derivable from the energy and momentum conservation law,

$$E_{\gamma^I} = \frac{E_\gamma}{1 + \frac{E_\gamma}{m_0 c^2}(1 - \cos\theta)}, \tag{2.3}$$

where $m_0 c^2$ is the rest-mass energy of the electron (511 keV). The energy ranges from $E_\gamma$ to a minimum value of approximately $m_0 c^2/2$. If, the position of the $\gamma$-ray emission is known, the scattering angle $\theta$ can be obtained from the coordinates of the three points involved (as illustrated in Fig. 2.2):

$$\cos\theta = \frac{\vec{p_\gamma} \cdot \vec{p_{\gamma^I}}}{|\vec{p_\gamma}| \cdot |\vec{p_{\gamma^I}}|}. \tag{2.4}$$

Equations 2.3 and 2.4 are the foundations of the tracking concept, since they provide an alternative determination of both energy and angle involved in the scattering process. By inserting the value of the angle $\theta$ in the expression for $E_{\gamma^I}$, an independent measurement of the energy of the scattered $\gamma$ ray can be obtained.

The angular distribution of scattered $\gamma$ rays can be can be calculated using quantum electrodynamics and is known as the *Klein-Nishina* formula [Kno00c]:

$$\frac{d\sigma}{d\Omega} = Z r_e^2 \left(\frac{1}{1 + \alpha(1 - \cos\theta)}\right)^2 \left(\frac{1 + \cos^2\theta}{2}\right) \left(1 + \frac{\alpha^2(1 - \cos\theta)^2}{(1 + \cos^2\theta)[1 + \alpha(1 - \cos\theta)]}\right) \tag{2.5}$$

where $\alpha = E_\gamma / m_0 c^2$ and $r_e$ is the classical electron radius (2.817 fm). The total Compton scattering cross section $\sigma_{Comp}$ is obtained by integrating the Klein-Nishina formula over all the solid angle. The maximum kinetic energy of the recoil electron is given by [Leo93a]:

$$T_{max} = E_\gamma \left(\frac{2\alpha}{1 + 2\alpha}\right) \tag{2.6}$$

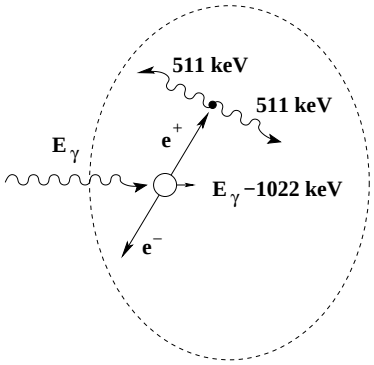


Figure 2.3: Schematic sketch of pair production interaction.

and is called the Compton edge.

Other possible scattering processes are:

- Rayleigh scattering, which is an elastic scattering of $\gamma$ rays, characterised by the fact that *no* energy is transferred to the medium. Rayleigh scattering occurs at low energy.
- Thomson scattering, which is the scattering of photons by free electrons. Thomson scattering occurs at very low energy, it can therefore be neglected in the energy range of interest for nuclear spectroscopy.

### 2.2.3 Pair production

For $\gamma$-ray energies above a few MeV (threshold energy equal to $2m_0c^2$), pair production can occur. This process is characterised by the disappearance of the photon in the Coulomb field of the nucleus and by the creation of an electron-positron pair. The energy balance of the process is

$$E_\gamma = 2m_0c^2 + T_{e^+} + T_{e^-}, \tag{2.7}$$

where $T_{e^-,e^+}$ is the kinetic energy given to the electron/positron, while the recoil energy given to the atom can be neglected. By-products of the pair production process are two annihilation photons, from the annihilation of the positron with a free electron in the medium (Fig. 2.3). The pair production cross section, $\sigma_{pair}$, increases rapidly with energy and becomes dominant only for energies above 5 MeV.

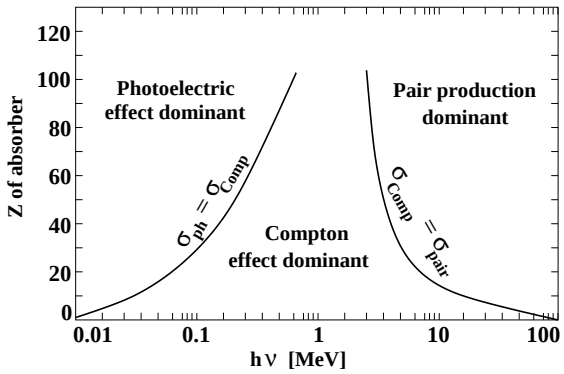


Figure 2.4: The relative importance of the three major interaction mechanisms. The lines show the values of Z and $h\nu$ for which the two neighbouring effects are equal.

### 2.2.4 Attenuation coefficients

The total cross section for the interaction of a $\gamma$-ray photon is the sum of the cross sections of the possible interaction mechanisms:

$$\sigma_{tot} = \sigma_{ph} + \sigma_{Comp} + \sigma_{pair}. \tag{2.8}$$

The relative importance of the photoelectric, Compton scattering and pair production interaction processes is depicted in Fig. 2.4. The *total absorption coefficient* represents the probability for an interaction per unit length and is obtained by multiplying $\sigma$ by the density of atoms N:

$$\mu = N\sigma = \left(\frac{N_a \rho}{A}\right)\sigma, \tag{2.9}$$

where $N_a$ is Avogadro's number, $\rho$ the material density and A the molecular weight.
The fraction of photons transmitted through a thickness $t$ of material is then given by

$$I = I_0 e^{-\mu t}, \tag{2.10}$$

where $I_0$ is the incident intensity. The *mean free path* $\lambda$ is defined as the average distance between two interaction points. It is calculated as:

$$\lambda = \frac{\int_0^\infty x e^{-\mu x}}{\int_0^\infty e^{-\mu x}} = \frac{1}{\mu}, \tag{2.11}$$

and it is simply the reciprocal of the total absorption coefficient. Typically $\lambda$ ranges from a few millimeters to tens of centimeters.

## 2.3 Production of charge carriers

In the previous section, it has been highlighted that the absorption of $\gamma$ radiation results in the creation of one or more energetic electrons. The electrons then lose their energy in the material through the creation of secondary charged particles. Since the range of primary electrons in germanium, up to energies above several hundred keV, is less than a millimeter, the production of the secondary charge carriers is considered a localised process [Muk76]. The energy loss is governed by two mechanisms: 1) the ionisation and excitation process due to collisions with the atomic electrons and 2) the emission of electromagnetic radiation (*Bremsstrahlung*) due to scattering in the electric field of the nucleus:

$$\left(\frac{dE}{dx}\right)_{tot} = \left(\frac{dE}{dx}\right)_{coll} + \left(\frac{dE}{dx}\right)_{rad}. \tag{2.12}$$

The collisional energy loss is given by the Bethe-Bloch formula [Leo93b]:

$$-\left(\frac{dE}{dx}\right)_{coll} = 2\pi N_a r_e^2 m_e c^2 \rho \frac{Z}{A}\frac{1}{\beta^2}\left[\ln\frac{\tau^2(\tau+2)}{2(I/m_e c^2)^2} + P(\tau) - \delta - 2\frac{C}{Z}\right], \tag{2.13}$$

where $r_e$ is the classical electron radius (2.817 fm), $m_e$ is the electron mass, $N_a$ is Avogadro's number ($6.022\times10^{23}$ mol$^{-1}$), $I$ is the mean excitation potential, $Z$, $A$, and $\rho$ are, respectively, the atomic number, weight and density of the absorbing material, $\beta$ is the v/c of the incident electron, $\tau$ is the kinetic energy of the electron in units of $m_e c^2$, $\delta$ is the density correction, $C$ is the shell correction and, finally, $P(\tau) = 1 - \beta^2 + \frac{\frac{\tau^2}{8} - (2\tau+1)\ln 2}{(\tau+1)^2}$ .
The collisional loss is the dominant contribution below a few MeV. At higher energy, due to the low mass of the electrons, radiative processes are possible and indeed, for energies above tens of MeV they become dominant. The energy loss through *Bremsstrahlung* is given by the formula [Leo93b]:

$$-\left(\frac{dE}{dx}\right)_{rad} = N E_0 4 Z^2 r_e^2 \alpha \left(\ln\frac{2E_0}{m_e c^2} - \frac{1}{3} - p(Z)\right), \tag{2.14}$$

where $\alpha = 1/137$ and $p(Z)$ is a correction factor that takes into account the Coulomb interaction of the emitted electron in the electric field of the nucleus.

Since not all the energy of the energetic electron goes into the charge production process, but part of it is dissipated in lattice vibrations, a parameter of importance for a semiconductor detector is the ionisation energy, $\epsilon_{pair}$, i.e. the average energy required to create an electron-hole pair: the smaller this parameter, the larger the number of the

produced charge carriers. This will result in smaller statistical fluctuations. For germanium at 77K, $\epsilon_{pair} \simeq 3$ eV. The number of electron-hole pairs created when an energetic electron deposits an energy $E_e$ is equal to:

$$N_{pair} = \frac{E_e}{\epsilon_{pair}}. \tag{2.15}$$

To calculate the statistical fluctuations, Poisson statistics, which only apply to random independent events, cannot strictly be applied. The production of electron-hole pairs affects the probability of another pair being created, i.e. the events cannot be considered independent. It is observed that the fluctuations in the number of ionisations produced are less than those calculated from Poisson statistics. Fano [Fan47] calculated a statistical variance, which agreed with experimental data, by introducing the factor $F$, known as Fano factor:

$$\Delta N_{pair} = \sqrt{F N_{pair}} = \sqrt{F \frac{E_\gamma}{\epsilon_{pair}}}, \tag{2.16}$$

The Fano factor takes into account all the ionisations processes which yield an energy transfer in the detector and is an intrinsic constant of the material. Only for F=1, the charge carrier mechanism follows Poisson statistics. For germanium at 77 K, F$\simeq$0.06.

## 2.4 The choice of a $\gamma$-ray detector material

In many radiation detection applications, solid state materials are used. The use of solid state, rather than gas-filled, detectors allows the size of the detector to be smaller, because of the higher solid state density. High efficiency scintillation detectors can be built from solid state material, but the large energy required to produce the charge carriers responsible for the signal generation ($\sim$100 eV) and the consequent small number of carriers created by the $\gamma$-ray interaction results in a very poor energy resolution ($\sim$10 %). Semiconductor materials, in which the number of generated charge carriers is much larger, provide the best energy resolution performance.

The electrical properties of semiconductor materials arise from their particular band structure, as shown in Fig. 2.5. Metals have the highest occupied energy band only partially full; insulators have a very large energy gap between the top of the valence and the bottom of the conduction band; semiconductors have only a small energy gap ($\sim$1 eV).

Among the semiconductors, germanium is the material of choice for $\gamma$-ray detection. Germanium has larger atomic number (Z=32) than silicon (Z=14) and therefore a larger

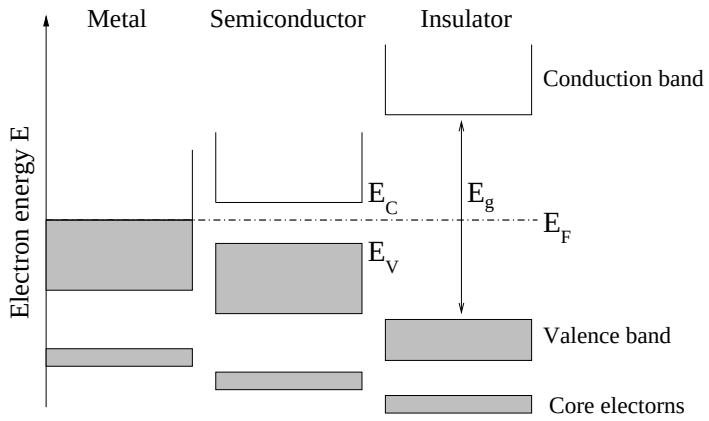


Figure 2.5: Energy level diagrams for a metal, a semiconductor and an insulator. Even at T=0 K, metals have partially occupied bands (shaded). For semiconductors and insulators the Fermi level lies between the occupied valence band and the unoccupied conduction band.

attenuation coefficient. Furthermore, the smaller energy gap (at T=0 K, $E_g$=0.75 eV, which compares to $E_g$=1.17 eV for silicon) results in a better energy resolution (∼0.3 %).

## 2.5 Properties of germanium

Germanium is a group IV semiconductor. Its physical properties are reported in Tab. 2.1. It has a crystalline structure based on a face-centered cubic (FCC) diamond lattice structure, as shown in Fig. 2.6. Due to the small band gap, even at room temperature, electrons are thermally excited into the conduction band where they are free to move. The electrons that enter in the conduction band and the holes that they leave in the valence band form an *electron-hole pair*. In the presence of an electric field, the electrons in the conduction band and the holes in the valence band are responsible for the current flow. The current density can be written as [Iba95a]:

$$J = \mid e \mid (n\mu_n + p\mu_p)E, \tag{2.17}$$

where $n$ and $p$ are the concentrations of electrons in the conduction band and holes in the valence band, respectively, and $\mu_n$ and $\mu_p$ are their mobilities. According to Fermi-Dirac statistics, $n$ and $p$ can be calculated [Iba95a] by integrating the probability distribution

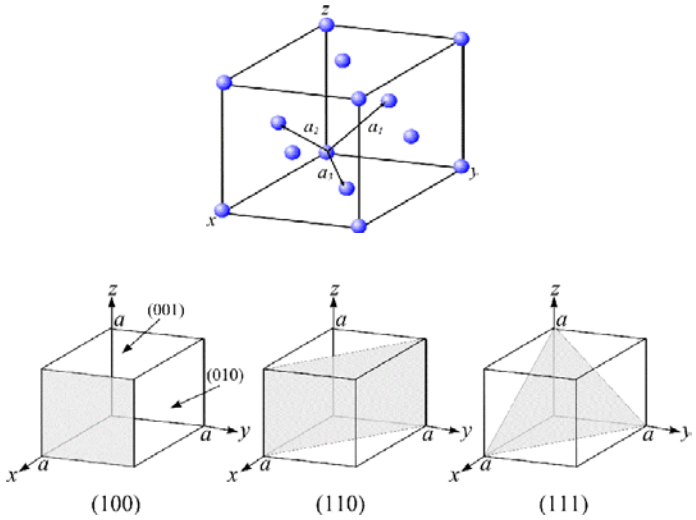


Figure 2.6: Crystal structure of germanium showing the tetrahedral bonding and the lattice vector, $a_{1,2,3}$, (top) and the lattice planes (bottom), labelled by Miller indices.

function $f(E,T)$, weighted by the density of the states in the conduction band, $N(E_C)$, and in the valence band, $N(E_V)$, over all the possible energy levels, i.e. above the bottom of the conduction band ($E_C$) for electrons,

$$n = \int_{E_C}^{\infty} N_C(E) f(E,T) dE \approx N_{eff}^{C} \exp\left(-\frac{E_C - E_F}{kT}\right), \tag{2.18}$$

and below the top of the valence band ($E_V$) for holes,

$$p = \int_{-\infty}^{E_V} N_V(E)[1 - f(E,T)] dE \approx N_{eff}^{V} \exp\left(\frac{E_V - E_F}{kT}\right). \tag{2.19}$$

The prefactors $N_{eff}^{C}$ and $N_{eff}^{V}$ are the partition functions for translational motion in three dimensions and represent the effective density of states in the conduction and valence band,

$$N_{eff}^{C,V} \equiv 2\left(\frac{2\pi m_{n,p}^{*} kT}{h^2}\right)^{3/2}, \tag{2.20}$$

where $m_n^*$ and $m_p^*$ are the effective mass of electrons and holes. The second term of equations 2.18 and 2.19 has been obtained in the limit $E - E_F \gg 2kT$, where $E_F$ denotes the Fermi level energy and $k$ is Boltzmann's constant. In this case, the Fermi-Dirac function $f(E,T)$ can be approximated by the Maxwell-Boltzmann occupation statistics.

| | |
|---|---|
| Atomic number Z | 32 |
| Atomic weight A | 72.6 |
| Atoms | $10^{22}$ cm$^{-3}$ |
| Density | 5.32 [g/cm$^3$] |
| Crystal structure | FCC (diamond) |
| Lattice parameter | 5.658 $\mathring{A}$ |
| $n_i$ (T=300 k) | $2.4\times10^{13}$ |
| Dielectric constant $\epsilon_r$ | 15.8 |
| Intrinsic resistivity (T=300 K) | 16 $\Omega$cm |
| Energy gap (T=300 K) | 0.67 eV (indirect) |
| Energy gap (T=0 K) | 0.75 eV (indirect) |
| Electron mobility $\mu_n$(T=300 K) | 3900 cm$^2$/Vs |
| Hole mobility $\mu_p$(T=300 K) | 1900 cm$^2$/Vs |

Table 2.1: Physical properties of germanium [GER].

For an intrinsic semiconductor at equilibrium, the concentration of electrons and holes are equal, thus the intrinsic charge carrier concentration $n_i$ can be defined by the so called *law of mass action*:

$$n_i = \sqrt{N_{eff}^C N_{eff}^V} \exp\left(\frac{-E_g}{2kT}\right). \tag{2.21}$$

The charge neutrality ($n = p = n_i$) allows a definition of the Fermi level as:

$$E_F = \frac{E_C + E_V}{2} + \frac{3}{4}kT \ln\left(\frac{m_p^*}{m_n^*}\right). \tag{2.22}$$

If $m_n^* = m_p^*$ the Fermi level lies, for all temperatures, in the middle of the forbidden gap. The concentration of charge carriers can be drastically changed by doping the semiconductor with electrically active impurities. These impurities increase the concentration of the free carriers either by donating electrons to the conduction band (valence-five atoms such as P) or by accepting them from the valence band (valence-three atoms such as B). Valence-five and valence-three atoms are called *donors* and *acceptors*, respectively, while the corresponding doped materials are referred to as *n-type* and *p-type* semiconductors.

The addition of active impurities results in the introduction of energy levels in the forbidden gap, either close to the conduction band and with positive charge character (donors) or close to the valence band and with negative charge character (acceptors). In order to preserve the neutrality condition, the Fermi level $E_F$ moves from the middle of the energy gap towards the bottom of the conduction band (top of the valence band) as the donor (acceptor) concentration is increased.

### 2.5.1 The $p-n$ Junction

The operating principle of a semiconductor detector is based on the physical characteristics of the $p-n$ junction (see Fig. 2.7). The term *junction* refers to the border between two halves of a semiconductor crystal, doped with different types of impurities. Due to the different concentration of electrons and holes and to the different position of the Fermi level in the two regions, a bending of the band structure and a corresponding diffusion of charge carriers in the transition layer occurs. The electrons diffuse from the $n$-side to the $p$-side, leaving behind an excess of positively ionized acceptor atoms, while the holes diffuse from the $p$-side to the $n$-side, leaving behind an excess of negatively ionized donors. As a result, a space charge region, free from charge carriers (*depletion region*) is created, and a consequent electric field arises. The electric field inhibits the diffusion of the charge carriers until equilibrium is reached. The characteristics of the resulting potential difference are determined by solving, in the approximation of an *abrupt* $p-n$ boundary, the Poisson equation. In one dimension the Poisson equation is given by [Sze95b]:

$$\frac{d^2V(x)}{dx^2} = -\frac{\rho(x)}{\epsilon}, \tag{2.23}$$

where $\epsilon=\epsilon_0\epsilon_r$ is the dielectric constant of the material ($\epsilon_r$=16 for Ge) and $\rho(x)$ is the uniform charge distribution, equal to $eN_D$ in the $n$-side and to $eN_A$ in the $p$-side. From the conservation of the total charge, it follows that [Iba95b]:

$$N_A x_p = N_D x_n, \tag{2.24}$$

where $x_n$ and $x_p$ are the extents of the depletion region in the two sides of the junction. In the extreme case of $N_A \gg N_D$, the depletion region extends only on the $n$-side of the junction. The *built-in* potential is hence defined as:

$$V_{bi} = \frac{e}{2\epsilon}\left(N_A x_p^2 + N_D x_n^2\right), \tag{2.25}$$

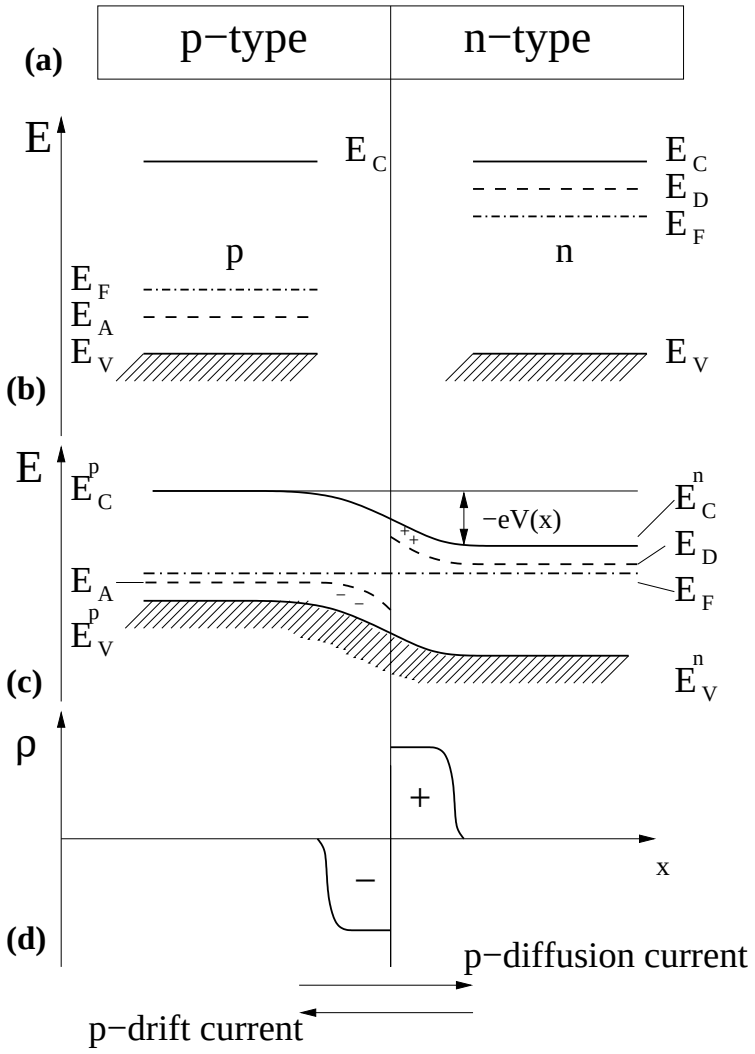


Figure 2.7: Schematic representation of a $p-n$ junction in thermal equilibrium: (a) Semiconductor crystal, $p$-type on one side and $n$-type on the other side. (b) Band scheme in the imaginary case of total decoupling of the two sides. $E_C$ and $E_V$ indicates the bottom of the conduction and the top of the valence band, $E_A$ and $E_D$ represent the ground states of the acceptors and donors; $E_F$ is the Fermi level. (c) Band scheme of the $p-n$ junction when the two sides are in thermal equilibrium with one other. The transition from the $p$ to the $n$ region is assumed to be abrupt. The position of the conduction and valence edges are denoted $E^n_{C,V}$ on the $n$-side and $E^p_{C,V}$ on the $p$-side. In the region of the junction an electrostatic potential is induced. (d) The fixed space charge $\rho(x)$ in the region of the junction due to the ionised impurities. This region is free from charge carriers and therefore is also known as the *depletion region* [Iba95b].

and it is typically very small (< 1V), while the width of the depletion layer is given by:

$$d = x_n + x_p = \sqrt{\frac{2\epsilon V_{bi}}{e}\frac{(N_A + N_D)}{N_A N_D}}. \tag{2.26}$$

In a semiconductor crystal, the electron-hole pairs produced by the passage of ionizing radiation recombine quickly with each other and with the intrinsic charge carriers. In order to use the semiconductor material as a radiation detector, it is necessary to sepatate the charges before they recombine and to increase the size of the depletion region. This is achieved through the application of a reverse bias across the junction. Applied bias voltage also serves to reduce capacitance. The width of the depletion region is given by Eq. 2.26, once $V_{bi}$ has been replaced with $V_{bi} - V_{bias}$. The full-depletion voltage, $V_d$, is the voltage required to extend the depletion layer to the whole junction. In general, radiation detectors are operated at a bias larger than $V_d$ for better charge collection performance.
The capacitance associated with the electrical configuration of the junction is given by [Sze95a]:

$$C = \frac{dQ}{dV} = \frac{\epsilon A}{d}, \tag{2.27}$$

where $A$ is the area of the depletion layer and $d$ its width. Using Eq. 2.26, the space-charge capacitance can be written as

$$C = \frac{A}{2}\sqrt{\frac{N_A N_D}{N_A + N_D}\frac{2\epsilon e}{V_{bi} - V_{bias}}}. \tag{2.28}$$

The capacitance decreases as the reverse bias is increased until a minimum value, $C_d$, corresponding to the full depletion voltage.

### 2.5.2 Detector geometry

A fully depleted junction forms the basis of a radiation detector. Due to the high penetrability of the $\gamma$ radiation, the thickness of the depletion region required to stop $\gamma$ rays fully has to be of the order of a few centimeters. In practice, such a depletion volume cannot be achieved using standard germanium, due to the finite impurity concentration always present in Ge crystals (of the order of $10^{15}$ atoms/cm$^3$). From equation 2.26, the thickness of the depletion region is observed to be inversely proportional to the impurity concentration. In order to fabricate a germanium detector the impurity concentration has to be greatly reduced either by further refining techniques, which allow a impurity concentration of about

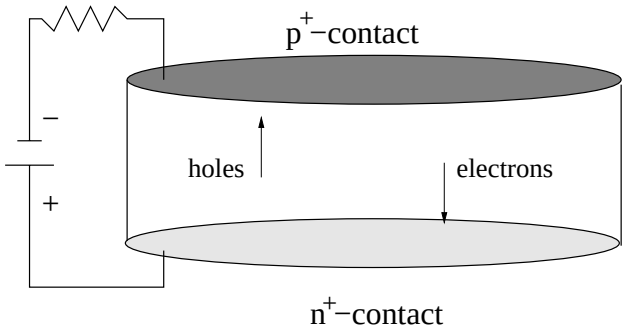


Figure 2.8: Schematic illustration of a planar $n$-type detector; the $n^+$ contact is lithium drifted and $p^+$ one is boron implanted. The secondary charge carriers produced in the depleted region, instead of recombining, drift towards the electrodes, the electrons towards the anode and the holes toward the cathode.

$10^{10}$ atoms/cm$^3$ to be achieved, or by compensating the material by adding interstitial lithium donor atoms (*lithium drifting process*). Detectors built from intrinsic germanium are called *high purity germanium* (HPGe) detectors, detectors produced by the lithium drifting process are termed Ge(Li). The major advantage of a HPGe detector over a Ge(Li) is their larger size and the possibility to warm the detector to room temperature while not in operation and to perform annealing. A Ge(Li) detector has to be kept constantly at the liquid nitrogen temperature because of the high mobility of the lithium impurities in Ge.

The simplest detector geometry is the planar configuration (see Fig. 2.8), where the two electrodes are placed on the surfaces of a germanium disk. Such a detector has a thickness limitation. It is not possible to fabricate a detector with an active depth of more than ∼2 cm. Therefore, the most widespread detector used in nuclear physics experiments is the closed-ended coaxial detector, shown in Fig. 2.9. The closed-ended coaxial detector is build from a cylindrical Ge crystal, in which part of the central core is removed to allow space for a contact over the inner surface. The second contact is placed on the outer surface. The contacts are made by doping the germanium crystal through boron implantation, for the $p^+$ contact, and through lithium drifting, for the $n^+$ one. The contacts are ∼0.5 $\mu$m and ∼500 $\mu$m thick, respectively. Due to the larger thickness of the lithium drifted contact, the $n^+$ electrode is accommodated on the interior hole of the detector, while the $p^+$ one is implanted on the outside. In the bulletised geometry, the frontal corner of the detector and

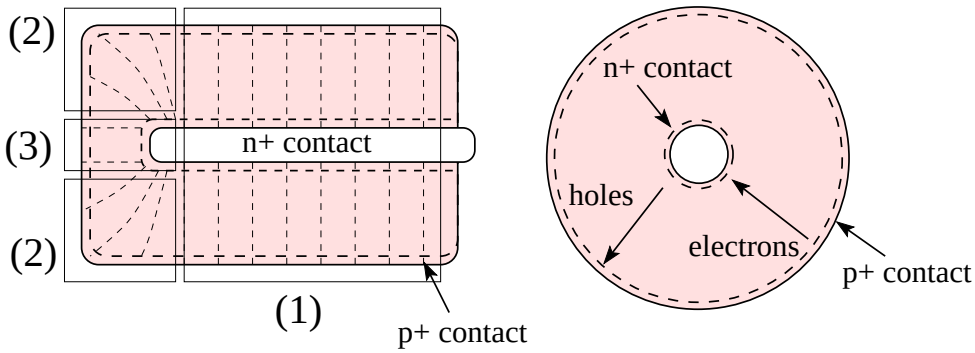


Figure 2.9: Cross section and front view of a $n$-type coaxial closed-ended bulletised germanium detector; the $n^+$ lithium drifted and $p^+$ boron implanted contacts are indicated.

the core hole are bevelled, to favour a more equal distribution of the electric field lines over the detector volume. The detector can be cooled at liquid nitrogen temperature through a cold finger located at the place of the central core.

The main advantages provided by the coaxial geometry are the possibility of fully depleted large crystals and the relatively low capacitance, while the main drawback arises from the electric field distribution inside the closed-ended part of the detector. In fact, a closed-ended detector can be divided into three parts with different behaviour: a true coaxial part at the back (1), a closed-ended part at the front edge (2) and a circular planar part at the front centre (3). As it will be discussed in section 4.3, due to the weak electric field at the closed-end part of the detector, crystal orientation effects will be observed.

Although the fundamental characteristics such as detection efficiency and energy resolution are essentially identical for a $n$-type and a $p$-type detector of the same geometry, historically the use of $n$-type germanium has been preferred due to its improved radiation hardness.

### 2.5.3 Electric field calculation

The value of the electric potential at any point in the detector, $V(x)$, is calculated by solving the Poisson equation (Eq. 2.23). Once the potential is known, the electric field is calculated

as:

$$\mathcal{E}(x) = -\frac{dV(x)}{dx}, \tag{2.29}$$

In the case of a coaxial detector, it is convenient to solve the Poisson equation in cylindrical coordinates:

$$\frac{d^2V(r)}{dr^2} + \frac{1}{r}\frac{dV(r)}{dr} = -\frac{\rho(r)}{\epsilon}. \tag{2.30}$$

The resulting electric field, calculated as $\mathcal{E}(r) = -dV(r)/dr$, is then given by [Kno00a]:

$$\mathcal{E}(r) = \frac{\rho(r)}{2\epsilon}r - \frac{V_{bias} + \frac{\rho(r)}{4\epsilon}\left(r_2^2 - r_1^2\right)}{r\ln\left(\frac{r_2}{r_1}\right)} \tag{2.31}$$

where $r_1$ is the inner radius, $r_2$ is the outer radius and V is the applied voltage. A boundary condition is that the potential difference between the anode and the cathode is equal to the applied voltage, i.e. $V(r_2) - V(r_1) = V_{bias}$. The full depletion voltage $V_d$ can be calculated from equation 2.31 by setting the condition $\mathcal{E}(r_1) = 0$. This results in:

$$V_d = \frac{\rho(r)}{2\epsilon}[r_1^2\ln\left(\frac{r_2}{r_1}\right) - \frac{1}{2}\left(r_2^2 - r_1^2\right)]. \tag{2.32}$$

Notice that the depletion voltage is proportional to the impurity concentration.

## 2.6 The signal generation process

In a depleted junction, the electron-hole pairs created by a $\gamma$-ray interaction do not recombine, instead they drift under the influence of the electric field towards the electrodes. A charge carrier moving near a conducting electrode maintained at constant electric potential induces a current flow in the external circuit [Dab89]. The problem of calculating the instantaneous value of the induced current was solved by Ramo [Ram39], who, for a planar configuration, derived the simple formula known as Ramo's theorem:

$$i(t) = q\frac{\mathcal{E}(x,t)v_d(x,t)}{\psi}, \tag{2.33}$$

where $q$ is the charge of the carrier, $v_d$ is the drift velocity of the charge carrier, $\mathcal{E}$ is the intensity of the electric field at the instantaneous position of the charge and $\psi$ is the electric potential of the electrode.

The application of Ramo's theorem to semiconductor junctions is not trivial, due to the non uniform electric field distribution, which depends on the space-charge distribution. The validity of Ramo's theorem to semiconductor detectors has been investigated by

Deshpande [Des70], Vass [Vas70] and Martini [Mart69]. Green's "reciprocity theorem" is an extension of Ramo's theorem which yields the induced charge on one electrode of a multi electrode device while all other electrodes are grounded. According to Green's theorem, in the assumption of a positive charge moving in the space between two electrodes in a coaxial configuration, the equation 2.33 can be rewritten as [Rad88]:

$$i(t) = -q\vec{\mathcal{E}}_w(\vec{r}(t))\vec{v}_d(\vec{r}(t)), \tag{2.34}$$

where $\vec{\mathcal{E}}_w(\vec{r})$ is the *weighting field* and the time dependence of the drift velocity has been pointed out ($v_d = dr/dt$). The weighting field is an artificial field calculated as the gradient of the *weighting potential*. The weighting potential is obtained by solving the Laplace equation (i.e. Poisson's equation with $\rho = 0$) in the assumption of unity voltage on the considered electrode and zero voltage on all the others. The weighting field, in units of $cm^{-1}$, measures the electrostatic coupling between the moving charge and the sensing contact, and is an extremely important concept for pulse shape calculation [Krö01].

An expression for the weighting field is:

$$\vec{\mathcal{E}}_w = \frac{1}{r \ln\left(\frac{r_2}{r_1}\right)} \tag{2.35}$$

Once the electric field is known, the drift velocity is calculated as

$$\vec{v}_{d_{e,h}}(\vec{r}) = \frac{d\vec{r}(t)}{dt} = \mu_{e,h}\vec{\mathcal{E}}(\vec{r}) \tag{2.36}$$

where $\mu_{e,h}$ is the mobility of electrons and holes, respectively.
The mobility is a parameter that describes the relationship between $v_d$ and $\mathcal{E}$. It can be parametrised as:

$$\mu \simeq \frac{q\tau_c}{m_q}, \tag{2.37}$$

where $m_q$ is the mass of the charge and $\tau_c$ is the time occurring between collision with lattice vibration and atoms of impurities.

The total induced charge, that corresponds to the energy deposited by the radiation, is given by the integral of the current over the whole detector active volume:

$$Q = \int i(t)dt = -q\int_{x_1}^{x_2} \vec{\mathcal{E}}_w d\vec{r} = q[V(x_2) - V(x_1)]. \tag{2.38}$$

From Eq. 2.38 the amount of deposited charge is simply calculated as the difference in the weighting potential between the initial and the final position of the moving charge carrier.

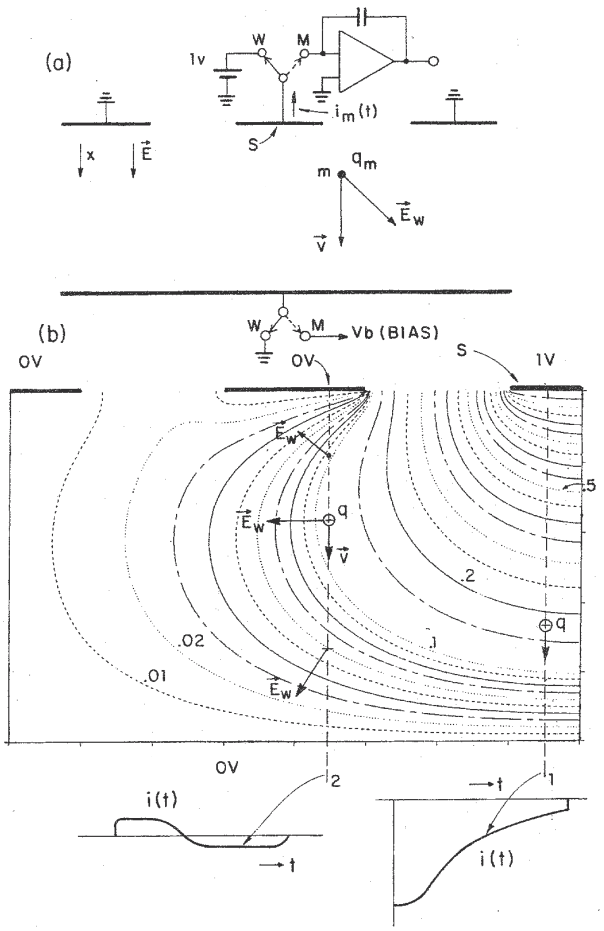


Figure 2.10: (a) Determination of the induced current by the weighting field concept, illustrated on a planar multielectrode strip configuration. The weighting field is defined conceptually as the field for unity potential on the sensing electrode S (switch in position W) and zero potential on all other electrodes. In actual operation, the sensing electrode is connected to a charge amplifier and a uniform operating field is applied to the detector by connecting the opposite electrode to a voltage source (switch in position M). The weighting field calculated numerically for this case is shown as a plot of equipotential lines in (b) for the left half of the electrode structure in (a). Two examples of charge transit from top to bottom are shown. The induced current pulse shapes, resulting from Eq. 2.34 for a localised charge moving at a constant velocity, are shown at the bottom of the figure. Charge $q$ traversing the full distance between the electrodes along line 1 is observed as $Q = -q$, while the current decreases with distance from electrode 1, as the electrostatic coupling decreases. For a charge moving along line 2, the induced charge is zero if the measurement time is longer than the transit time. For a short measurement time a net induced charge is observed (the induced current pulse shape is bipolar, since the weighting-field direction changes along the path).

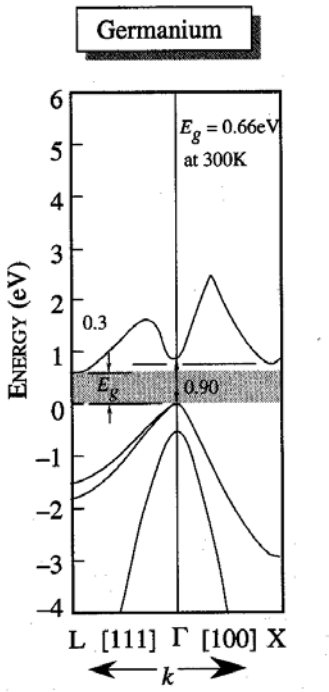


Figure 2.11: Calculated band-structure of Ge in the reciprocal space representation. The band gap, $E_g$, is determined by states with different $\vec{k}$ [Sin01].

Fig. 2.10 shows, qualitatively, the formation of the current pulses in a planar multielectrode system. Two examples of charge travelling the distance between the two electrode are shown: one corresponding to the collection of a net charge and one corresponding to the induction of a transient charge without net charge deposition [Rad88a].

### 2.6.1 The influence of the anisotropic drift velocity on the charge collection process

The conductivity in Ge is anisotropic, i.e. the mobility of electrons and holes varies depending on the direction of the applied electric field with respect to the direction of the lattice vectors [Mih00]. This effect will play an important role in the signal generation process. Theoretical calculations and simulation results on this anisotropy are reported in the literature [Shi55, Nat63, Jac83]; experimental evidence was observed in [Ott75, Can74, Can77]. Germanium is an indirect band gap semiconductor. A plot of the calculated band structure

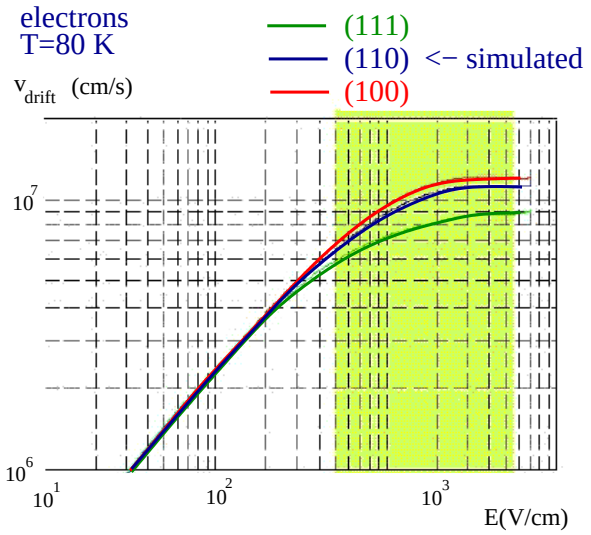


Figure 2.12: Experimental field dependences of the electron drift velocity in germanium along the ⟨111⟩ and ⟨100⟩ directions at a temperature of 80 K and the simulated drift velocity for a field oriented along the ⟨110⟩ direction (taken from [Aga01].)

of Ge, in the reciprocal space representation, is presented in Fig. 2.11. The maximum of the valence band and the minimum of the conduction band are at different positions: the minimum of the conduction band is along the ⟨111⟩ direction, while the maximum of the valence band is along the ⟨000⟩ direction. In the principal axis representation (the principal axes are ⟨111⟩ for Ge) and in the limit of the parabolic approximation (i.e. considering terms only up to the order $k^2$), the energy levels of conduction band electrons, $\mathrm{E}(\vec{k})$, are calculated as [Iba95d]:

$$E(\vec{k}) = \hbar^2 \left( \frac{k_x^2 + k_y^2}{2m_t^*} + \frac{k_z^2}{2m_l^*} \right), \tag{2.39}$$

where $m_{t,l}^*$ are the transverse and longitudinal effective electron masses, whose experimental value relative to the mass of a free electron $m_0$ are $m_t^*/m_0$=0.082 and $m_l^*/m_0$=1.57, respectively. The surfaces of constant energy are therefore ellipsoids around the ⟨111⟩ direction. The structure of the valence band maximum is more complicated, presenting three different bands at $\vec{k} = 0$: two valence bands with different curvature plus a third one resulting form a splitting due to spin-orbit interaction.

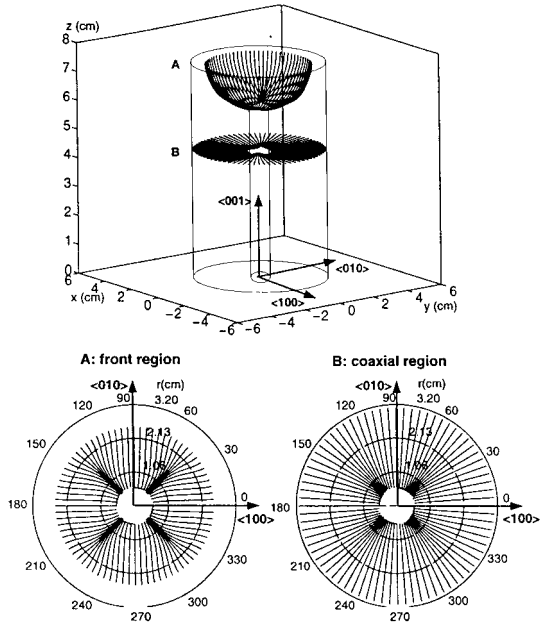


Figure 2.13: Charge carrier trajectories in a closed-ended HPGe detector, from interactions of $\gamma$-ray quanta in the front part (A) and in the coaxial part (B) of the Ge detector. The upper drawing shows a full spatial representation and the lower drawings show front views [Mih00].

It is this characteristic band structure that is responsible for the anisotropy in the conductivity for germanium. Fig. 2.12 shows the drift velocity of the electrons plotted as a function of the electric field for three different orientation with respect to the crystallographic directions. The drift velocity depends clearly on the crystallographic orientation and has its minimum value along the $\langle 111 \rangle$ direction. Furthermore, the drift velocity reaches the saturation value for electric fields higher than $\sim 10^3$ V/cm.

The anisotropy affects two main aspects of the collection process:

1. the collection time,

2. the trajectories of the charge carriers.

The first effect is a consequence of the changes in the magnitude of the drift velocity and influences directly the shape of the signal, while the latter is due to the variation in the angle between the drift velocity and the electric field vectors and is especially important in the

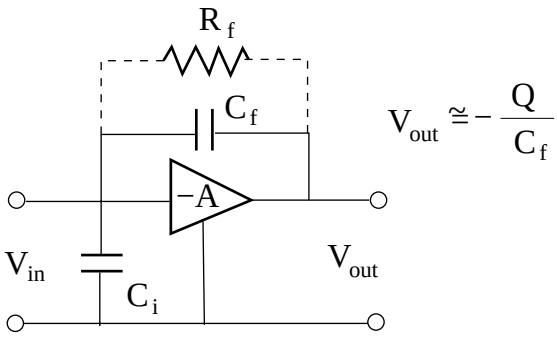


Figure 2.14: Simplified diagram of a resistive feedback charge sensitive preamplifier configuration. The output pulse amplitude is proportional the charge produced by the $\gamma$-ray interaction. The time constant $R_f C_f$ determines the decay rate of tail of the output pulse [Kno00b].

case of segmented detectors, because it determines a preferential direction, i.e. preferential segments, for the charge collection. Charge carrier trajectories for different drift directions with respect to the crystal orientation, as calculated in [Mih00], are shown in Fig. 2.13. The reader is referred to the aforementioned reference.

## 2.7 Detector operational characteristics

### 2.7.1 Preamplifier

The preamplifier represents an interface between the detector and the signal processing electronics [Kno00b]. Its basic function is to amplify and shape the small signal from the detector and to transfer it to the electronic chain with the least degradation. Typically, charge sensitive preamplifiers are used for Ge detectors. In a charge-sensitive preamplifier, the charge carried by the incoming pulse is first integrated on a capacitor and then removed by a slow discharge through a *resistive feedback* network, as shown in Fig. 2.14. This produces a pulse with a fast leading edge (rise time), corresponding to the charge collection time in the detector, and a slow exponential decay (fall time), as sketched in Fig. 2.15.

In order to preserve as well as possible the information carried in the signal leading

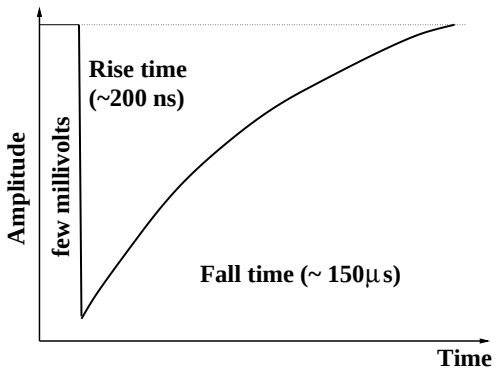


Figure 2.15: Sketch of a preamplifier signal consisting of a fast leading edge and a slow exponential tail.

edge, a very fast, low noise, low power consumption and stable preamplifier is required. To obtain a fast response, i.e. a signal with short rise time (RT), a large bandwidth (BW) preamplifier is required. The relation between the pulse rise time and the preamplifier bandwidth can be derived by considering the preamplifier signal to follow an exponential decay:

$$V_t = V_0 \left(1 - e^{-t\omega_c}\right) \tag{2.40}$$

where $V_t$ is the voltage (i.e. the amplitude of the pulse) at the time $t$, $V_0$ is the final voltage and $\omega_c$ is the decay constant of the exponential function. By default, the rise time is measured as the time from the 10% ($t_{10}$) to the 90% ($t_{90}$) of the final amplitude. By considering equation 2.40 at the time $t_{10}$ and $t_{90}$:

$$0.1V_0 = V_0 \left(1 - e^{-t_{10}\omega_c}\right) \qquad 0.9V_0 = V_0 \left(1 - e^{-t_{90}\omega_c}\right) \tag{2.41}$$

and the relation between decay constant and bandwidth ($\omega_c = 2\pi$ BW) one obtains:

$$RT = t_{90} - t_{10} = \frac{2.2}{2\pi \times BW}, \tag{2.42}$$

where the rise time is measured in seconds and the bandwidth in Hertz ($s^{-1}$).

The complex electronics of segmented detectors, which will be described in the next section, together with the need for a compact cryostat, imposes limitations on the size of the preamplifiers and on the length of the connection wires. One of the most common problems

for segmented detectors is cross-talk. Cross-talk arises following a coupling of the signals from adjacent segments, which results in a net charge observed in segments not involved in the $\gamma$-ray interaction. It is due to an insufficient shielding and crossing of the wires from different electronic channels. A solution for reducing the cable capacitance and therefore cross-talk and pick-up of stray electromagnetic fields is to mount the the preamplifiers very close to the detector.

### 2.7.2 Noise performance

All the random fluctuations, superimposed on the detector signal, are included in the definition of *noise*. Understanding the most relevant sources of noise and their influence on the read-out signal is fundamental for an accurate pulse shape analysis. In this section, a brief review of the noise sources in semiconductor detectors will be outlined. For a complete discussion, the reader is referred to papers by Radeka [Rad88], Dabrowski [Dab89] and Goulding [Gou82].

The quality of a signal is measured by the signal-to-noise (S/N) ratio, which determines the least amplitude of a signal component distinguishable above the noise level. It is of vital importance to have a good signal-to-noise ratio at the beginning of the signal chain: any noise generated at this stage is amplified along with the signal. Contributions to the S/N ratio come from both the detector and the electronics, in particular from the detector capacitance and the field effect transistor (FET) of the preamplifier. For conventional charge-sensitive preamplifiers the electronic noise is evaluated as an equivalent noise charge (ENC), i.e. as the charge corresponding to a signal that would produce the same output amplitude [Pei92a]:

$$ENC = A + B \cdot C \tag{2.43}$$

where A and B are constants, which depend on the preamplifier, while C is the detector capacitance.

The contributions of the leakage current and the bias resistor have also to be taken into account in the noise evaluation. The expression for the equivalent noise charge due to the leakage current is:

$$ENC = \frac{exp}{q}\sqrt{\frac{qIT_p}{4}} \tag{2.44}$$

where $exp$ is the natural logarithm base, $q$ is the electron charge, $I$ is the detector leakage current and $T_p$ is the peaking time, equal to the integration time of the shaper.
The ENC corresponding to the bias resistor is given by:

$$ENC = \frac{e}{q}\sqrt{\frac{T_p kT}{2R}} \tag{2.45}$$

where $k$ is the Boltzmann's constant, T the temperature and R the value of the bias resistor. An improved detector design providing low detector capacitance, high bias resistance and small leakage current, will increase the signal-to-noise ratio.
Depending on the coupling between noise and signal, noise sources are divided into parallel or series noise [Gil98]. For example, the fluctuations in the leakage current and in the gate-source current of the FET are classified as sources of parallel noise, while noise associated with series resistances and the thermal noise of the input FET are sources of series noise. It has to be pointed out that, while the frequency band of the signal is narrow, the frequency distribution of both series and parallel noise components are so broad that it can be considered uniform (or *white*). For this reason, high-pass and low-pass filters can be used for eliminating the low and high-frequency components of the noise, without affecting the signal shape. It is then common practice, to analyse the noise performance of a detector in terms of the power spectrum and of the integrated power as a function of the frequency, by means of a detailed Fourier analysis [Pre99].

### 2.7.3 Energy resolution

The energy resolution of a detector is defined as the full width at half maximum of the spectral peak (FWHM), assuming that the peak has a Gaussian shape and no background or continuum contribution is superimposed on the peak. The intrinsic energy resolution of a germanium detector is determined by the contribution of three factors:

$$(\Delta E_{intr})^2 = (\Delta E_D)^2 + (\Delta E_X)^2 + (\Delta E_E)^2 \,. \tag{2.46}$$

1. $\Delta E_D$ is the inherent statistical fluctuation in the number of charge carriers created. This is given by:

   $$(\Delta E_D)^2 = (2.35)^2 F \epsilon_{pair} E_\gamma \tag{2.47}$$

   where $F$ is the Fano factor, $\epsilon_{pair}$ is the ionisation energy, i.e. the energy required to form an electron-hole pair, and $E_\gamma$ is the $\gamma$-ray energy.

2. $\Delta E_X$ is due to incomplete charge collection. This effect is important in large volume detectors and will be discussed in section 4.3.

3. $\Delta E_E$ is the contribution of all the electronic components following the detector (electronic noise).

Typically, the intrinsic energy resolution is of the order of 2 keV at 1.33 MeV.

The overall energy resolution of a germanium detector is determined by the contribution of two factors:

1. the aforementioned intrinsic energy resolution of the germanium system, $\Delta E_{intr}$,

2. the contributions due to the Doppler effect, $\Delta E_{Dopp}$,

added in quadrature.

$$(\Delta E_{total})^2 = (\Delta E_{intr})^2 + (\Delta E_{Dopp})^2 \,. \tag{2.48}$$

**Doppler broadening**

The energy spectrum measured from radiation emitted by fast moving nuclei shows a shift and a broadening of the spectral lines. A calculation of the energy shift through a transformation of the frame of reference, from the centre of mass (CM) to the laboratory one, yields [Nol79]:

$$E_\gamma = E_\gamma^0 \frac{\sqrt{1-\beta^2}}{1-\beta\cos\theta}, \tag{2.49}$$

where $E_\gamma$ is the energy in the laboratory reference system, $E_\gamma^0$ is the energy in the CM system, $\theta$ is the angle between the scattered projectile and the emitted $\gamma$ ray and $\beta$=v/c is the velocity of the moving nucleus in the laboratory frame (Fig. 2.16). If the emission angle of the $\gamma$ ray is known, the real transition energy is recovered.

The observed Doppler broadening results form the contribution of three factors, added in quadrature:

$$(\Delta E_{Dopp})^2 = (\Delta E_{open})^2 + (\Delta E_{ang})^2 + (\Delta E_{vel})^2 \,. \tag{2.50}$$

1. $\Delta E_{open}$ depends on the geometry of the detector, arising from its opening angle $\Delta\theta$, according to:
$$\frac{\Delta E_\gamma}{E_\gamma} = \frac{\beta sin\theta}{1-\beta\cos\theta}\Delta\theta. \tag{2.51}$$
It can, therefore, be reduced by reducing $\Delta\theta$.

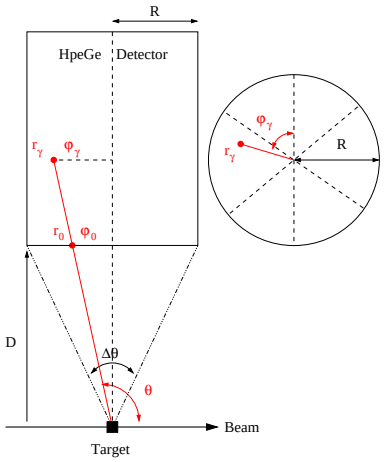


Figure 2.16: Reference system describing the direction of the $\gamma$-ray emission with respect to the front face of the detector. The position of the $\gamma$ interaction $(r_\gamma, \varphi_\gamma)$ is defined in cylindrical coordinates.

2. $\Delta E_{ang}$ is angular spread of the recoiling nuclei, following interaction of an ion beam in a solid target. The spread due to the size of the beam spot has also to be taken into account.

3. $\Delta E_{vel}$ is the variation in the recoil velocity, $\Delta E_\gamma^{vel}$ . Due to the slowing down of the recoils in the target, the velocity of the recoil at the time of emission of the $\gamma$ ray is not known precisely. Although in typical experiments, the relative variation of the recoil velocity is of the order of 10%, it is possible to correct for this factor by measuring the velocity of each recoiling nucleus.

By substituting in equation 2.48 the expression for the Doppler broadening, one obtains [Gla98] :

$$\left(\frac{\Delta E_\gamma}{E_\gamma}\right)^2 = \frac{(\Delta E_{intr})^2}{(E_\gamma)^2} + \left(\frac{\beta sin\theta}{1-\beta\cos\theta}\right)^2 (\Delta\theta)^2 + \left(\frac{-\beta+\cos\theta}{(1-\beta^2)(1-\beta\cos\theta)}\right)^2 (\Delta\beta)^2 . \quad (2.52)$$

The Doppler broadening, and hence the overall detector energy resolution, is worse for large detectors placed at 90° with respect to the beam direction. It can be improved by reducing the detector opening angle $\Delta\theta$, i.e. by segmenting the detectors into parts, while maintaining the total volume (see section 2.9).

### 2.7.4 Efficiency

The counting efficiency of a germanium detector can be classified using a number of primary methods. In this work the *absolute* and the *relative efficiency* will be considered.

1. The absolute efficiency, $\epsilon_{abs}$, is defined as the number of detected events divided by the total number of photons emitted by the source and it is therefore influenced by the detector/source geometry.

2. The relative efficiency, $\epsilon_{rel}$, is the efficiency of a germanium detector relative to a NaI(Tl) crystal, 76 mm in diameter and 76 mm in length, measured at 25 cm from the source. This is the absolute efficiency divided by $1.244\times10^{-3}$.

When defining a counting efficiency, the nature of the detected event has also to be taken into account. The *photopeak efficiency* accounts only for events in which the $\gamma$ ray deposits the full energy in the detector. The photopeak efficiency, $\epsilon_{ph}$, can be defined as:

$$\epsilon_{ph} = (PT) \times \epsilon_{abs}, \tag{2.53}$$

where (PT) is a quality factor termed *peak-to-total ratio*. A standard measurement of the peak-to-total ratio is obtained from the sum of the $^{60}$Co net peak areas divided by the total number of counts in the spectrum for energies from 100 keV to 1350 keV. The peak-to-total ratio is sometimes defined as *peak-to-background ratio*.

Another measure of the spectrum quality is the *peak-to-Compton ratio*. It is defined as the ratio of the counts in the highest photopeak channel to the count in a typical channel of the Compton continuum associated with that peak. Conventionally, the ratio is quoted for the 1332 keV peak from $^{60}$Co, having considered as Compton continuum the interval from 1040 keV and 1096 keV.

### 2.7.5 Time resolution

The time resolution of a germanium detector is measured relative to a fast scintillator detector utilising fast analogue electronics. A typical time resolution for Ge detector is of the order of 5 ns [Kno00d].

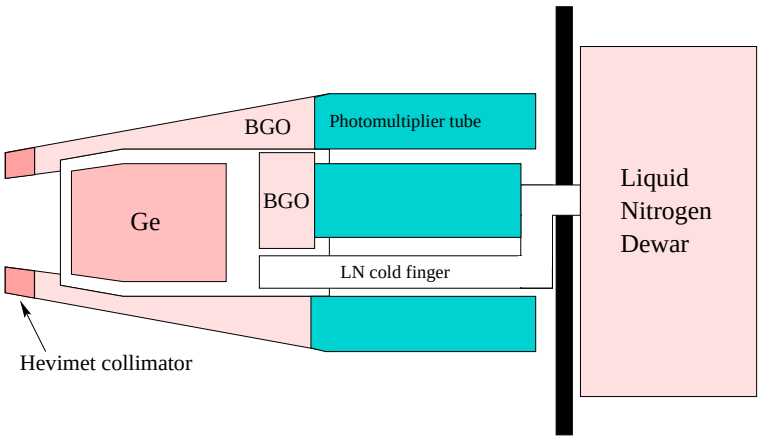


Figure 2.17: A schematic diagram of a Compton suppressed detector, showing a germanium crystal inside its BGO suppression shield. The shield suppresses the Compton scattered $\gamma$ rays that escape from the germanium and also acts as a collimation system, to prevent the scattering of $\gamma$ rays from a Ge detector to its neighbor.

## 2.8 Compton suppressed detectors

Compton suppressed detectors provide a substantial improvement in the peak-to-total ratio. A Compton suppressed detector consists of a germanium crystal surrounded by a Compton suppression shield, such a device is termed an escape suppressed spectrometer (ESS) (see Fig. 2.17). The shield is made of scintillator detectors, usually bismuth germanate (BGO), which are placed around the germanium crystal with the function of detecting the $\gamma$ rays that Compton scatter out of the germanium. Events in coincidence between the scintillator and the germanium are rejected electronically, by means of an analogue electronics timing circuit. The improved quality of a suppressed spectrum is shown in Fig. 2.18; typically the peak-to-total of a suppressed spectrometer is $\sim$60%, which compares with $\sim$20% for an unsuppressed detector [Nol85a].

## 2.9 Multi-element detectors

Multi-element detectors are detectors in which the active volume has been subdivided either physically or electronically into several parts, which each provides an output signal. Such detector can be classified into two classes:

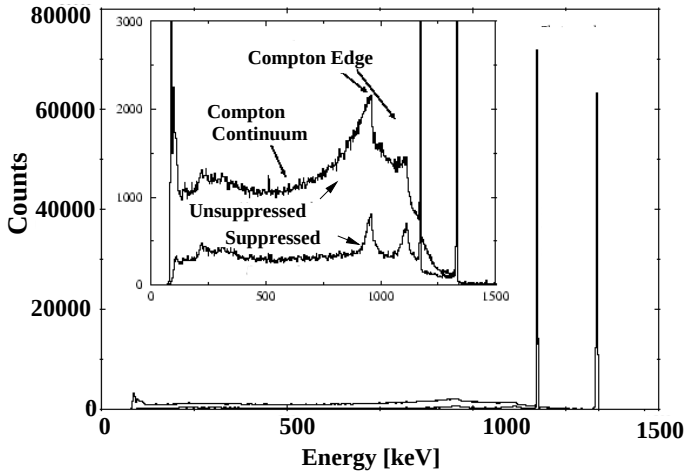


Figure 2.18: Un-suppressed and suppressed $^{60}$Co spectra, measured with a standard HPGe detector. In the insert, the y-axis has been rescaled to show the detail of the background, while the full photopeak intensity relative to the background indicates the overall quality of the spectrum.

1. Composite detector: consists of several germanium crystals, close packed in the same cryostat. Examples are the Clover detector, which is built from four tapered germanium crystals arranged in the configuration of a four-leaf clover [Nol94b, Duc92, Duc99, Shep99] and the Cluster detector, which consists of seven crystals. The Cluster detector utilises crystal encapsulation, a technique developed to improve the reliability of composite detector technology [Ebe92]. In an encapsulated detector each crystal is housed in a sealed aluminium capsule of 0.7 mm wall thickness and fixed at 0.5 mm distance from the surface of the crystal, this results in a decoupling of the crystal vacuum from the cryostat vacuum.

2. Segmented detector: consists of one single germanium crystal, whose readout contact (generally the outer contact) has been electrically segmented. Various segmentation geometries have recently been investigated. Examples are the 2-fold Gammasphere detector [Del88], the 6-fold encapsulated Miniball detector [Ebe97], the 16-fold segmented Exogam Clover detector [Sim00], the 25-fold MARS detector [Baz99], the 32-fold MSU detector [Mue00], the 36-fold GRETA detector [Vet00, Mai99], the 36-

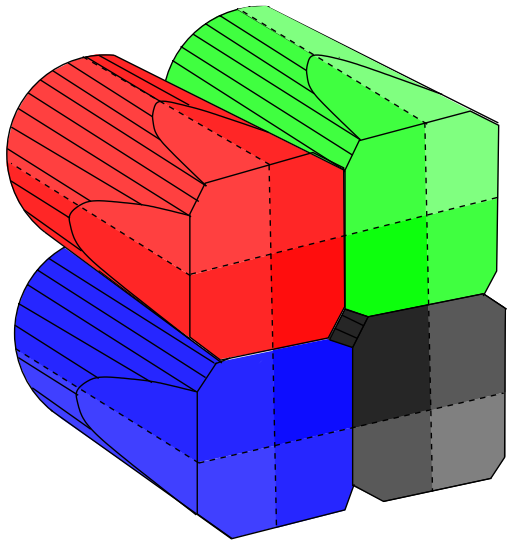

Figure 2.19: Schematic picture of the 16-fold Clover detector. The peculiarity of this detector is that is both composite and segmented.

fold Eurysis detector [Pea01] and the 24-fold Ortec detector, the main subject of this work. In parallel, R&D on segmented planar detectors is being carried out [Lis00].

An example of a composite segmented detector is the 16-fold Exogam Clover detector, whose geometry is depicted in Fig. 2.19. Multi-element detectors provide better energy resolution performance (while maintaining high efficiency) because of their better angular resolution and hence smaller opening angle. Segmented detectors used in conjunction with digital pulse shape analysis techniques enable a position resolution superior to the segment size to be achieved.

Although the segmentation technology is a fairly recent technique in the field of nuclear instrumentation, it is a well established technique in the construction of detectors for high energy physics experiments. For many years, silicon micro-strip detectors have been used as vertex detectors in colliding beam experiments [Pei92].

### 2.9.1 Composite and segmented detector capabilities

In this section the enhanced performance of the composite and segmented detectors will be reviewed. In many aspects composite and segmented detectors exhibit similar characteristics.

### Add-back performance

The efficiency of a composite detector is higher than the efficiency of a single crystal detectors with the same total volume. Indeed, the overall efficiency of a composite detector is a sum of two different primary factors:

- the direct detection efficiency, $\epsilon_D$, is given by the photopeak efficiencies of each crystal considered as a single detector. It is measured by recording separately the full $\gamma$-ray absorption in each of the individual crystals. For the case of a detector made of $n$ crystals the direct efficiency is given by:

$$\epsilon_D = \sum_{i=1}^{n} \epsilon_{D,i} \tag{2.54}$$

- the coincidence detection efficiency, also called the add-back efficiency, $\epsilon_{AB}$. It is measured by summing the energy deposited in the composite detector on an event by event basis. Coincidence events are mainly due to $\gamma$ rays Compton scattering between two or more crystals. The total $\gamma$-ray energy is then recovered by summing the partial energy deposited in the individual crystals.

Hence, the total detection efficiency can be written as:

$$\epsilon = \epsilon_D + \epsilon_{AB} \approx n\epsilon_{D,1} + \epsilon_{AB} \tag{2.55}$$

where the approximation is valid in the case that the $n$ crystals all have the same efficiency. The gain in efficiency obtained by adding coincidence signals together is given by the add-back factor $A$:

$$A = 1 + \frac{\epsilon_{AB}}{\epsilon_D} \tag{2.56}$$

However, it must be considered that coincidence events can also be due to multiple hits, i.e. two different $\gamma$ rays hitting the detector simultaneously. If energies of multiple hit events are added together into the spectrum they would contribute to the background. An additional advantage is provided by a segmented composite detector, like the segmented Exogam Clover. As shown in Fig. 2.20, a segmented Clover detector enables one to distinguish between multiple hit events and a $\gamma$ ray Compton scattering between two adjacent crystals.

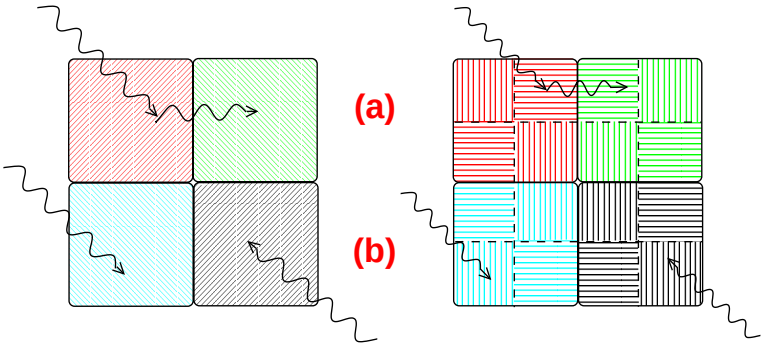


Figure 2.20: Schematic front face of original Clover and segmented Exogam Clover. The segmented detector enables Compton scattered (a) and multiple hits events (b) to be distinguished.

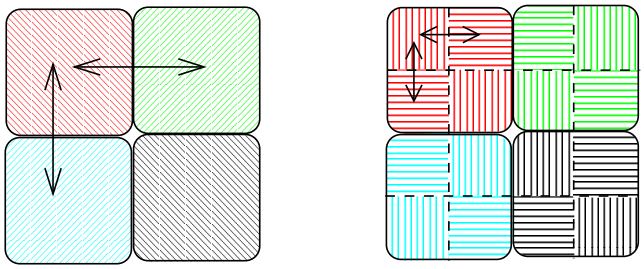

Figure 2.21: Advantages in using segmented detectors as Compton polarimeter.

### Linear polarisation

In heavy-ion fusion evaporation reactions, the residual nuclei are aligned with their spin vector in a plane perpendicular to the beam axis; $\gamma$-ray transitions de-exciting the aligned nuclear state show an anisotropy of angular distribution and linear polarisation, depending on the nuclear alignment and on the de-excitation cascade. The electromagnetic character of a $\gamma$-ray transition can be ascertained by measuring the linear polarisation of the photon using a Compton polarimeter. A Compton polarimeter provides a measurement of the scattering angle between the first and the second interaction point of the $\gamma$ ray in the detector. It is known that electric transitions favour perpendicular Compton scattering, while the magnetic ones favour parallel Compton scattering [Schl94, Sch98].

A Compton polarimeter consists of three Ge crystals, or scintillator detectors, one scatter and two absorbers. Existing Compton polarimeters, due to multiple scattering and absorption in the detector used as scatterer, have low efficiency. Segmented germanium

detectors can be used as Compton polarimeters, as shown in Fig. 2.21, with the advantage of a higher efficiency due to the reduction of dead material between scatterer and analyser and a better energy resolution.

# Chapter 3

# Gamma-ray tracking detector arrays

## 3.1 The development of detectors for nuclear spectroscopy

Progress in our understanding of the nuclear system has always been strongly associated with the development of increasingly powerful experimental instrumentation. The development of germanium semiconductor detectors and the subsequent construction of multi-detector arrays revolutionised the field of $\gamma$-ray spectroscopy. In the following, a brief history of semiconductor detector technology will be reported.

- In 1962 the first detector was made using a Ge(Li) crystal.
- In the 1970s, at the Niels Bohr Institute, several Ge(Li) detectors were used in an array [Bea96].
- In the early 1980s, progress in semiconductor technology allowed the fabrication of HPGe detectors.
- In the 1980s arrays made up of Compton suppressed detectors were constructed. Examples worldwide are TESSA (UK) [Twi83], HERA (USA) [Dia84], Nordball (Denmark) [Her85], $8\pi$ (Canada) [Tar83]. Compton suppressed arrays, with a total peak efficiency of 0.5-1.0% and a better peak-to-total ratio, provided a substantial improvement in the detection sensitivity [Nol94a]; the TESSA array boasted the discovery of

super-deformation in $^{132}$Ce [Nol85b] and $^{152}$Dy [Twi86].

- Further improvements in the total photopeak efficiency (up to ∼5%) were obtained with the construction of the GASP [Baz92, Ros93], and Eurogam I [Bec92, Bea92] arrays, consisting of 40 and 45 ESSs, respectively; using these devices identical superdeformed bands [Bec93, Fra96] and staggering of the dynamical moments of inertia [Has97] were observed for the first time.

- In 1990, the limited size of a germanium crystal (7 cm diameter), and the constraints associated with large Doppler broadening, led to the development of a new concept of germanium detectors: the composite detector. The first large array built with composite detectors was Eurogam II at CRN-Strasbourg (France), which comprised 24 Clover detectors and 30 standard single crystal detectors (Phase I), a total of 54 Compton suppressed detectors using of 126 germanium elements, and had a total photopeak efficiency of ∼8%.

- Presently, the state-of-art in nuclear physics instrumentation are the Gammasphere [Del88, Lee90, Mac94] and the Euroball [Sim97, Ger92] arrays, with a total photopeak efficiency of ∼10% and a P/T ratio of ∼60%. Euroball consists of 15 Cluster detectors at backward angles, 26 Clover detectors at 90° and 30 Phase I detectors at forward angles, for a total of 239 germanium elements; each detector is surrounded by a BGO shield. Gammasphere comprises of 110 detectors, each one 2-fold segmented. These arrays are optimised to study nuclear structure at high spin with heavy-ion induced fusion-evaporation reactions. In order to make further improvements in the sensitivity of such devices, a new concept in $\gamma$-ray spectrometry is required.

## 3.2 The observational limit

Modern experimental $\gamma$-ray spectroscopy requires the use of large detector arrays in order to maximise the photopeak efficiency and enable $\gamma - \gamma$ coincidence measurements to be performed. The knowledge of coincidence information is indeed fundamental to establish the relationship between the multiple $\gamma$ rays in a cascade following nuclear reactions. When discussing detector arrays, the following terminology is used:

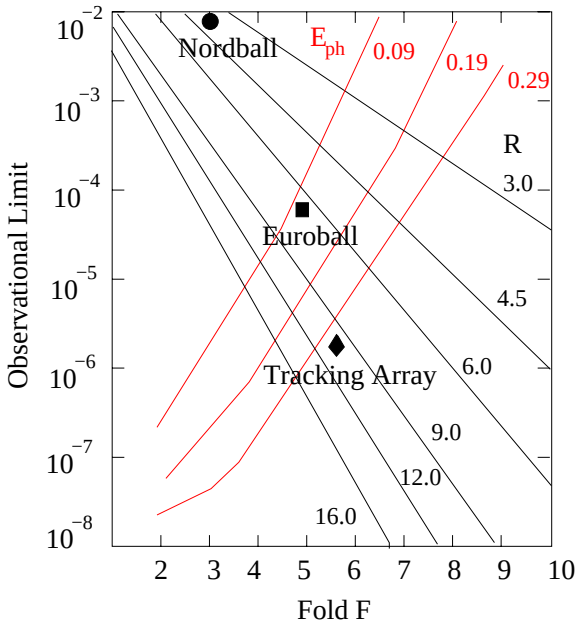


Figure 3.1: Observational limit for various values of the total photopeak efficiency and resolving power as a function of the fold. The observational limit for two existing arrays, Nordball and Euroball, is compared to the value predicted for a new array based on the concept of $\gamma$-ray tracking (taken from [Mih00b]).

- *Multiplicity*, $M_\gamma$, is number of coincident $\gamma$-ray transitions emitted during the decay of the excited nucleus to its ground state.
- *Fold*, $f$, is the number of detectors (or detector elements, in the case of multi-element detector arrays) that fire in coincidence and it is usually less than the multiplicity.
- *Single hit probability* is the probability of having a single $\gamma$-ray interaction inside one detector/element, for many incident $\gamma$ rays of multiplicity $M_\gamma$.
- *Multiple hit probability* is the probability of having a given number of $\gamma$-ray interactions inside the same detector/element.

In order to resolve a large number of closely spaced discrete $\gamma$-ray transitions, the concept of *resolving power* has to be introduced. The resolving power is defined as [Bea96]:

$$R = \frac{SE_\gamma}{\Delta E_\gamma^{total}}(PT), \tag{3.1}$$

where $SE_\gamma$ is the average energy separation between consecutive $\gamma$-rays transitions in a typical cascade, $\Delta E_\gamma^{total}$ is the energy resolution and PT is the peak-to-total ratio. In order to optimise the resolving power of the array, both the PT and the energy resolution have to be improved. A good peak-to-total ratio is of particular importance in the case of high fold coincidence data. Indeed, for a fold-$f$ event, the peak to total is given by $(\mathrm{PT})^f$.

Only peaks that stand above the background in the spectrum and that are statistically significant can be distinguished. The *observational limit* of an array is defined as the minimum intensity of a $\gamma$-ray transition that can be resolved. The concept of observational limit is discussed in the work of Gerl and Lieder [Ger92], in relation to the total photopeak efficiency and the resolving power of the array. In Fig. 3.1, the observational limit is plotted as a function of the fold number, for different values of efficiency and $R$. The details of the calculations are reported in [Bea96]. The plot shows that the contribution to the observational limit due to the resolving power increases as a function of the fold, while the contribution due to the photopeak efficiency decreases. The relative position of an array is given by the intersection of the appropriate pair of lines.

## 3.3 The concept of $\gamma$-ray tracking

The principle of an array built from Compton suppressed detectors is based on the rejection of the events corresponding to $\gamma$ rays that Compton scatter out of the germanium. Although the rejection of these events provides a better peak-to-total response, it unavoidably reduces the efficiency of the array. Furthermore, the space occupied by the BGO shield limits the Ge coverage, resulting also in a decrease of efficiency: in arrays such as Gammasphere, only about 56% of the solid angle is covered by germanium.

An ideal $4\pi$ shell of germanium, based on the recovery of photopeak events by adding-back the partial energy deposited in neighbouring detectors, provides a solution to overcome the efficiency limitation. A schematic view of an ideal Ge shell, of 15 cm inner radius and 9 cm thickness, built from 100-200 closely packed, encapsulated Ge detectors,

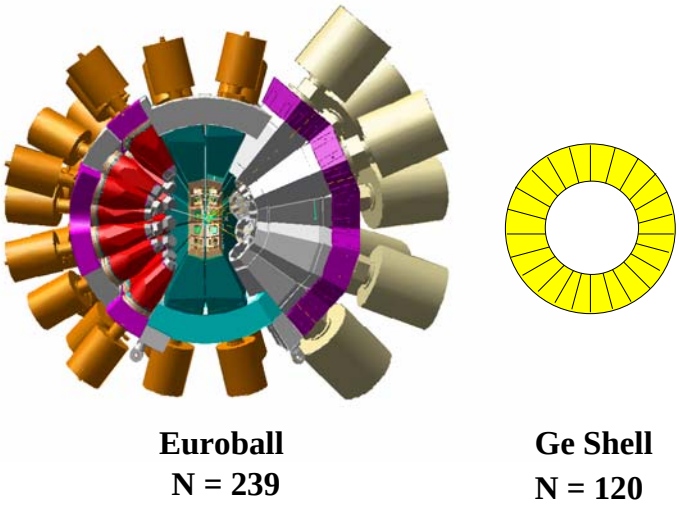


Figure 3.2: Cross-section of the Euroball array compared to a germanium Shell built from 120 closely packed detectors.

is shown in Fig. 3.2 compared to the Euroball array. In the case of $M_\gamma$=30, the expected efficiency of the Ge shell is ∼6.5% and the PT is ∼13%, as calculated in [Aga01]. This value compares with $\epsilon$ ∼6.5% and the PT∼37% of the Euroball array, under the same conditions. Despite the larger germanium coverage, the performance of the Ge shell is not better, actually it will have a PT three times worse than Euroball. The large probability of multiple hit events in the same detector and the scattering of $\gamma$ rays between adjacent detectors are the main reasons for such poor performance. The number of detector elements required to reduce the occurrence of multiple hits events in the same element is prohibitively expensive. The proposed solution is to use highly segmented Ge detectors such that all the interactions of every $\gamma$ ray could be resolved.

The new concept is based on $\gamma$-ray tracking [Lee99], this requires the complete reconstruction of the scattering path of the $\gamma$ ray inside the detector material. Tracking will allow the identification of $\gamma$ rays that Compton escape from the Ge and will enable the correct distinction between single and multiple hit events, avoiding the problem of incorrect summing.

At the time of writing, international efforts towards the development of $\gamma$-ray track-

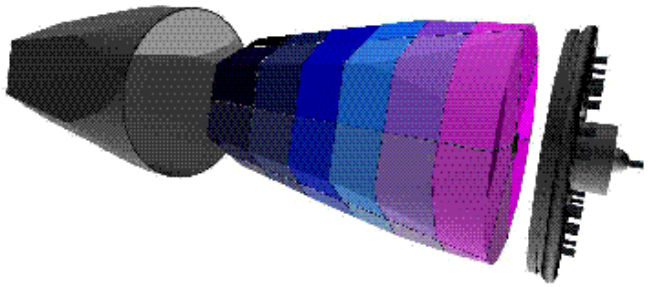

Figure 3.3: The 36-fold segmented, encapsulated Ge detector, as planned for AGATA.

ing arrays are focused around two main collaborations: GRETA (Gamma-Ray Energy Tracking Array) in the USA [Del99] and AGATA (Advanced GAmma Tracking Array) in Europe [Aga01]. Tracking arrays will provide excellent performance and, thanks to their improved observational limit (as presented in Fig. 3.1), they have the potential to enable the identification of incredibly weak reaction channels. In order to optimise the performance of a tracking array, many geometrical configurations have been investigated. The solid angle coverage and the thickness of the Ge shell are the parameters that mainly influence the detection efficiency (with present detector design a Ge coverage of ∼80% can be achieved). The proposal is to build a $4\pi$ array utilising Cluster type detectors, each consisting of three 36-fold segmented crystals with six-fold azimuthal and six-fold longitudinal segmentation, as shown in Fig. 3.3. The germanium crystal, 9 cm in length and 7 cm in diameter, with a circular shape at the rear and the shape of a tapered hexagon, at about $10^{\circ}$ angle, at the front, are used in order to form the optimum shell. The tapered geometry allows more space at the back of the detector and improves the charge collection properties in the front part, where the electrical field is very weak. A total of 180 hexagons together with 12 pentagons is proposed to form the AGATA ball, while for GRETA an equivalent geometry consisting of 110 hexagons and 10 pentagons, very similar to Gammasphere, has been suggested. Schematic geometries of the two arrays are presented in Fig. 3.4. The predicted

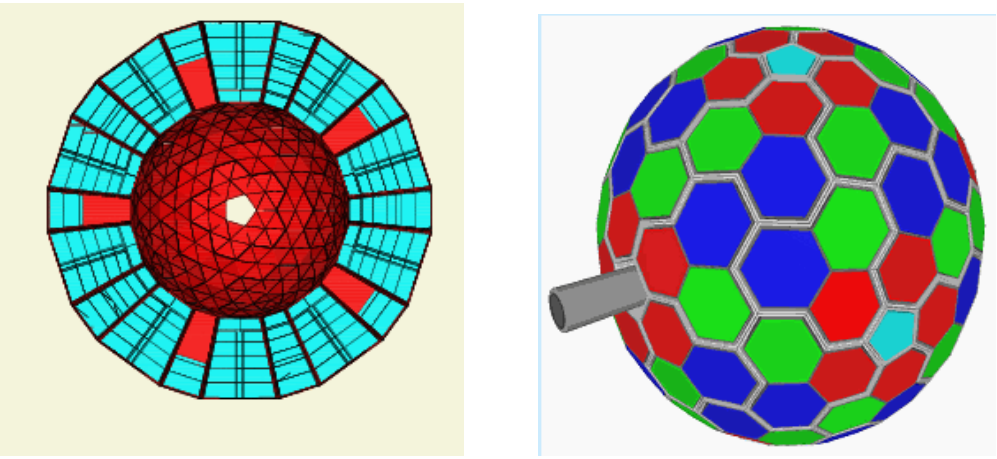

Figure 3.4: The geometrical configurations proposed for the GRETA (left) and AGATA (right) arrays.

performance of the AGATA array, as are reported in [Aga01], is shown in Tab. 3.1.

For a complete review on the concept of $\gamma$-ray tracking one can consult ref. [GRE] and references therein.

Tracking can be considered a two-step process:

1. The determination of the energies and the positions of all the individual interactions.

2. The identification of the interaction points that belong to the same $\gamma$-event and the reconstruction of their scattering sequence, based on a statistical approach utilising the application of the Compton scattering formula.

As explained in section 2.2, the absorption of $\gamma$ radiation in the material, although occurring via discrete interactions, can be considered as an instantaneous process. The Ge detector cannot distinguish the time relationship of the interaction process. However by comparing the energy deposition as a function of position to the Compton scattering formula, a solution is afforded. Two different approaches are currently being investigated.

1. The first algorithm is based on a preliminary clusterisation of the interaction points within a given angular separation, followed by an evaluation step to decide whether

| Detector properties specified for | | |
|---|---|---|
| Efficiency | $E_\gamma$=0.1 MeV, $M_\gamma$=1 | >70% |
| | $E_\gamma$=1 MeV, $M_\gamma$=1 | ∼50% |
| | $E_\gamma$=10 MeV, $M_\gamma$=1 | ∼10% |
| | $E_\gamma$=1 MeV, $M_\gamma$=30 | ∼25% |
| Peak-to-total | $E_\gamma$=1 MeV, $M_\gamma$=1 | 60-70% |
| | $E_\gamma$=1 MeV, $M_\gamma$=30 | 40-50% |
| Angular Resolution | $\Delta E/E<1\%$ | $<1^o$ |
| Maximum Event Rate | $M_\gamma$=1 | 3 MHz |
| | $M_\gamma$=3 | 0.3 MHz |
| Effective Granularity | | $\sim 10^5$ elements |

Table 3.1: Predicted performances for a $\gamma$-ray tracking array, as reported in [Aga01].

or not all the points in the cluster belong to the same $\gamma$ ray [Sch99, Baz00]. The most likely scattering sequence is determined by means of a least-squares minimisation of the energy-angle relation. An example of a scattering event consisting of three interactions is sketched in Fig. 3.5, where $E_1$ is the energy released by the energetic electron. The energy of the $\gamma^I$ ray is equal to $E_{\gamma^I} = E_\gamma - E_1$. In the case of an event consisting of N interactions (termed $E_{\gamma^I}$ the energy value obtained by using the Compton scattering formula (Eq. 2.3), and $E_{\gamma^I}^{meas}$ the measured value at the $n^{th}$ vertex) a $\chi^2$ value, to check the validity of the interaction sequence, is defined as:

$$\chi^2 \approx \sum_{n=1}^{N-1} W_n \cdot \left( \frac{E_{\gamma^I} - E_{\gamma^I}^{meas}}{E_\gamma} \right)_n^2 \tag{3.2}$$

where the energy of the incoming radiation is being used as standard deviation and $W_n$ is a weighting factor which takes into account the distance travelled by the $\gamma$ ray between the two points. The sum over all the vertices, up to the last Compton scattering, includes the N! possible permutations of the points, since their time sequence is not known. Ideally, clusters of correctly identified points, whose energies add to a photopeak event, should have a $\chi^2$=1. In practice, due to the finite energy and position resolution of the detector, the $\chi^2$ is different from unity even for good

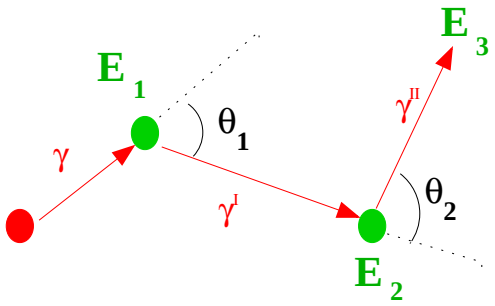


Figure 3.5: A schematic illustration of the scattering path of a $\gamma$ ray in the detector material.

clusters. This represents an unavoidable limitation to the reconstruction efficiency of the tracking algorithm. Since the absolute value of $\chi^2$ does not carry any physical meaning, an acceptance threshold on its distribution is set depending on the quality of the reconstructed spectra. The reconstruction efficiency of a tracking algorithm at a given $\gamma$-ray energy is measured as percentage of correctly identified events, i.e. those in the photopeak.

Typically, a higher $\chi^2$ threshold would give higher efficiency to the detriment of the peak-to-total. The reconstruction efficiency of tracking algorithm strongly depends on the position resolution; for efficient $\gamma$-ray tracking algorithms a position resolution of $\sim$1 mm is required [Vet01]. As tabulated in Tab. 3.1 for the possible AGATA array, a total photopeak efficiency of 25% and a peak-to-total of 50% is achievable for 1 MeV $\gamma$-ray energy and at a $M_\gamma$=30. This means that, in comparison with Gammasphere, whose photopeak efficiency under similar conditions is $\sim$8%, a gain of 3.75 in efficiency can be achieved even at a high $\gamma$-ray multiplicity.

2. The second method, known as the backtracking algorithm, consists of a preliminary identification of the last interaction point and then, by using the energy-angle relation of the Compton law, a backward reconstruction of the track up to the first interaction position [Mar99]. This method is based on the principle that the energy of the last photo-electric interaction, which terminates the Compton scattering sequence, is nearly constant and independent of the initial $\gamma$-ray energy. The performance of the backtracking algorithm is very similar to that of the clusterisation algorithm.

For the photoelectric and pair production interaction mechanisms, different tracking criteria apply. While no tracking criteria can be applied to low energy $\gamma$ rays directly absorbed by the photo-electric effect, pair production events are easily recognized from their characteristic signature: a point with energy $E_\gamma$-1.022 MeV and two $\gamma$ rays emitted back-to-back (see section 2.2).

Of particular interest, is the determination of the first and second interaction points:

1. The localization of the first interaction will enable a better Doppler correction to be performed.

2. The first and the second interaction point will help to determine the *linear polarization* of the $\gamma$ ray and therefore the parity of nuclear levels which have decayed.

Following the above discussion, the feasibility of performing $\gamma$-ray tracking relies on the achievable position resolution. Therefore one of the key aims of this work was to assess quantitatively detector performance in this area.

# Chapter 4

# Experimental measurements

## 4.1 Experimental setup

In order to resolve different $\gamma$ rays interacting in the detector volume and to reconstruct their scattering sequence, the total number of interactions, the 3D-position and the energy of every individual interaction has to be known precisely. The precision of $\gamma$-ray tracking is strongly correlated to the quality of this information. The experimental measurements carried out in this work relate to the 6×4 segmented prototype detector. The principal aims of the measurements were the characterisation of the detector performance using both conventional analogue and new digital electronics. In this section the experimental set-up used in the measurements will be described.

### 4.1.1 The 6×4 prototype detector

The Ortec prototype detector, named TIGRE (Tracking the Interaction of Gamma Ray Events), was delivered to the Oliver Lodge Laboratory in February 2001. Photograph of the detector and of the Ge crystal, before mounting in the cryostat, are illustrated in Fig. 4.1, while a schematic view of its geometry is presented in Fig. 4.2. TIGRE consists of a coaxial high-purity $n$-type germanium crystal, 65 mm diameter by 80 mm length, inside a 1 mm thick aluminium can of the same shape. The inner contact is $n^+$ lithium drifted (800 $\mu$m nominal thickness); the outer one is $p^+$ boron implanted (0.3 $\mu$m nominal thickness). The impurity concentration is not homogeneous along the crystal: it varies between $2.0\times10^9$ atoms/cm$^3$ in the coaxial (back) part to $1.5\times10^{10}$ atoms/cm$^3$ at the closed-end part (front).

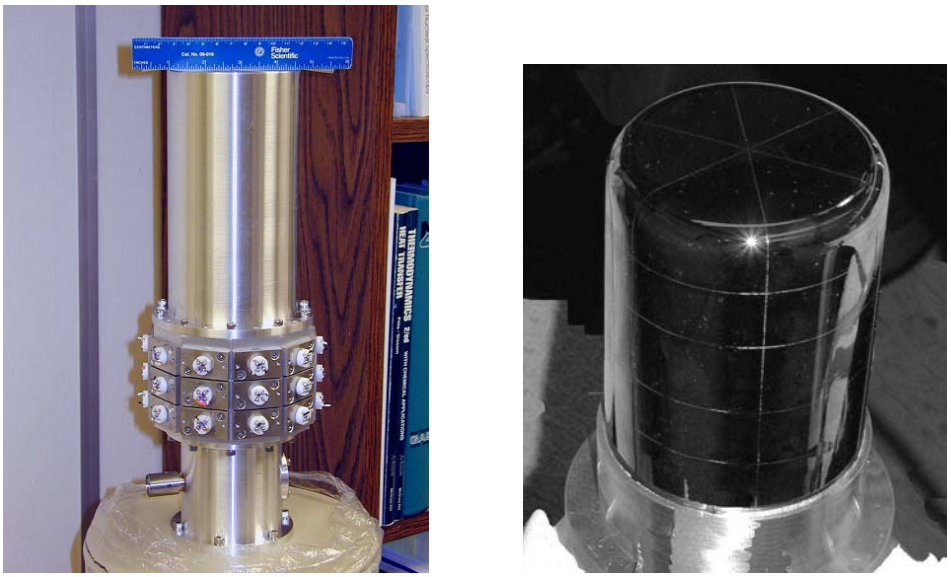

Figure 4.1: Photographs of the 6×4 prototype detector: the detector complete with the aluminium cryostat housing the crystal, the preamplifier board and the cryostat (left); the germanium crystal with the electrical segmentation pattern (right).

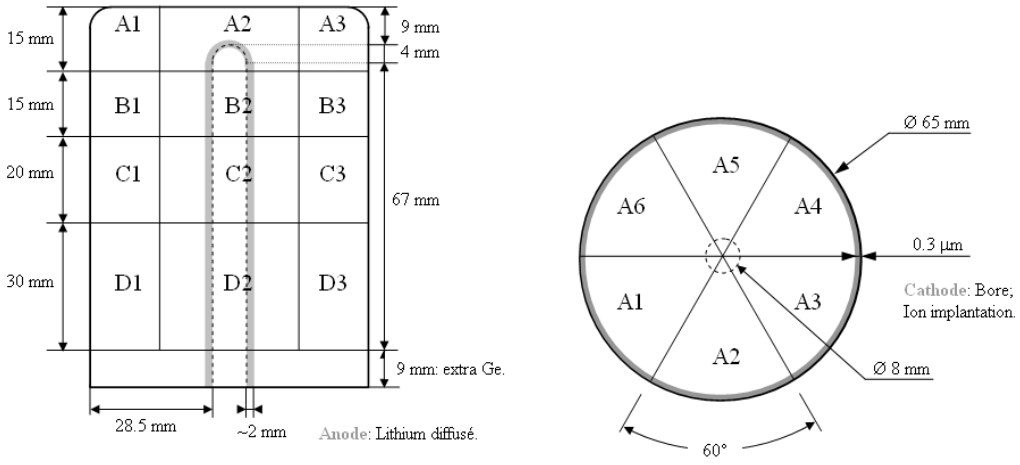


Figure 4.2: Geometry of the 6×4 prototype detector.

The outer electrode is segmented along two dimensions, six ways longitudinally and four ways in depth, which results in a total of 25 output electronic channels (twenty four outer segments plus the inner contact). The separation between adjacent electrodes is $\sim$150 $\mu$m. The inner contact has not been segmented, so it provides a convenient measure of the total energy deposited by the incident $\gamma$ radiation. In this work, the six vertical divisions are called *sectors*, enumerated from 1 to 6, while the four horizontal divisions are called *slices*, labelled A,B,C and D. The transverse segmentation planes are at different relative distances, namely 15 mm, 15 mm, 20 mm and 30 mm, starting from the front. This choice reduces the volume of the segments in the closed-ended part, where the electric field is not truly coaxial[1], and allows one to obtain a more equal count rate across the twenty four segments. The crystal is bulletised to improve the electrical field in the front of the crystal. Each contact is fitted with a fast charge sensitive preamplifier based on a design by the University of Cologne [Ebe00], provided with warm FETs. The gain of the preamplifiers is $\sim$250 mV/MeV for the outer contacts and $\sim$130 mV/MeV for the inner one. The outer contacts are connected to ground through DC coupled non-inverting preamplifiers and therefore their output signals have negative polarity. The inner contact is coupled through an AC non-inverting preamplifier and provides a positive polarity signal. Although warm, the FETs present low noise (about 2.5 mV peak-to-peak, corresponding to $\sim$10 keV) and good energy resolution performance. In mounting the preamplifiers, special care was taken in reducing the length and crossing of the electric wires, in order to minimise electrical cross-talk problems. The operating voltage is +3200 V to the centre contact, which corresponds to an electric field inside the detector sufficient for the charge carriers to reach the saturation velocity (see Fig. 2.12). There is only one preamplifier power supply requiring a +/-12 V line. Under operation, the detector is maintained at liquid nitrogen temperature. The dewar has a nominal holding time of 72 hours.

### 4.1.2 Digital signal processing system

In order to carry out pulse shape analysis of the detector signals, digital signal processing electronics is required. In this section, the features of a suitable digital signal processing sys-

[1]Special care was taken in manufacturing the detector; indeed the first transverse segmentation plane is placed at a point believed to mark the transition from the complex to the coaxial electric field.

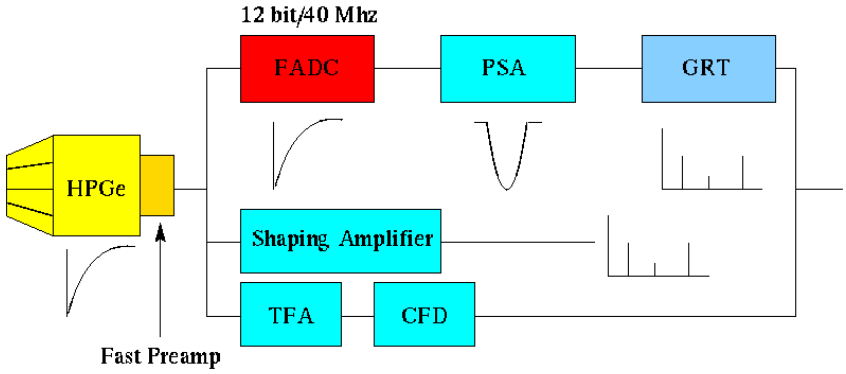


Figure 4.3: A block diagram representing the components of a digital signal processing chain, compared to the conventional analogue electronics solution. In the analogue electronics approach, the energy is extracted by means of a shaping amplifier and the time is obtained through a timing filter amplifier (TFA) and a constant fraction discriminator (CFD). In the digital approach, the preamplifier signal is digitized using FADC units; the data are processed by means of a pulse shape analysis (PSA) routine. The information provided is the input to a $\gamma$-ray tracking algorithm (GRT).

tem and its advantage over a conventional analogue electronics system will be summarised.

Digital signal processing is a technique based on a direct digitization of the detector preamplifier signal. This enables the extraction of the quantity of interest from the incoming data, the suppression of non-essential information and a consequent reduction of the incoming data stream to a manageable level [Kos99].

A block diagram of the digital signal processing electronics chain is presented in Fig. 4.3. To preserve all the relevant features of the pulse shape and to obtain the same energy resolution achievable with analogue electronics, the preamplifier signal must be digitized with a waveform digitizer (FADC, flash analogue to digital converter). Due to the characteristics of the preamplifier signals, i.e. high bandwidth and large dynamic range, FADCs with 12-bit amplitude resolution and a sampling rate of at least 40 MHz [Hub99] have been used.

The data are processed by means of a pulse shape analysis routine and the information provided is the input to a $\gamma$-ray tracking algorithm. The ultimate aim of the digital electronics system is to provide a hardware and software solution powerful enough to enable the implementation of pulse shape analysis routines in the DSP (Digital Signal Processor) or FPGA

(field programmable gate array) unit for on-line data reduction. The DSP and FPGA are devices used to perform digital filtering on the sampled ADC data in real time. A DSP is a specialised microprocessor, typically programmed in C, which is well suited to extremely complex mathematical tasks, with conditional processing. In contrast a FPGA is a device which contains a large number of gates ($\sim$0.2-8$\times 10^6$) and is programmed by connecting the gates together to form multipliers, registers, adders and so forth, using a proprietary programming language. The DSP can be programmed with fairly complex algorithms but it offers relatively slow speed operation. On the contrary the FPGA allows a high speed operation but it can be programmed only with relatively simple algorithms [Laz01]. Ideally, for each interaction point only five values should be extracted: the energy, the time and the three spatial coordinates. Each piece of information will require the application of different processing algorithms.

### 4.1.3 The scanning apparatus

In order to improve the position resolution of the detector by utilising pulse shape analysis, the relationship between the pulse shape and the interaction position has to be known quantitatively, i.e. the pulse shapes have to be calibrated with respect to the entry point of the $\gamma$ ray in the whole detector volume. This calibration is achieved by means of a scan of the detector. The technical details of the scanning system will be presented here; the experimental results will be discussed in a later section.
A schematic view of the scanning apparatus is displayed in Fig. 4.4. It consists of:

- A high resolution positioning system provided by Unimatic Engineers. The motorised table, arranged in a x-y axis configuration, consists of a Parker Automation positioning table (408012ST series) made of two independent sliders; each slider is built from a square rail bearing linear table of high quality aluminium alloy, protected with a black anodized surface finish; the surfaces are precision grounded to assure flatness. Each slider utilises a precise lead screw driven by a Pacific Scientific stepper motor. The stepper motor is operated by Parker PDFX15 indexer, which is computer controlled, enabling precise sequences of moves to be executed. Limit and home switches enable safe operation of the table and good reproducible positioning respectively. The moving profile can be programmed in software. The optimum position resolution of

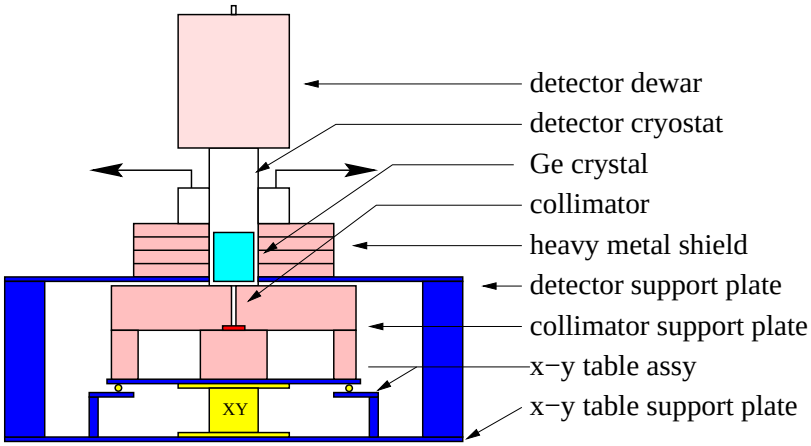


Figure 4.4: Schematic view of the scanning apparatus.

the system is 50 $\mu$m [Par00]. However for this work the table was configured with 100 $\mu$m resolution.

- A heavy metal collimator with a 2 mm diameter hole, inserted in a block of lead, 20 cm radius by 8 cm depth (see Fig. 4.5). The function of the collimator is to limit the portion of the detector which is irradiated.

- A 0.33 mCi $^{137}$Cs source, mounted inside the collimator. The choice of the source activity was made on the basis of the achievable good count rate, but taking into account the collimator performance.

- A detector holder provided with a lead shield of variable height (about 12 cm), to adjust the position of the Ge crystal with respect to the collimator top. The detector, the collimator and the x-y position table are supported by milled steel plates.

Despite the use of collimator and shield, designed to minimise the fraction of events which interact outside the region irradiated by the collimator, there is always a finite probability that unwanted background radiation will interact in the germanium. In order to minimise the background, only events depositing a full energy of 662 keV ($^{137}$Cs $\gamma$-ray energy) were considered. The main background source was environmental background due to $^{40}$K, at an energy of 1460 keV.

A simulation using the code Monte Carlo N-Particle (MCNP) [Mcn94] was carried out in

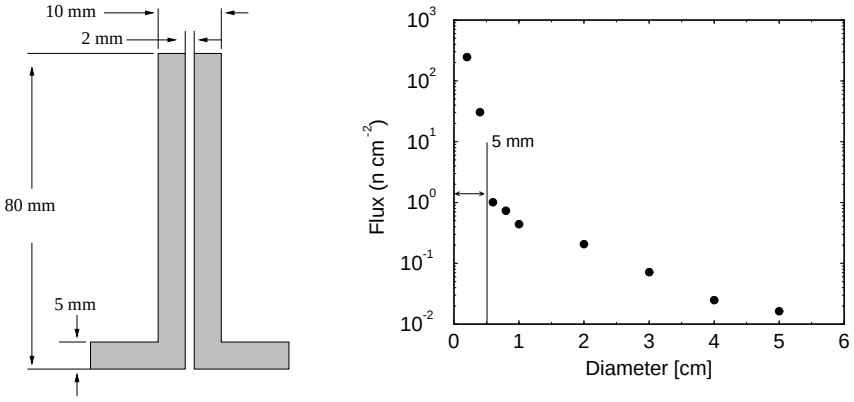


Figure 4.5: The geometry of the heavy metal collimator (left); the number of detected $\gamma$ rays as a function of the distance form the centre of the collimator (right).

order to investigate the effectiveness of the collimator design. MCNP is a general-purpose Monte Carlo code, which describes the photon transport in an arbitrary three dimensional configuration of materials. The definition of the collimator geometry and the $^{137}$Cs source was included in the code. The flux of $\gamma$ rays as a function of position was calculated. The results presented in Fig. 4.5 show the numbers for the 0.3 mCi source. The number of counts drops considerably away from the collimator hole and the spread of the radiation from the collimator has a FWHM of $\sim$5 mm at a source-detector distance of 10 cm.

**Electronics**

For pulse processing, twenty-five channels of fast digital signal processing electronics are required. Eighteen channels are provided by three cM62 cards of six channels each, fitting into a compact PCI (Peripheral Component Interconnect) crate [Inn00a]. For the other seven channels a Joerger Enterprises, Inc. Model VTR10012 VME card installed in a VME crate [Joe02] has been used.

Each cM62 card has one Texas Instruments DSP and three OMNIBUS slot AD40 cards, with two channels each, connected as plug in modules [Inn00b]. A simplified block diagram of a cM62 card is shown in Fig. 4.6. Each channel of the AD40 module consists of a low distortion input amplifier, a 12-bit dynamic range - 40 MHz sampling ADC and a FIFO (First In First Out) 1k Sample circular buffer, to allow efficient data collection and

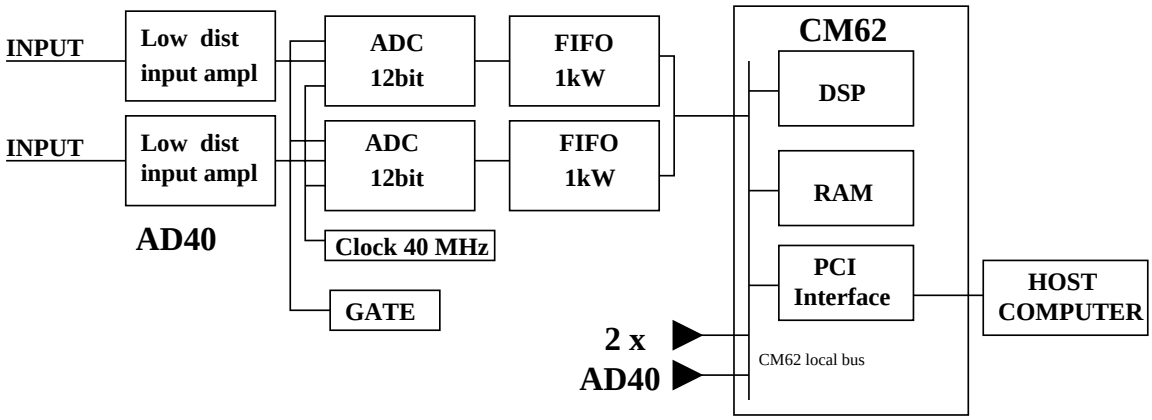


Figure 4.6: Block diagram of a cM62 card, showing two channels provided by an AD40 module.

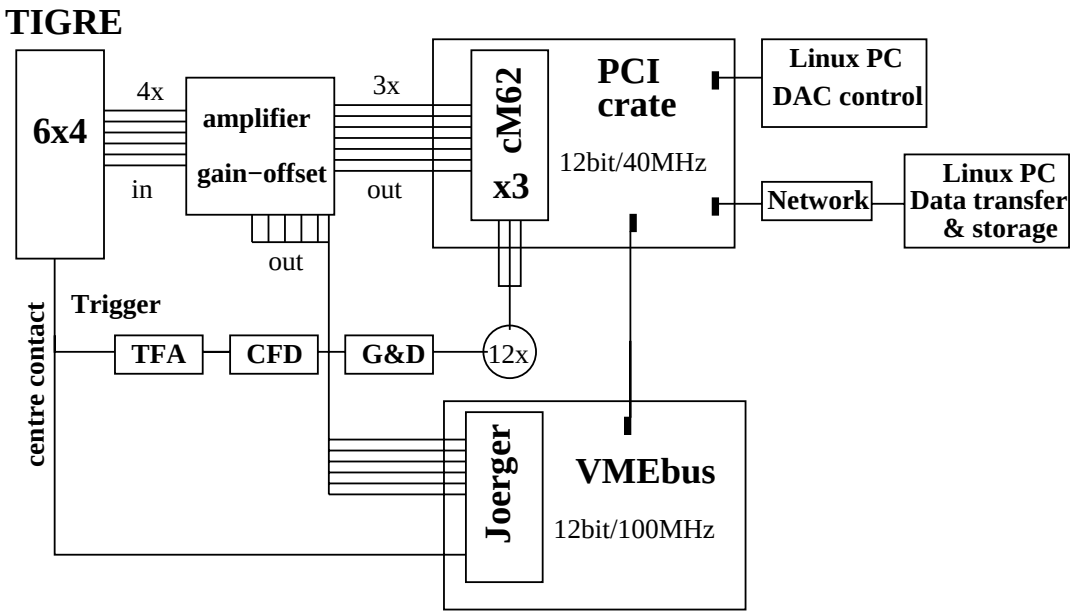


Figure 4.7: Schematic view of the data acquisition system.

transport to the host DSP card. The DSP can collect the data from the AD40 as either single points to minimise latency, or as data set (up to the full FIFO size) to minimise the interrupt rate to the host computer. Additional on-board logic supports pre-triggering, in which the FIFO is continuously refilled with fresh conversions until an external gating event is detected, after which a programmable number of samples are acquired. When the trigger occurs, a user-specified number of samples are saved in the input FIFO as the pre-triggering information, after which new samples are retained until the FIFO fills. Data acquisition for each channel may be inhibited until the input level exceeds a programmable voltage threshold, after which acquisition is enabled.

The Joerger card uses a 12-bit dynamic range - 100 MHz sampling ADCs. The module has an on board SRAM memory of 1k sample per channel and it can also operate in pre-triggering mode.

Both the cM62 and the Joerger cards were used with an external trigger, provided by the centre contact signal from TIGRE. The trigger was formed by utilising a timing filter amplifier (TFA) followed by a constant fraction discriminator (CFD), with an optimal CF delay of 100 ns. In order to minimise the background, an appropriate threshold of the CFD, was chosen. The threshold was set below the 662 keV $\gamma$-line, to limit the data acquisition to events fully absorbed in the detector volume. In this condition, the maximum trigger rate was 50 cps. The background rate was 8 cps.

For each channel, 512 data samples were recorded. The sampling window for the cM62 (40 MHz) was therefore 12.8 $\mu$s, while for the Joerger card (100 MHz) it was 5.12 $\mu$s. The trigger point was chosen as 64 samples into the sampled signal. The input coupling was 50$\Omega$/DC. The 12 bit y-range corresponds to 4096 arbitrary units of magnitude digitized over +1 V to -1 V. This results in a FADC sensitivity scale of 0.5 mV per unit. Before being sampled, the detector signals were amplified by a factor of five and the DC offset was removed in hardware[2]. This enabled the full dynamic range of the FADCs to be exploited. The typical amplitude of the preamplifier outer contact signals were $\sim$160 mV at 662 keV, before the amplification step, and $\sim$800 mV, after amplification. The amplitude of the centre contact signal was $\sim$80 mV before, and $\sim$430 mV after amplification.

Control, data acquisition and storage tasks were performed via a PC work station. An

[2]Due to the large DC offset of contact B5 (-308 mV before amplification), this channel was not amplified.

| Contact | Offset [mV] | Gain [mV/MeV] | Contact | Offset [mV] | Gain [mV/MeV] |
|---|---|---|---|---|---|
| A1 | +50 | 234 | C1 | -10 | 276 |
| A2 | -262 | 262 | C2 | -220 | 245 |
| A3 | -220 | 271 | C3 | -214 | 267 |
| A4 | -224 | 282 | C4 | -230 | 239 |
| A5 | -240 | 277 | C5 | -198 | 260 |
| A6 | -210 | 251 | C6 | +15 | 253 |
| B1 | -183 | 264 | D1 | -165 | 233 |
| B2 | -226 | 274 | D2 | -220 | 278 |
| B3 | -204 | 238 | D3 | -230 | 239 |
| B4 | -230 | 254 | D4 | -390 | 288 |
| B5 | -308 | 267 | D5 | -210 | 251 |
| B6 | -250 | 271 | D6 | -167 | 245 |

Table 4.1: Gain and offset values of the outer contact preamplifiers.

overall view of the data acquisition system is shown in Fig. 4.7. The data acquisition system utilised the MIDAS software system. A preliminary analysis of the data was performed on-line using the MIDAS MTsort program [Sam00].

## 4.2 Detector performance

In this section the experimental measurements performed on the 6×4 detector are reported. The first part discusses the testing of the detector, carried out mainly by means of conventional analogue electronics; in particular, results on energy resolution, detection efficiency, preamplifier response and noise characteristics will be presented. The second part discusses the analysis of the scan data: the performance of the acquisition system, the quality of the digitized data and the accuracy of the collimation system are tested. The detector response to a radiation event in terms of segment sensitivity and the scattering profile between adjacent segments will be discussed.

The first characterisation of the detector was to measure the preamplifier gain and offset values, as reported in Tab. 4.1.

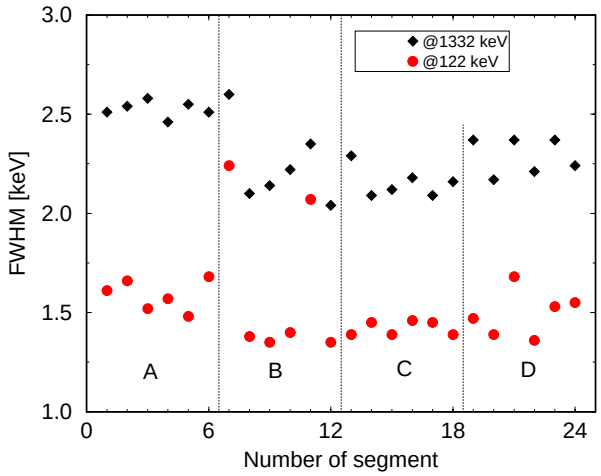


Figure 4.8: Energy resolution results for the 24 position channels of the 6×4-fold detector at 122 keV and 1332 keV. The measurements have been taken by using a shaping time constant of 6 $\mu$s on the spectroscopy amplifier.

### 4.2.1 Energy resolution measurements

The detector energy resolution has been characterised, using two sealed radioactive sources, a $^{60}$Co and a $^{57}$Co source, by calculating the FWHM of the photopeak at 1332 keV and 122 keV, respectively. In order to reduce any microphonic effects due to mechanical vibrations, the detector was placed on a sponge layer. The preamplifier output from the detector was amplified and shaped using a spectroscopy amplifier (Ortec mod. 671). The output was fed into a multi channel analyser, which consisted of an Ortec 8k TRUMP ADC card and the Ortec Maestro software version 4.2.

In order to ensure statistically reproducible results, 1000 counts in the peak channel were required for each measurement. The spectroscopy amplifier allows either Gaussian or Triangular shaping and a variety of time constants. The Gaussian shaping mode and a time constant of 6 $\mu$s provided the best results.

The measurements were first performed by connecting only one signal cable and then repeated, with all six channels of the same slice connected. The two sets of measurements provided consistent results, both in terms of the position of the peak centroid, which appeared in the same ADC channel number, and in terms of the FWHM. This demonstrates

that the electronic channels have good gain stability: capacitive load on a preamplifier channel does not affect the performance of the other electronic channels.

Energy resolution results for the 24 position signals are reported in Tab. 4.2 and displayed in Fig. 4.8. The measured energy resolution of the outer contacts ranges from ∼2.1 keV to ∼2.5 keV. The segments in slices A and D have the worst energy resolution. As described above, due to the geometry of TIGRE, at the closed-ended part and at the back part of the detector the electric field is not coaxial; at the closed-ended part the electric field is very weak, at the back part it is complex. The electric field distribution influences the charge collection process and, consequently, the energy resolution of the detector. The resolution of the inner contact has always been very poor (3.9 keV) since the detector was manufactured.

### 4.2.2 Efficiency measurements

The relative efficiency of the TIGRE detector was measured using conventional analogue electronics. A value of 64% was measured for the 1332 keV $\gamma$ ray in $^{60}$Co at 25 cm source-detector distance. The experimental uncertainty was $\leq$6%, mainly due to the uncertainty in the source position.

Efficiency measurements at a 25 cm distance were repeated as a function of the $\gamma$-ray energy, using various sources ($^{152}$Eu, $^{133}$Ba, $^{88}$Y and $^{241}$Am). The trend of the efficiency curve is presented in Fig. 4.9. The fit of the data has been performed with the program EFFIC [Hao90].

### 4.2.3 Preamplifier response

A fundamental characteristic for a tracking detector is the fast response of the preamplifier circuit. The preamplifier response of the TIGRE detector was measured using a precision pulse generator providing a step function with a 2 ns leading edge. The rise time was measured as the time the pulse takes to grow from 10% to 90% of its final amplitude, using a fast *HP Infinium* scope with a sampling frequency of 1 GHz. The value obtained from the preamplifier output pulse was 29 ns. The measurement refers to the centre contact signal, the only one provided with a test input. The shape of the preamplifier output signal is shown in Fig. 4.10. From this result, it can be concluded that the detector preamplifiers

| Contact | FWHM [keV][1] | FWTM [keV][1] | FWHM [keV][1] | FWTM [keV][1]) |
|---|---|---|---|---|
| | 1332 keV | | 122 keV | |
| A1 | 2.51 | 4.70 | 1.61 | 3.13 |
| A2 | 2.54 | 5.15 | 1.66 | 2.97 |
| A3 | 2.58 | 4.91 | 1.52 | 2.78 |
| A4 | 2.46 | 4.76 | 1.57 | 2.66 |
| A5 | 2.55 | 5.00 | 1.48 | 2.68 |
| A6 | 2.51 | 4.92 | 1.68 | 3.26 |
| B1 | 2.60 | 5.01 | 2.24 | 3.60 |
| B2 | 2.10 | 3.78 | 1.38 | 2.53 |
| B3 | 2.14 | 4.10 | 1.35 | 2.57 |
| B4 | 2.22 | 4.13 | 1.40 | 2.58 |
| B5 | 2.35 | 4.78 | 2.07 | 3.75 |
| B6 | 2.06 | 3.87 | 1.35 | 2.62 |
| C1 | 2.19 | 4.06 | 1.39 | 2.63 |
| C2 | 2.09 | 4.21 | 1.45 | 2.68 |
| C3 | 2.12 | 3.91 | 1.39 | 2.68 |
| C4 | 2.18 | 4.17 | 1.46 | 2.72 |
| C5 | 2.09 | 4.18 | 1.45 | 2.68 |
| C6 | 2.16 | 4.13 | 1.39 | 2.59 |
| D1 | 2.37 | 4.34 | 1.47 | 2.76 |
| D2 | 2.17 | 4.32 | 1.39 | 2.61 |
| D3 | 2.37 | 4.44 | 1.68 | 3.15 |
| D4 | 2.21 | 4.16 | 1.36 | 2.63 |
| D5 | 2.37 | 4.43 | 1.53 | 2.86 |
| D6 | 2.24 | 4.43 | 1.55 | 2.95 |

Table 4.2: Energy resolution results at 122 and 1332 keV for the outer contact signals. [1] Uncertainties on the energy resolution measurements are typically $\leq$5 %.

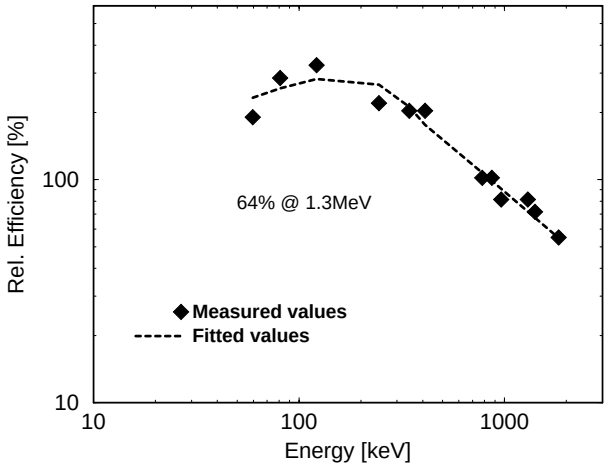


Figure 4.9: Relative efficiency curve as a function of the $\gamma$-ray energy.

[1] Uncertainties on the energy resolution measurements are typically $\leq$6 %.

are fast enough to enable time variations larger than 30 ns to be distinguished; this time resolution is sufficient for measuring variations in the the signal rise time, which, for the TIGRE detector, is of the order of 200 ns.

By substituting the calculated rise time in Eq. 2.42, one obtains a preamplifier bandwidth of 12 MHz, which is in good agreement with the preamplifier specifications (12.5 MHz).

### 4.2.4 Noise evaluation

A detailed Fourier analysis of the preamplifier signal allows one to distinguish between the various contributions of noise and to configure the detector in order minimise their influence [Pre99]. The noise response of the detector is discussed in terms of the integrated power spectrum as a function of frequency [Vet00].

Fig. 4.11 displays an example of a typical outer contact noise signal, its power spectrum and the corresponding integrated power. The noise signal corresponds to the time dependent charge amplitude measured from a contact not participating in the $\gamma$-ray charge collection. The signal was digitized with a 12 bit/100 MHz FADC. In the picture,

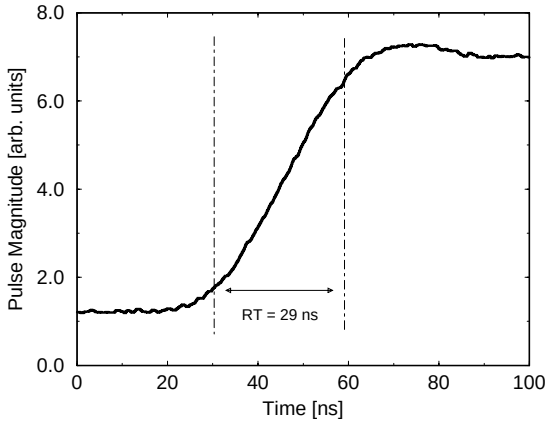


Figure 4.10: The centre contact preamplifier response to a precision pulses generator digitized with a fast scope having a sampling frequency of 1 GHz.

the signal amplitude has been converted from arbitrary units into keV by considering the gain of the preamplifier/amplifier chain[3] (see Tab. 4.1). The peak-to-peak noise is ∼2.5 mV, which corresponds to a noise level of ∼5 keV.

The power spectrum as a function of frequency $f$ is given by the amplitude of $\widetilde{s}(f)$, the Fourier transformation of the signal function $s(t)$:

$$\widetilde{s}(f) = \int_{-\infty}^{\infty} s(t) e^{2\pi i f t} dt, \tag{4.1}$$

while the integrated power has been calculated as:

$$P(f) = \int_{-\infty}^{\infty} |\widetilde{s}(f)|^2 df. \tag{4.2}$$

With reference to Fig. 4.11, the integrated power increases linearly with the frequency up to 13 keV$^2$ (3.6 keV) at a frequency of 15 MHz, then it starts saturating until it reaches the plateau value of 20 keV$^2$ (4.5 keV). This noise characteristic reflects the white noise contributions in the frequency range of the preamplifier bandwidth, predominantly given by electronic noise in the FET and by the detector capacitance [Gou72]. The plateau value determines the overall noise in the system and therefore provides a low energy threshold

[3]The preamplifier has a gain of ∼250 mV/MeV, while the amplifier used in the electronics chain before the digitization step has a factor five amplification and a bandwidth of 200 MHz, which, being larger then the sampling frequency of the FADC, does not influence the frequency analysis.

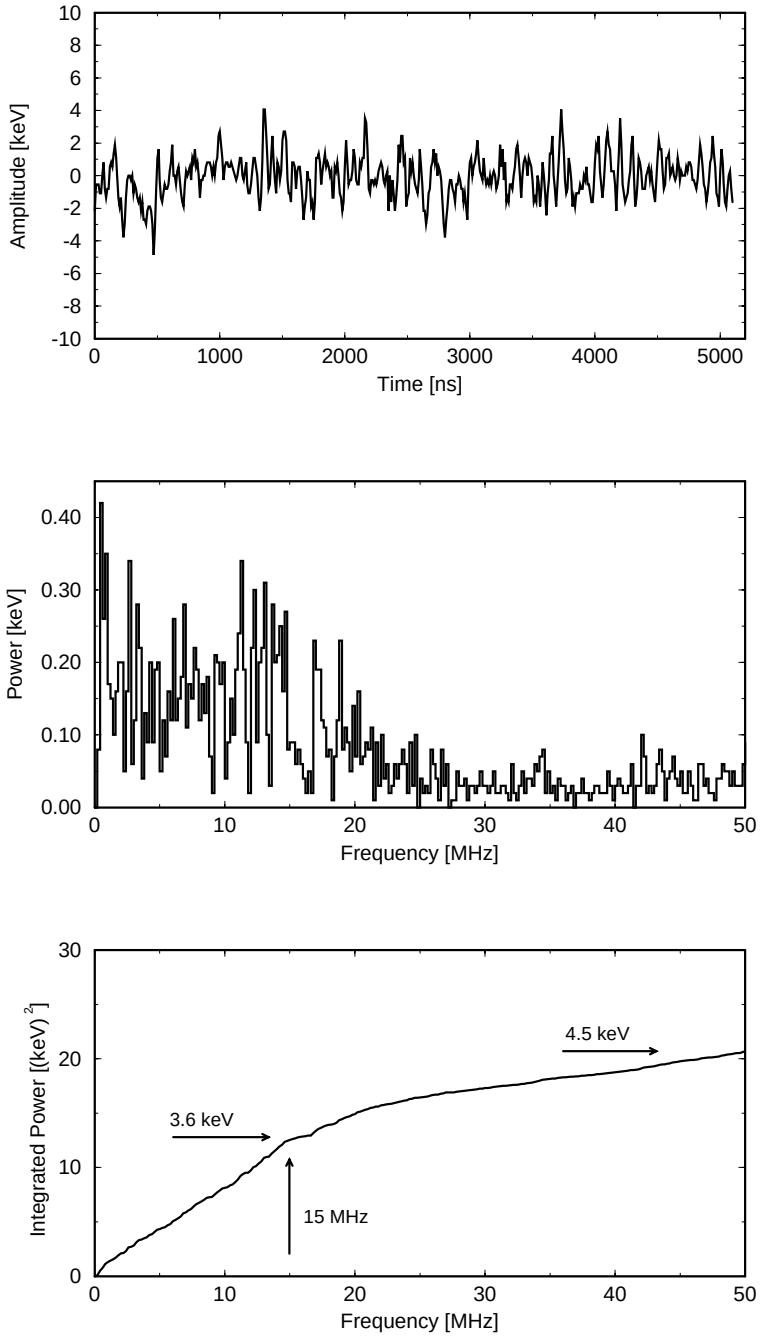


Figure 4.11: Noise signals from a typical outer contact preamplifier, digitized with a 12 bit dynamic range FADC at a sampling rate of 100 MHz (top), its power spectrum (middle) and its integrated power(bottom).

for the identification of a real charge event in a segment. An integrated noise contribution of 4.5 keV is a very good result for a warm FET preamplifier. The results for a cold FET preamplifier are reported in [Vet00]. However, due to the different configuration of the preamplifiers and internal wiring, a direct comparison it is not possible.

## 4.3 The scan

The response function of the detector was calibrated as a function of position. In this section results on the charge collection properties and on the electric field distribution inside the detector will be discussed, while results on position determination will be reported in section 5.6.1.

### 4.3.1 Experimental Details

The front face of the detector was irradiated by moving the collimated source in two dimensions, horizontally. Prior to a detailed scan, a coarse surface scan was performed in 5 mm steps with a rectangular profile, in order to define the coordinates of the indexer which were required to scan the detector. The acquisition time at each position was 3 minutes. This test scan also enabled the calibration of the table position with respect to the centre of the detector and to check the statistics at each position.

A finer scan was then performed using 2 mm steps and 5 minutes at each position. A rectangular profile was used and data from a total of 1520 positions were collected. A total of 210 GBytes of data were recorded in five days. The data were recorded onto five DLT40/80 tapes.

### 4.3.2 The detector response to radiation events

It is useful to introduce the concept of *detector sensitivity* as a tool to study the response of the detector to radiation events. The detector sensitivity is defined as the number of full-energy events recorded over a given time window. The sensitivity of the detector is non-uniform within the germanium volume. Variations in the detection sensitivity are due to crystallographic properties of the Ge crystal (impurity concentration and possible lattice defects), the electric field distribution and the penetration distance of the $\gamma$ radiation in Ge

($\gamma$ rays interacting close to the edge of the crystal are more likely to Compton scatter out of the germanium material before being fully absorbed).

Maps of the detection sensitivity were obtained by plotting the number $\gamma$-ray events, which meet some trigger requirement, as a function of the interaction position. The $\gamma$-ray events were selected by using two kinds of selection criteria (*gates*):

1. A gate on the $\gamma$-ray energy measured both on the centre and the outer contact signals. The energy information was extracted from the number of digitized pulse by means of the pulse shape analysis routine, discussed in section 5.3; energy spectra were created for each contact signal. The energy gate was then set as an energy window around the region of the spectrum of interest.

2. A gate on the position of the scanning table, to ensure that the energy absorption occurred in the sector facing the source.

Fig. 4.12 shows the sensitivity map measured from the centre contact signal. Only an energy gate on the centre contact signal was used to select the 662 keV $\gamma$-ray events occurring in the detector volume. The sensitivity map has been plotted in two graphical representations, a 3D-surface map (top) and a 2D-contour map (bottom); in the latter the number of counts is indicated by the colour scale. From the plot, the shape of the germanium crystal, the centre contact hole and the crystal edges are clearly distinguishable. This plot provides also an important check on the data acquisition system performance. From a visual inspection of the plot, the number of counts as a function of position are consistent with the detector geometry.

The energy spectra were obtained from the centre contact signal and from the outer contact signals of sector one. The results, presented in Fig. 4.13, show the response of the detector to 662 keV $\gamma$ rays. The centre contact signal and the outer contacts A1 and D1 manifest low energy tails. Such a response is not observed in contacts B1 and C1. The low energy tail arises from photopeak events, whose energy has not been fully collected at the electrodes, either because of crystal defects providing charge trapping [Sze95c] or because the electric field is not strong enough to allow all the charge carriers to reach the destination electrode. The latter case is likely to be responsible for the incomplete charge collection observed in the TIGRE detector.

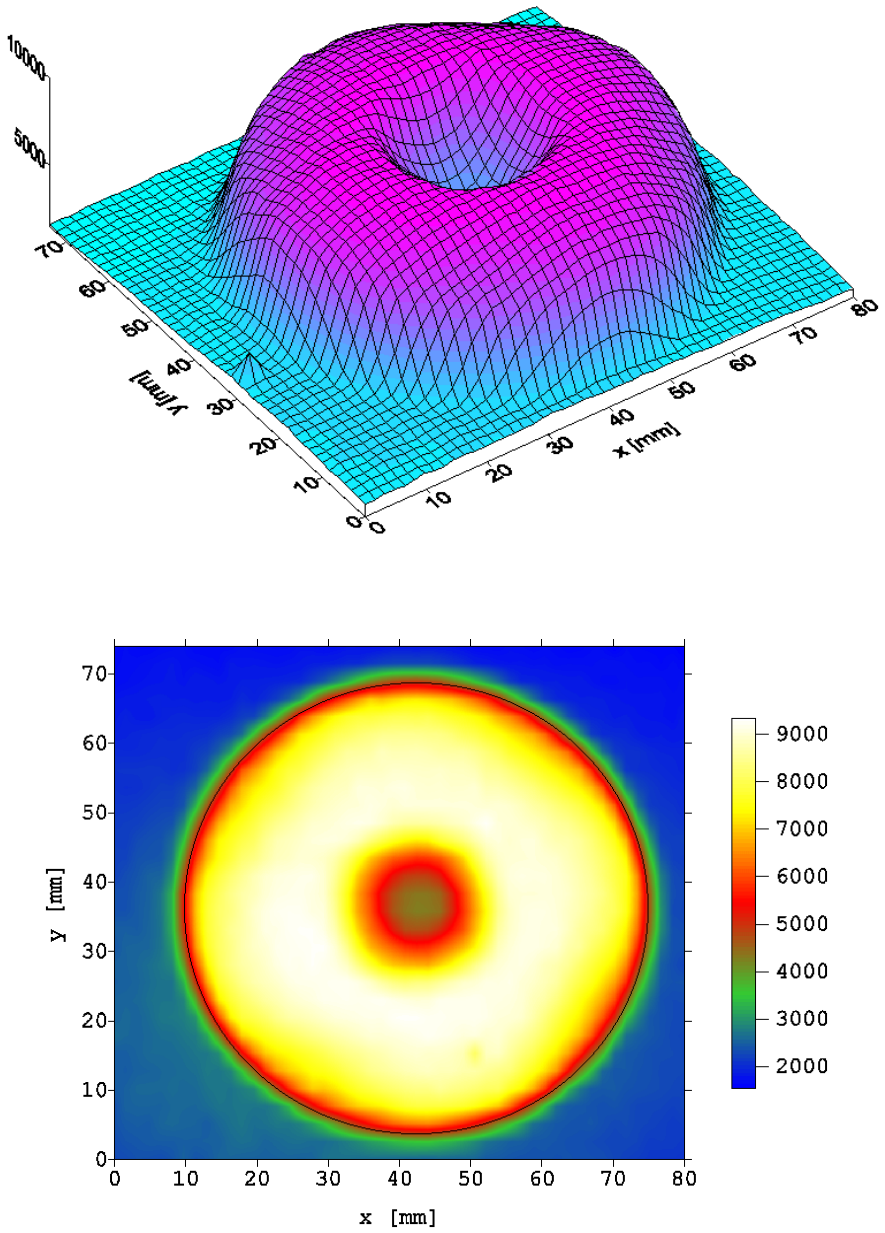


Figure 4.12: Sensitivity map of the 6×4 detector to full energy events. The top part shows the number of 662 keV events as a function of the source position in a 3D-surface map representation, while the bottom part shows a 2D-contour map, where the number of counts is given by the colour scheme.

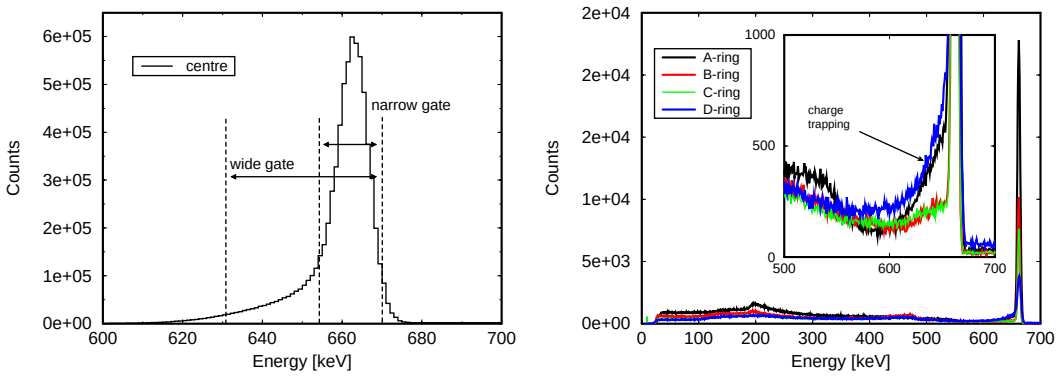


Figure 4.13: Energy spectra measured from the centre contact (left) and from typical outer contact signals, namely A1, B1, C1, D1. The narrow and the wide gate widths are indicated. The low energy tail of the full energy peak from A1, D1 and from the centre contact signals can be attributed to incomplete charge collection.

In order to investigate the influence of incomplete charge collection on detector response, sensitivity maps for each individual segment were produced using different gate widths around the photopeak energy (as indicated in Fig. 4.13). Results are summarised in Tab. 4.3 and the corresponding figures. On the sensitivity plots, the most probable crystallographic directions, labelled by Miller indices, are indicated. These directions have been empirically obtained on the basis of the discussion reported in section 2.6.1.

The results show that the response of a segment in the front slice of the detector is clearly different from the other segments. The overall number of counts systematically decreases from slice A to slice D, due to the different efficiency of the four slices for a $\gamma$ ray of 662 keV[4]. In the middle slices (B and C) the sensitivity is axially symmetric; in the front (A) and in the back (D) slices, near the crystal edge, there are regions with a much lower number of counts, whose sensitivity depends on the applied gate width. In the worse case, in slice A the number of counts drops by a factor of 6 ( see Fig. 4.14), and in slice D a ring of $\sim$5 mm thickness at the crystal edge presents a count rate comparable to the background. If this phenomenon is due to incomplete charge collection, a more uniform sensitivity among the

[4]Although the geometry of the detector was designed with different separation distances between the horizontal segmentation planes, in order to have almost uniform count rate over all the 24 segments, the probability of having a photopeak event in slice A at 662 keV is higher than in the back segments.

| Energy gate on centre | Energy gate on outer | Position gate | Figure |
|---|---|---|---|
| wide | no | no | 4.12 |
| narrow | wide | yes | 4.14 |
| wide | wide | yes | 4.15 |
| wide | narrow | yes | 4.16 |

Table 4.3: The table summarises the sensitivity results obtained for each slice of the detector, using different gates on the energy of centre and outer contact signal. A *wide* gate indicates an energy window of 50 keV around the 662 keV $\gamma$-line, a *narrow* gate defines an energy window of 15 keV (see Fig. 4.13).

segment area would be obtained with a wider energy gate on the centre contact: those events whose energy has been only partially collected would be recovered in the spectrum. This effect is indeed observed in Fig. 4.15 for slice A. The electric field in the closed-ended part of the detector is non-coaxial, in particular, the edges of the detector experience a weaker electric field ([Krö01], [Mih00]). In these regions the free charge carriers created by the $\gamma$-ray interaction can recombine (or, less likely, be trapped) before reaching the destination electrode. The charge is therefore not fully collected by either electrode. The effect is most marked along the $\langle 110 \rangle$ crystallographic direction due to the smaller drift velocity of the charge carriers along that direction (see section 2.6.1).
The situation is different in the back slice of the detector, where the sensitivity behaviour is influenced by the width of the energy gate on the outer contacts, but not by the width of the energy gate on the centre contact. Due to the clamp at the back of the detector, the electric field at the back of slice D is complex. For technical reasons, the outer contacts were made 9 mm shorter than the effective length of the crystal (see Fig. 4.17). Events interacting in the back corners are detected by the centre, but not by the outer contact, therefore the photopeak efficiency at the edge of slice D is lower than expected if a narrow gate is applied on the outer contact energies.

The response of the detector to Compton scattered events has also been investigated. Compton scattered events were selected by requiring that the energy deposition in one segment was in the Compton range (between 20 keV and 650 keV). Sensitivity maps for

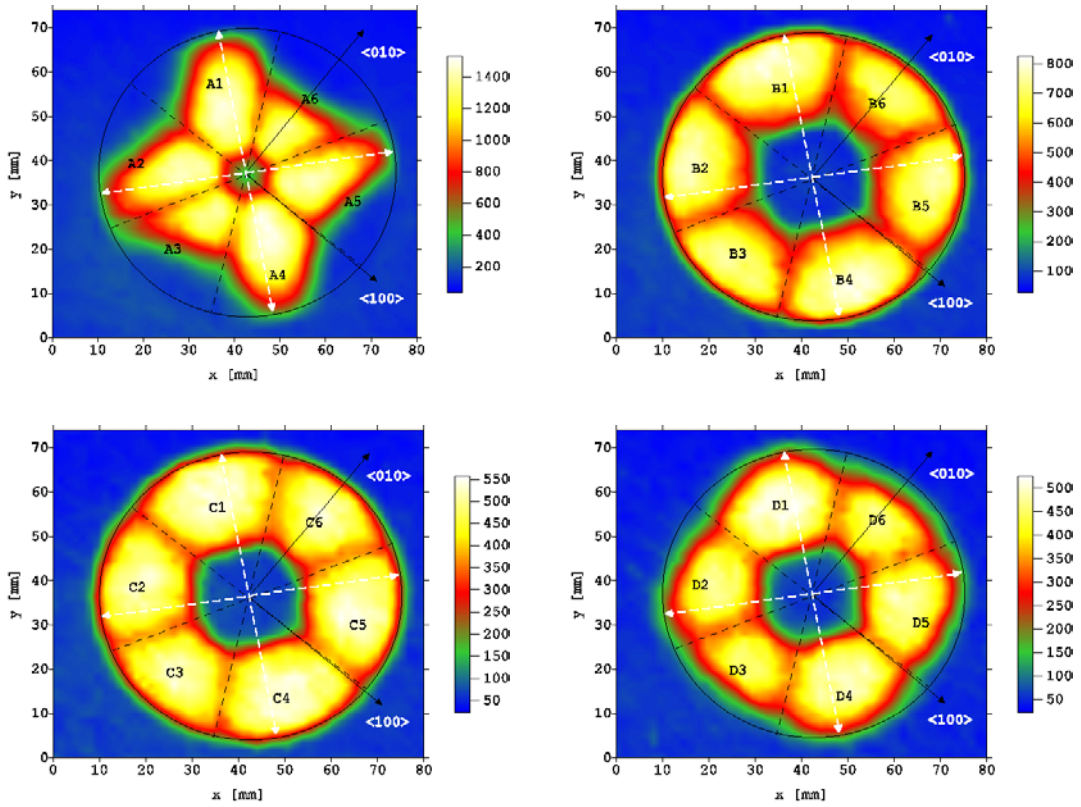


Figure 4.14: Maps of the segment sensitivity for slice A (top left), slice B (top right), slice C (bottom left) and slice D (bottom right). The photopeak events were selected using a narrow energy gate on the 662 keV $\gamma$-ray line from the centre contact and a wide energy gate on the 662 keV $\gamma$-ray line from the outer contacts. The white arrows indicate the probable crystallographic directions labelled by the Miller indices.

each detector slice are reported in Fig. 4.18. Compton scattered events between adjacent segments are more likely to occur near to the segment boundaries. The number of counts, in a $\sim$5 mm region around the segment boundaries, is about a factor 1.2 higher than in the middle of the segment. Again, slice A manifests a different behaviour: Compton scattered events are more focused towards the centre and the hole corresponding to the inner electrode is less distinguishable. This is expected, since the hole for the centre electrode occupies only a small part of slice A.

In order to characterise further the dependence of the detector sensitivity on the electric field, sensitivity maps were produced as a function of the interaction depth within

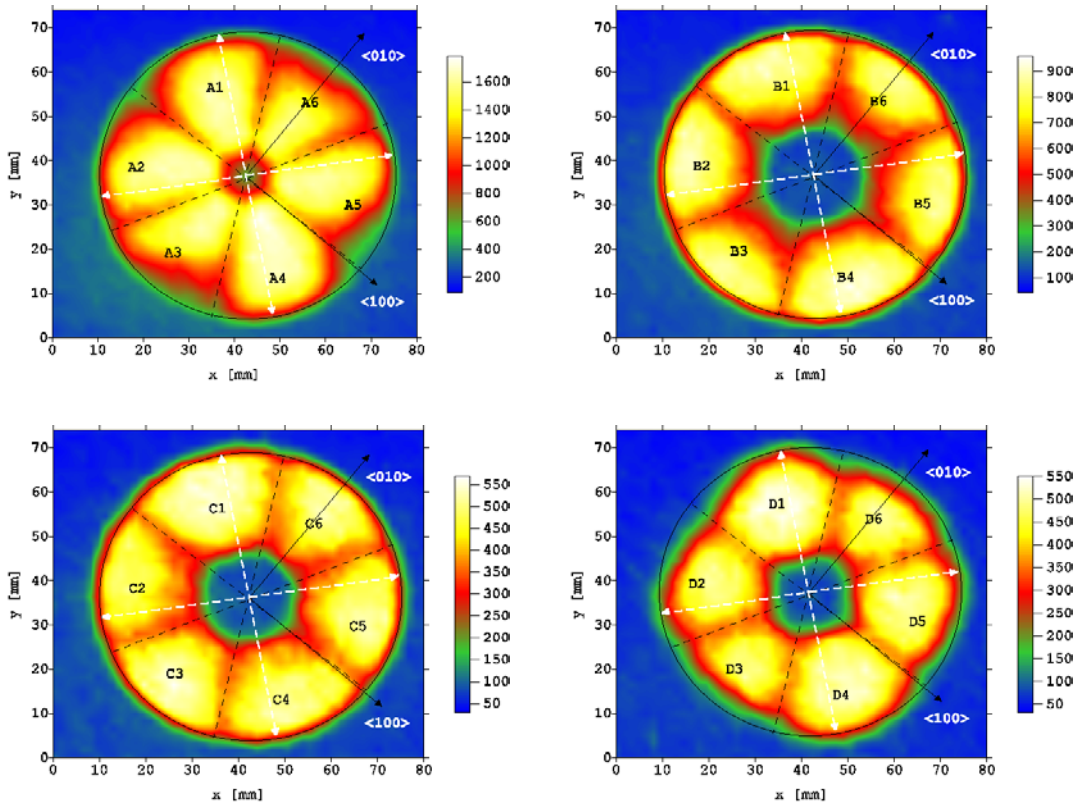


Figure 4.15: Maps of the segment sensitivity for slice A (top left), slice B (top right), slice C (bottom left) and slice D (bottom right). The photopeak events were selected using a wide energy gate both on the centre and on the outer contacts. The white arrows indicate the probable crystallographic directions labelled by the Miller indices.

the same detector slice. As will be discussed in section 5, it is possible to decide whether an interaction has occurred close to the front or close to the back part of a given slice, by looking at the magnitude of the *transient charge signals* (a transient charge is induced in the spectator segment to a $\gamma$-ray interaction) induced in the adjacent slices along the vertical direction. Transient charges are defined as large or small depending on their magnitude. In this work the classification has been made by requiring an amplitude threshold, as shown in Fig. 4.19. The amplitude of the image charge is expressed in arbitrary units, since it has been calculated as the maximum of the transient charge signal, without applying any formal calibration. For example, if an interaction occurs close to the front part of segment A1, the amplitude of the transient charge signal induced in segment B1 is small, on the contrary, if

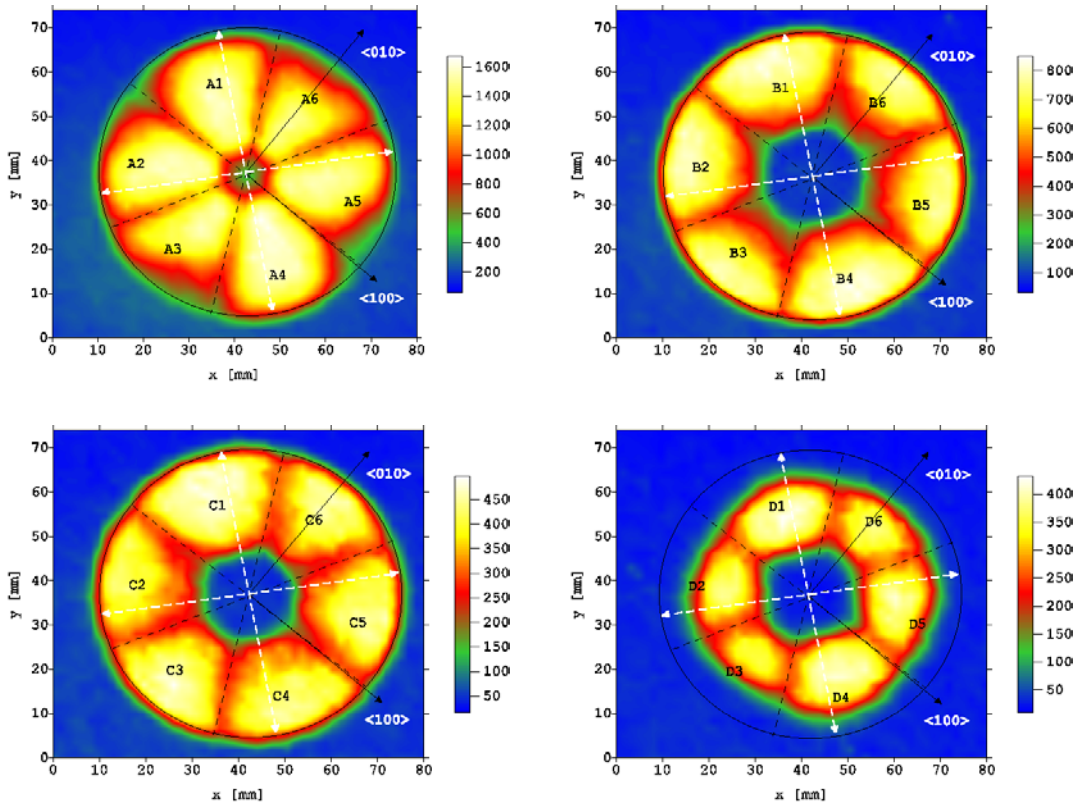


Figure 4.16: Maps of the segment sensitivity for slice A (top left), slice B (top right), slice C (bottom left) and slice D (bottom right). The photopeak events were selected using a wide energy gate on the centre and a narrow energy gate on the outer contacts. The white arrows indicate the probable crystallographic directions labelled by the Miller indices.

the interaction occurs close to the back part of segment A1, the amplitude of the transient charge induced in segment B1 is large. Using this argument, interactions occurring in either the front part or the back part of each detector slice have been selected.

The results for slice A are reported in Fig. 4.20. The top plots show the number of 662 keV $\gamma$ rays fully collected at the back of slice A, for a narrow (left) and wide (right) energy gate applied to the centre contact. The bottom left plot shows the number of photopeak events occurring in the front part of the slice for a wide energy gate (for a narrow gate, the efficiency map looks identical but with less statistics).

In order to understand the results, one needs to consider the trajectories the charge carriers have to travel to reach the destination electrodes (see Fig. 2.13). Interactions occurring in

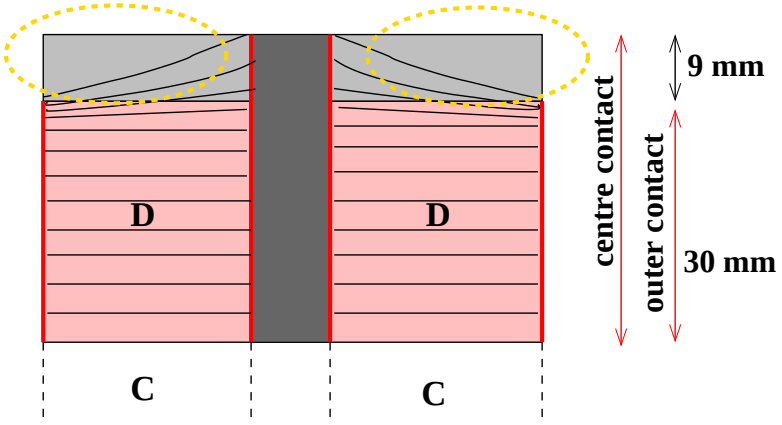


Figure 4.17: Geometry of slice D. For technical reasons, a layer of 9 mm of "dead" germanium is placed at the back of the detector: the centre electrode is 9 mm longer than the sum of the length of the outer electrodes.

the front part of slice A, where the electric field is nearly uniform at the front of the centre electrode and weak at the edge, are mainly collected towards the centre of the detector. Interactions occurring in the back part of slice A, where the electric field is quasi-coaxial, are fully collected with charge carriers moving towards the crystal edge. Crystal orientation effects are enhanced by the narrow gate. It is worth noticing that in the top plots of Fig. 4.20, the number of counts drops at the centre of the crystal because of the lack of information from the transient charge signals. As will be discussed in the next chapter, the part of the segment most sensitive to full energy events corresponds to the middle of the active volume. However this region, due to the small size of the mirror charge induced on the adjacent segments, is the least useful to pulse shape analysis purposes.

Fig. 4.21 shows the Compton scattering sensitivity maps for $\gamma$-ray interactions occurring in the back part (left) and in the front part (right) of slice A. Again, it is evident, the regions most sensitive to Compton scattered events are the segmentation boundaries. Again, the efficiency of the front part is higher at the centre of the detector, the sensitivity of the back part remains high up to the edge. The drop in sensitivity for different radial positions can be attributed to the lack of transient charge information.

Fig. 4.22 and Fig. 4.23 show the photopeak sensitivity at the front and at the back of slices B and C, respectively. Interactions in the front part of slice B were selected by

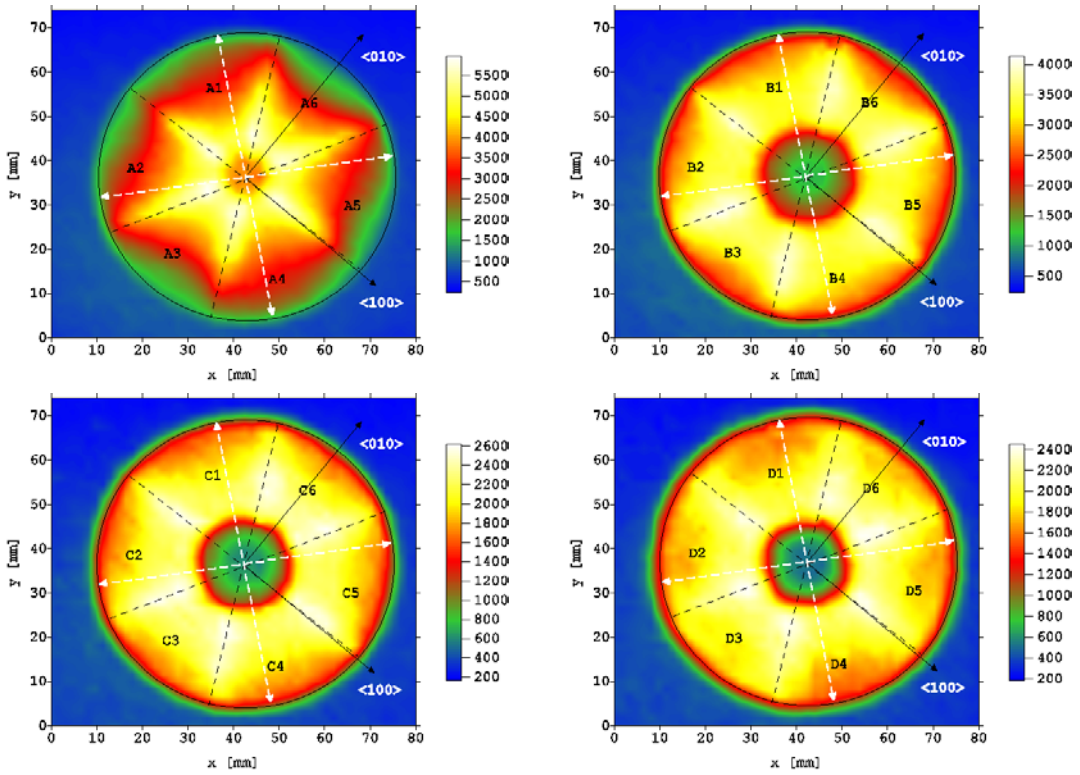


Figure 4.18: Maps of the Compton scattering sensitivity for slice A (top left), slice B (top right), slice C (bottom left) and slice D (bottom right). The number of full-energy events involving an interaction in more than one segment has been plotted as a function of the collimator position. The white arrows indicate the probable crystallographic directions labelled by the Miller indices.

requiring a large transient charge induced in slice A or a small transient charge induced in slice C; interactions in the back part of slice B were selected by requiring a small transient charge induced in slice A or a large transient charge in slice C. Similarly, interactions in the front part of slice C were selected by requiring a large transient charge induced in slice B or a small transient charge induced in slice D; interactions in the back part of slice C were selected by requiring a small transient charge induced in slice B or a large transient charge in the slice D. As expected, since the electric field in slices B and C is truly coaxial, the sensitivity maps displays axial symmetry. The smaller number of counts in the middle of the active volume, in left plots, once again is attributed to the poor transient charge information at this radius. These plots provide a measure of the region where image charge

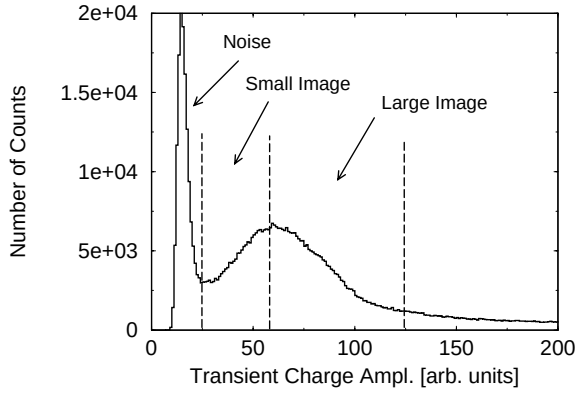


Figure 4.19: Frequency distribution of the amplitude of the transient charge signal measured as the absolute maximum of a typical outer contact signal. The amplitude values are expressed in arbitrary units, because no calibration or gain matching procedures have been applied to the data. The threshold defining an image charge as large or small is indicated.

is not present. The significance of this effect will be discussed in chapter 5.

Finally, Fig. 4.24 shows the sensitivity at the front and at the back of slice D, obtained by selecting, respectively, a large and a small transient charge induced in slice C. The plots show that the sensitivity drops considerably in the outside part of the slice. As already mentioned and as shown in Fig. 4.17, the outer electrode is 9 mm shorter than the inner one, i.e. from the point of view of the outer contacts, there is a 9 mm dead layer of germanium. If the $\gamma$-ray interaction occurs in this layer, the charge is not collected by the outer contact, which therefore do not see the full energy event. The situation is worse at the back than at the front of the slice.

### 4.3.3 Position of the segment boundaries

When the detector was mounted on the scanning table, the relative position of the segments was unknown. In order to determine the position of the segment boundaries, the detector response was investigated and hit-pattern spectra were created as a function of the interaction position. Results at four representative positions of the scanning table within sector three, are shown in Fig. 4.25. A hit-pattern spectrum is defined as the histogram incremented with the number of real events occurring in each of the twenty four segments. From the number of incremented counts, qualitative information about the macroscopic

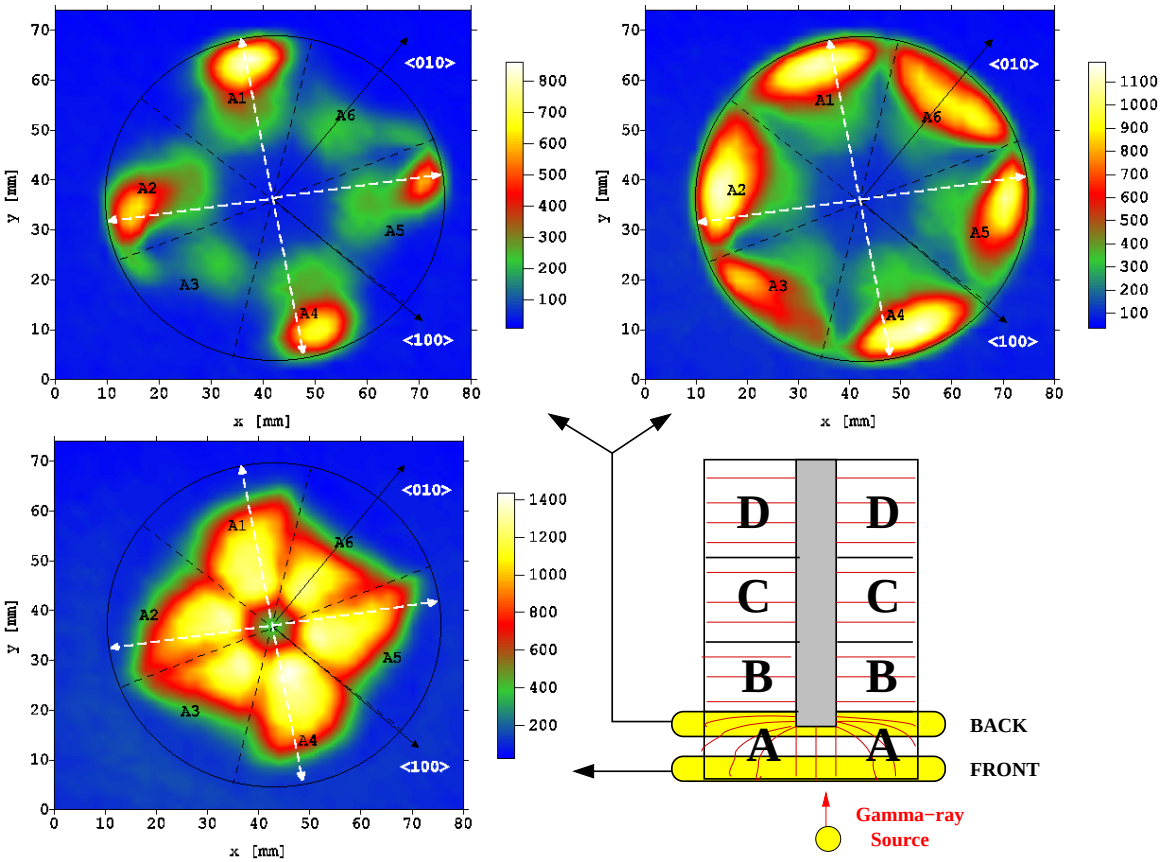


Figure 4.20: Photopeak efficiency map at different depths in slice A. Events occurring at different depths were selected using the amplitude of transient charge signals induced in slice B: a small image charge induced in the B-contact corresponds to an interaction occurring in the front part of slice A, on the contrary, a large image charge corresponds to an interaction occurring in the back part of slice A, close to the boundary with B.

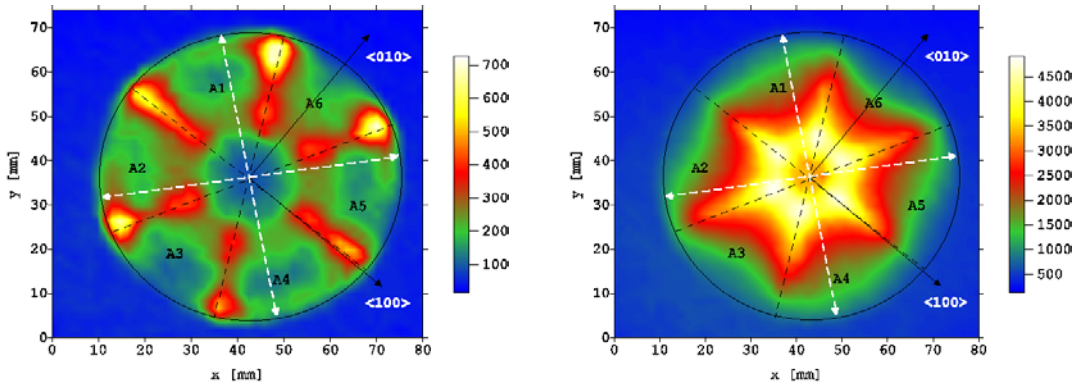


Figure 4.21: Compton scattering efficiency map in the back part (left) and in the front part (right) of the slice A.

position of the $\gamma$-ray source can be obtained. From these results it can be concluded that:

- position (1) corresponds to interaction occurring in front of the centre contact. The core electrode contact absorbs $\gamma$ rays which interact in it. The number of counts in segment A3 is therefore almost unaffected, because the central electrode only extends 0.6 cm inside the front slice (see Fig. 4.2);

- position (2) was determined to be closer to the boundary with sector two, because the number of counts observed in the segments of sector two is higher than in the segments of sector four;

- position (3) is closer to the boundary with sector four;

- position (4) is closer to the boundary with sector four and close to the crystal edge, because the number of counts in slice A is slightly lower than in slice B. This is a direct result of the poor charge collection observed at the edge of the front slice.

Sensitivity maps for each segment were incremented in order to obtain information on the effective position of the segmentation boundaries. Fig. 4.26 shows the sensitivity plots for segments A1, B1, C1 and D1. The results show that the A-segments are well defined and their borders overlap with the segmentation planes, but in the B, C and D-segments the boundaries are smeared out. This smearing is a consequence of the geometry of the collimator: $\gamma$ rays interacting in the front part of the detector are well collimated, while

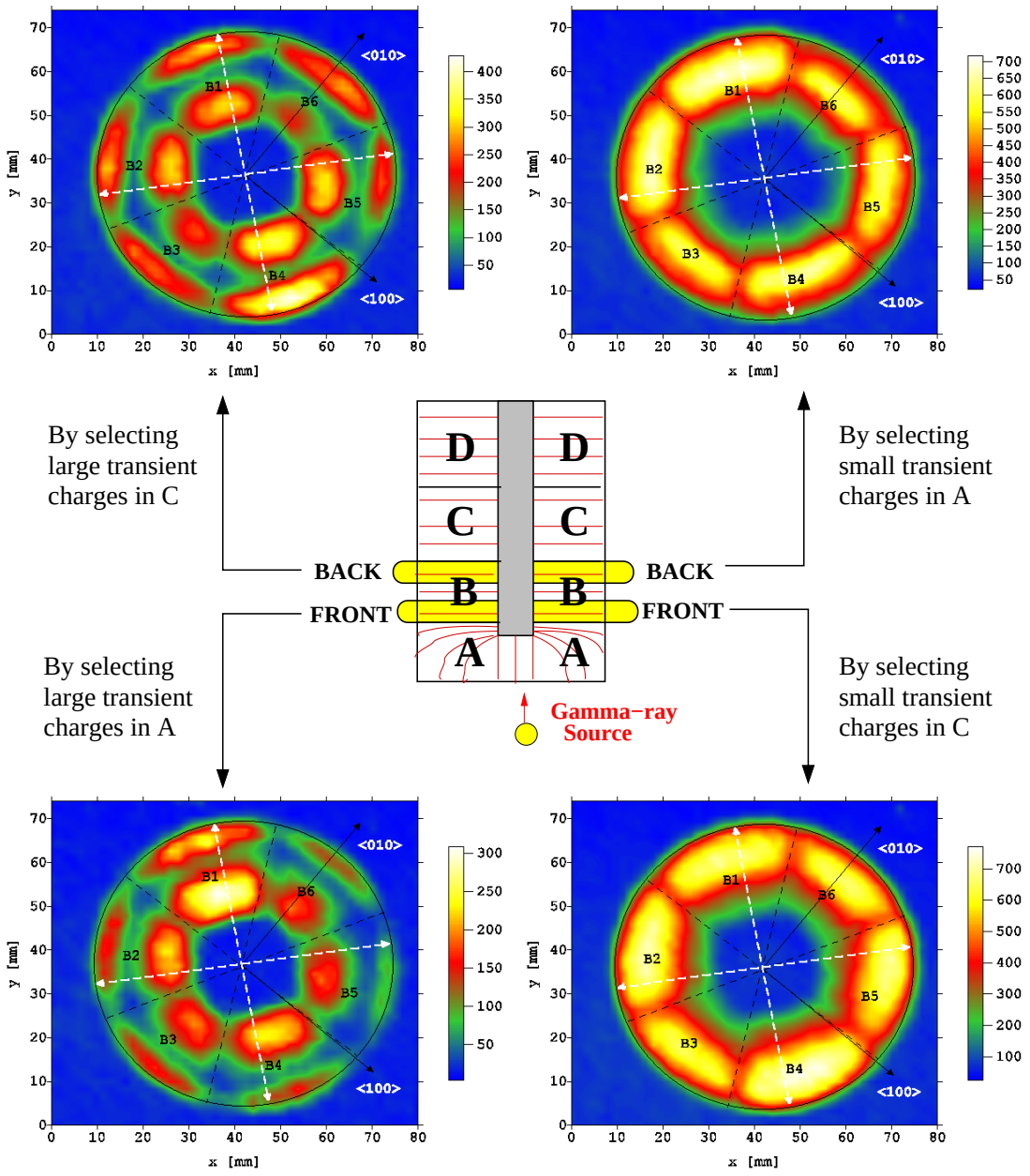


Figure 4.22: Photopeak efficiency map at two depths in slice B: near slice C selecting large image charges in the C-contacts (top left) or small image charges in the A-contacts (top right), and near slice A selecting large image charges in the A-contacts (bottom left) or small image charges in the C-contacts (bottom right).

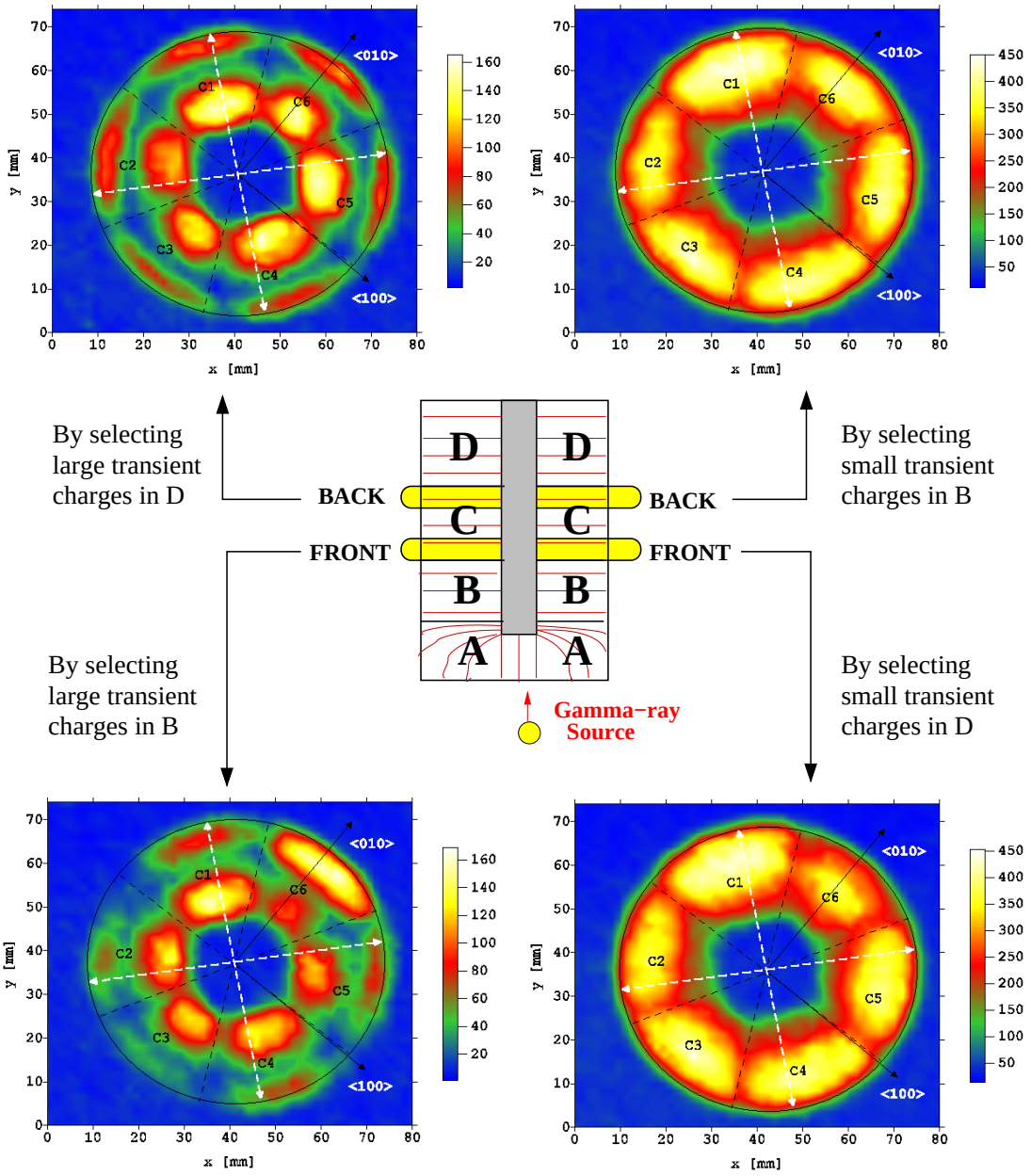


Figure 4.23: Photopeak efficiency map at two depths in slice C: near slice D selecting large image charges in the D-contacts (top left) or small image charges in the B-contacts (top right), and near slice B selecting large image charges in the B-contacts (bottom left) or small image charges in the D-contacts (bottom right).

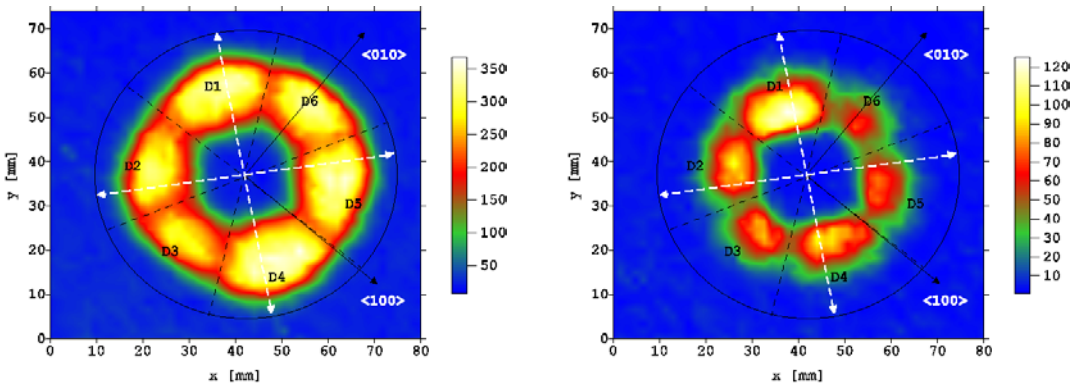


Figure 4.24: Photopeak efficiency map at two depths in slice D: near slice C selecting large image charges in the C-contacts (left) and at the back selecting small image charges in the C-contacts (right).

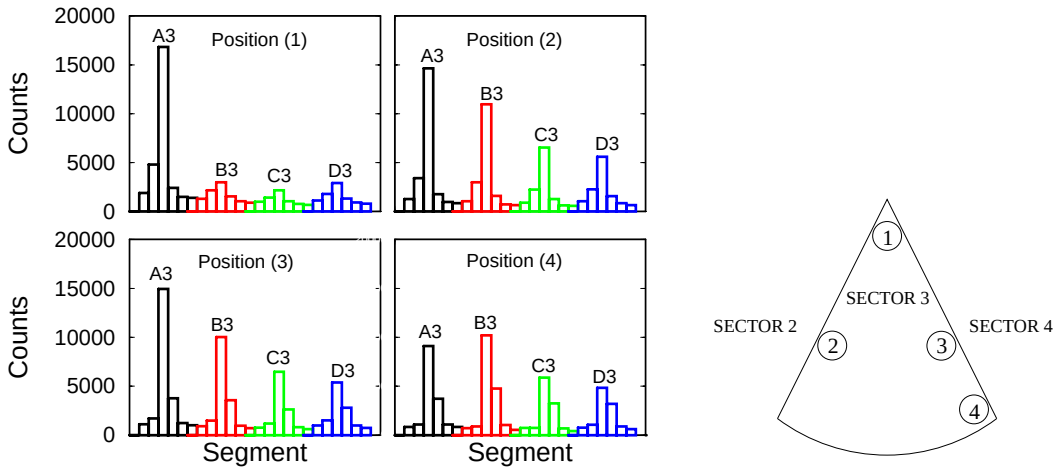


Figure 4.25: Four known positions of the scanning table (right) and the corresponding hit-pattern spectra (left).

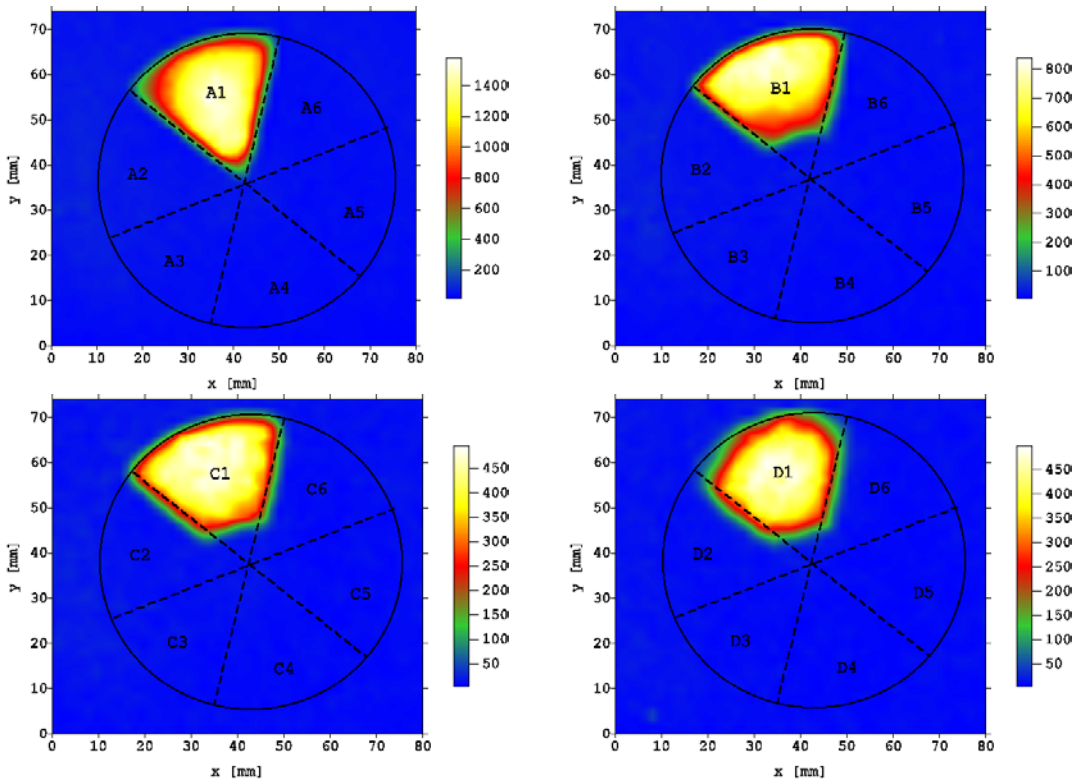


Figure 4.26: Photopeak efficiency map of segment A1 (top left), B1 (top right), C1 (bottom left) and D1 (bottom right). The front part of segment D1 is placed at a distance of 6 cm from the collimator.

those interacting in the back part are spread over a region of ∼5 mm thickness, which agrees with the collimator simulation reported in Fig. 4.5.

In the discussion so far, it has been assumed that the net charge was always collected in the geometrical segment in which the $\gamma$-ray interaction took place. A clarification about the concept of an effective segment in contrast to the geometrical segment has to be made. As explained in [Krö01], the deviation of the drift trajectories from the direction of the electric field lines and the non-radial component of the electric field can be sufficient that the carriers cross the border to the adjacent segment, which then collects the net charge. Although this effect has not yet been quantified, the main point to note is that the contact on which a net charge is measured represents the effective segment.

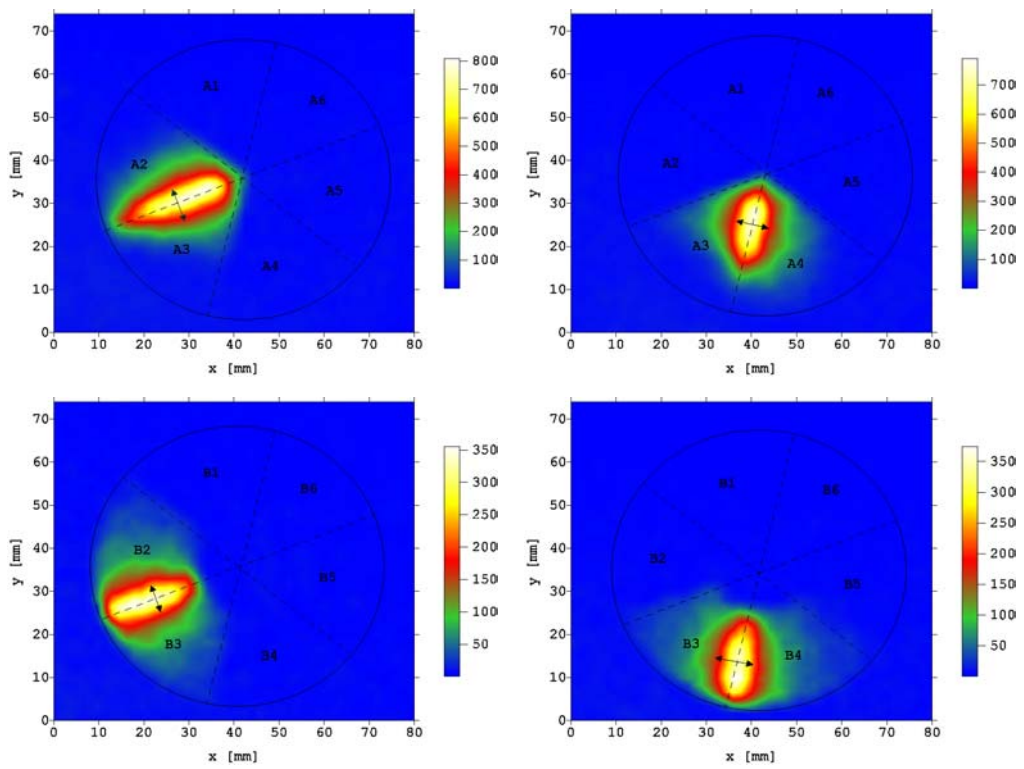


Figure 4.27: Scattering profile for fold-2 events involving segments A2-A3 (top left), A3-A4 (top right), B2-B3 (bottom left), B3-B4 (bottom right).

### 4.3.4 Scattering probability between adjacent segments

In order to investigate on the extent of Compton scattering between adjacent segments and to decide whether, in performing add-back between segments, it is sufficient to include only the nearest neighbour segments (see appendix A), scattering profiles for fold-2 and fold-3 events between adjacent segments were produced. Results are reported in Fig. 4.27 and Fig. 4.28, respectively. These maps enable one to quantify the contribution of Compton events to the total detection efficiency and to visualise the portions of the detector where Compton scattering is the dominant mechanism of interaction. As expected for fold-2 events, the probability of seeing a Compton scattered event between two segments is higher near the segment boundaries. The fact that the probability of seeing a Compton event is more spread out in slice B than in the slice A, can again be attributed to the quality of the collimation.

In the case of fold-3 events, the boundaries in between are the most sensitive parts

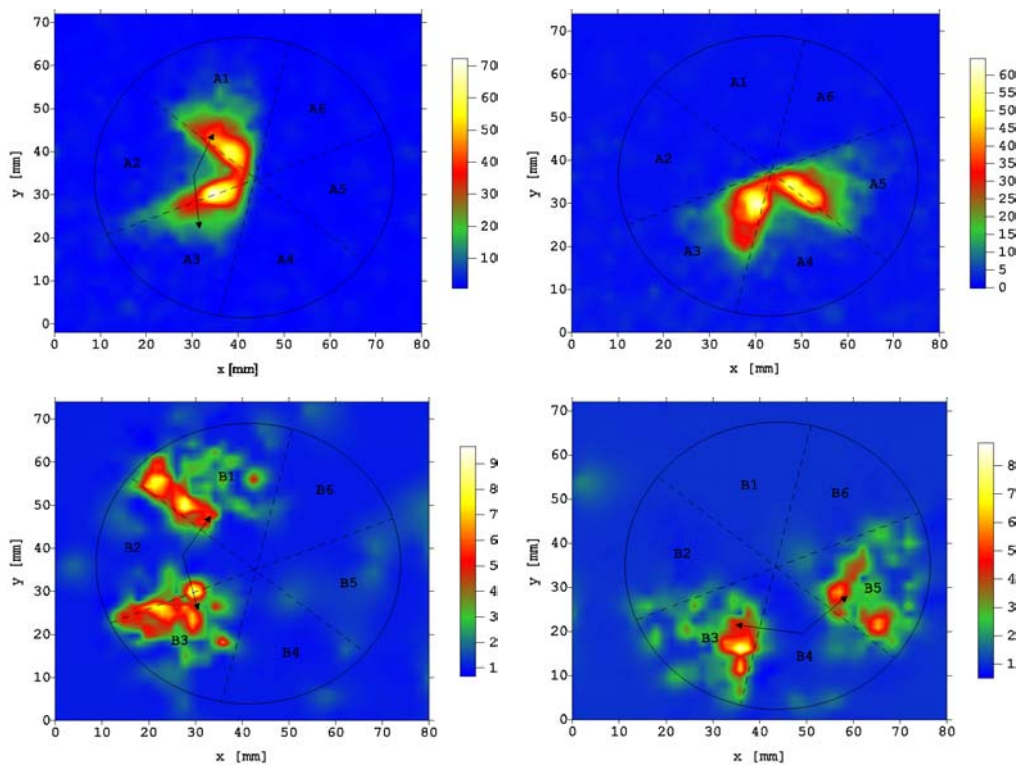


Figure 4.28: Scattering profile for fold-3 events involving segments A1-A2-A3 (top left), A3-A4-A5 (top right), B1-B2-B3 (bottom left), B3-B4-B5 (bottom right).

to Compton scattering. For example, if segments A1, A2 and A3 are considered, the only possible sequences for a scattering event are either A1→A2→A3 or A3→A2→A1. The relative probability of nearest neighbour scattering has been compared by calculating the difference in the number of counts: in the slice A fold-2 events are 10 times more likely than fold-3 events, while in the B-ring the factor is ∼30. In slice A, scattering events indeed take place mostly in the area in front of the centre electrode, where the azimuthal distance between the segment boundaries is smaller.

# Chapter 5

# The concept of pulse shape analysis

Signals from radiation detectors carry information not only in their amplitude but also in their shape. For example, certain scintillator detectors allow different types of radiation to be distinguished by the shape of the emitted pulses [Rot84, Bra91]. *Pulse shape discrimination* (PSD) is the technique which allows this distinction and it is based on a measure of the decay time of each pulse by using conventional analog electronics time circuits.

*Pulse shape analysis* (PSA) is a new technique, which utilises digital signal processing to analyse the shape of the pulse produced by a radiation detector. In the context of this work, a number of parameters can be extracted allowing information on the energy, the time and the position of the interaction to be achieved. The use of digital pulse processing allows an improvement on the position resolution of the detector and a consequent enhancement of its *effective granularity*. In this work, the effective granularity of a detector is defined as the number of partitions the detector can be subdivided into; the effective granularity of a segmented detector is given by the number of segments times the number of unique positions which can be distinguished within the same segment.

In the framework of the $\gamma$-ray tracking project, the ultimate goal of pulse shape analysis is to extract the parameters to use as input to the tracking algorithms (see section 3.3).

This chapter discusses the pulse shape analysis method: the theoretical relationship between signal shape and interaction position, the intrinsic limitations and the algorithm developed to extract the desired information will be described. Finally, PSA results obtained from the detector scan will be presented and the effective granularity of the TIGRE detector

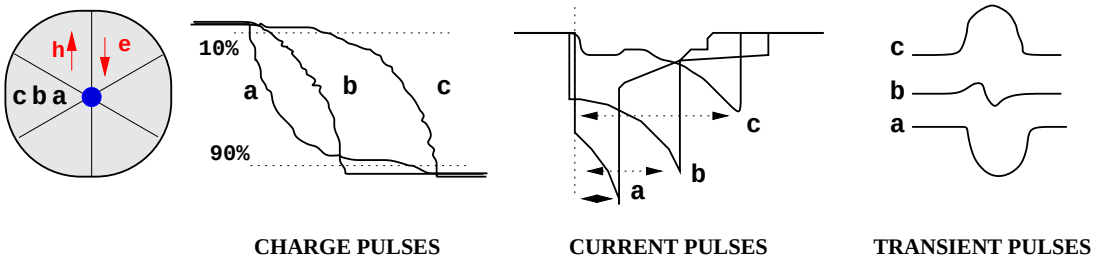


Figure 5.1: A schematic illustration of the leading edge of the centre contact preamplifier signal for three different interaction positions and the corresponding transient charge signals induced in the spectator segment.

will be calculated.

## 5.1 Basic principle

The concept of pulse shape analysis arises from the observation that the shape of the preamplifier signal depends on the position of the interaction [Str72, Pal97]. The main aim of this work is to calibrate the response function of the detector pulse shapes as a function of the position. A detailed understanding of the relationship between signal shape and interaction position is fundamental for developing pulse shape analysis algorithms.

The fundamental concept of *real event signal* and *transient event signal* will be explained. In Fig. 5.1, a schematic illustration of the leading edge of the centre contact preamplifier signal for three different interaction positions in the coaxial part of the detector is illustrated: both charge and current signals are sketched. For each position, the corresponding transient charge signal induced in a spectator segment is also shown.

1. In a segmented detector, the signal corresponding to a real event is measured on the segment where the $\gamma$-ray interaction takes place. In the following, the shape of the signal measured form the centre contact will be discussed. It can be analysed in terms of a charge signal or current signal.

   **Charge signal**: corresponds to the growth of the time dependent charge induced

at the electrodes, while the secondary charge carriers (electrons and holes) are being collected. Since the path of electrons and holes is different, different signal shapes correspond to interactions occurring at different distances from the electrodes. Therefore, real charge signals carry radial position information. If the $\gamma$-ray interaction occurs near the outer or near the inner contact, the pulse rises slowly, because either the electrons or the holes have to travel a longer distance. Although both pulses have long rise time, their shape is completely different, i.e. convex and concave, respectively. This difference allows us to distinguish between the two radial positions. When the interaction occurs in the middle of the active volume, the signal rises faster, because both charge clouds have to travel the same, and therefore the shortest, distance. The resulting rise time distribution is hence symmetrical with respect to the middle of the active volume. To be precise, the minimum rise time occurs at the radial position for which the collection time of electrons, $t_e$, is equal to the collection time of the holes, $t_h$. Due to the slightly different saturation velocity of electrons and holes (along the $\langle 111 \rangle$ direction the saturation velocity is $1.0 \times 10^7$ cm/s for electrons and $0.9 \times 10^7$ cm/s for holes), the radial position which satisfies this condition is not exactly the middle of the active volume.

If the geometry of the TIGRE detector (see Fig. 4.2) is considered, the distance between the inner and the outer electrode, $l$, is 28.5 mm (32.5 mm the radius of the germanium crystal minus 4 mm radius of the centre contact). By using the simple relations:

$$s_e + s_h = l \qquad s_{e,h} = v_{e,h} t, \tag{5.1}$$

where $s_{e,h}$ and $v_{e,h}$ are the path and the saturation velocity of electrons and holes, respectively, one obtains $s_e$=15 mm and $s_h$=13.5 mm.

**Current signal**: corresponds to the current flowing into the electrode to keep the potential constant. Because the detector preamplifiers are charge sensitive, current signals are experimentally obtained as the time derivative of the charge signals. The current signal presents different collection time and different amplitude at the time of collection as a function of the radial interaction position. Like the charge, the current pulse starts growing when the secondary charge carriers are created by the photoelectron, but differs from the charge pulse in that the current signal stops rising when

the electrons are collected at the centre contact, whether or not holes have also been collected by the outer. The time-to-maximum of the current pulse, i.e. the collection time of the electrons, is short for interactions close to the inner contact and large for interactions close to the outer contact. The maximum amplitude carries information on the interaction position, because it depends on the magnitude of the weighting potential, which the charge carriers have to traverse (see section 2.6). Current signals, as well as charge signals, carry radial position information.

2. The signal corresponding to a transient event is induced in the segments adjacent to the one hit by the $\gamma$ ray and does not contain a net charge deposition. It is systematically smaller than the corresponding real charge signal, typically less then 40%. A transient charge signal carries two kinds of position information:

   - Azimuthal position information from a measure of the signal amplitude. Consider the two segments adjacent to the one hit by the $\gamma$ ray. The amplitude of the transient charge signal induced in the segment closer to the interaction is larger. Due to the cylindrical geometry of the TIGRE detector, this gives information on the angular position of the interaction.
   - Radial position information from a measure of the signal polarity. The different polarity of electrons and holes results in a transient signal corresponding to an interaction close to the outside having a positive polarity (electrons dominate the charge collection process) and a transient signals corresponding to an interaction close to the inside having a negative polarity (holes dominate the charge collection process).

For the outer contact signal, the same concepts apply. However, holes and not electrons are collected at the outer electrode, this means that the shape of the outer contact signal will be identical to that of inner contact, but symmetrically reflected.

In the closed-ended part of the detector, the response function is more complicated, due to the complex electric field observed in the previous chapter. It is therefore more difficult to find a direct relationship between the shape of the pulse and the position of the interaction. A quantitative understanding of the behaviour of the pulse shape in the closed-ended part of the detector is beyond the scope of this work.

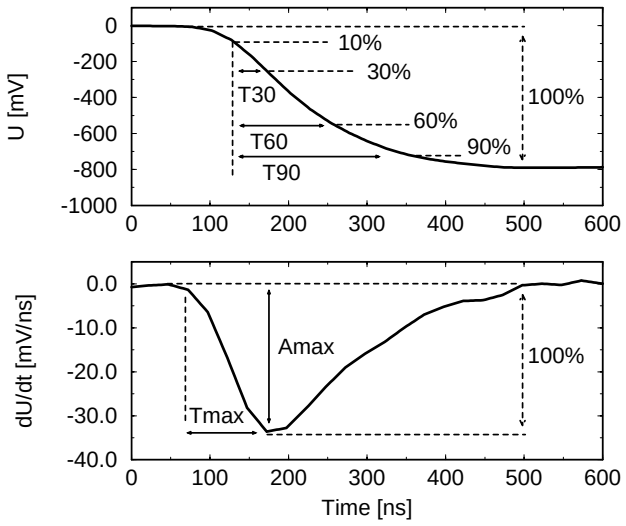


Figure 5.2: The charge (top) and current (bottom) preamplifier signals with the parameters used in the analysis.

## 5.2 The method

In order to extract position information from the pulse shape it is necessary to calibrate the pulse shape response as a function of the interaction position. A rigorous theoretical treatment based on traditional methods, such as developed in orthonormal bases or in Fourier series [Pas96], though mathematically correct, is unrealistic, due to the complexity of the problem. A semi-empirical formalism must be attempted.

In this work, the radial position of the interaction has been obtained by measuring the collection time of the charge carriers in conjunction with the polarity of the induced transient signals. The azimuthal position has been calculated by measuring the asymmetry in the amplitude of the transient signals induced on the neighbouring segments. The asymmetry in the amplitude of the two transient signals induced in the adjacent segments along the z-direction, provides information regarding the depth of the interaction. A number of different approaches for extracting the rise time from the digitized signals have been attempted. The parameters considered in this analysis are (see Fig. 5.2):

- the rise time of the charge signal (T90, T60, T30),

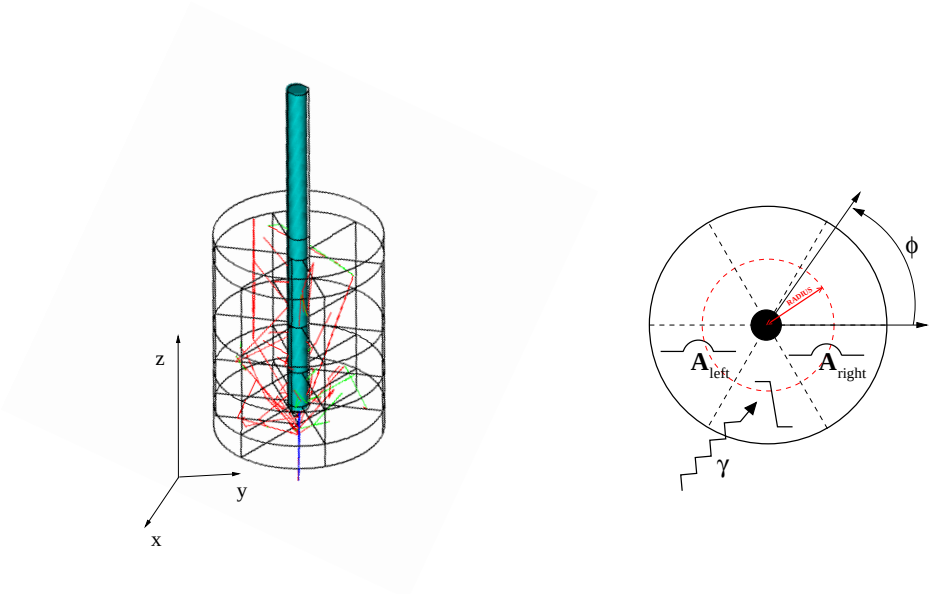


Figure 5.3: A simulation of the scattering path of the $\gamma$ ray in the detector volume, produced with the MCNP code [Mcn94] (left). A schematic front view of the detector, the segment hit by the $\gamma$ ray and the transient charge signal induced in two adjacent segments, called *left* and *right*, are indicated (right).

- the time to maximum of the current signal ($T_{max}$),

The pulse rise time is defined as the time the pulse takes to rise from 10% to 90% of its final amplitude, and is therefore called T90. In order to take into account the whole shape of the signal and therefore resolve ambiguities between the two symmetrical positions with respect to the intermediate radius, T30 and T60 (i.e. the time the pulse takes to rise from 10% to either 30% or 60% of its final amplitude) times are also measured.

The time-to-maximum of the current pulse is defined as the time interval between the start of the pulse and the instant at which the pulse reaches its maximum amplitude.

The asymmetry in the amplitude of transient signal is defined as:

$$Asym = A_{left} - A_{right} \tag{5.2}$$

where $A_{left,right}$ is the magnitude of the transient charge induced in the specified adjacent segment (see Fig. 5.3). The magnitude of the transient charge was measured by considering the point of maximum amplitude and by summing the amplitudes of three data points at each side of the maximum. In order to extract information on the depth of the interaction,

the asymmetry between the image charge induced in the vertical adjacent segment will be calculated.

### 5.2.1 Example pulse shapes

Representative pulse shapes showing the typical response function of the detector as a function of the interaction position will be presented in this section.

Fig. 5.4 shows preamplifier output signals for three known interaction positions. In each case the real charge signals from a fold-1 interaction in segment B3 and the transient charge signals from the nine adjacent segments are shown. A visual inspection of the charge pulse does not allow an obvious conclusion to be drawn; more meaningful information comes from the transient signals. If the interaction occurs near the inner contact and close to sector two (i.e. in the position labelled (1)), the transient signals have negative polarity, being mainly induced by the motion of the holes towards the outer electrode, and the amplitude of the image charge induced in segment B2 is larger than the one induced in segment B4. On the contrary, if the interaction occurs close to the outer electrode (i.e. in the positions labelled (2) and (3)), the polarity of the transient signals is positive, since it is due to the motion of the electrons towards the inner contact. In position (2), close to the centre of the segment, the amplitude of the transient charge induced in segment B2 and B3 is equally small, while in position (3), close to sector four, the amplitude of the image charge in segment B4 is larger than the one in segment B2. The transient signals induced in the neighbouring segments along the emission direction of the $\gamma$ ray, i.e. segments A3 and C3, show a large spread in the magnitude of the transient signals. This is a consequence of the uncertainty in the z-position of the interaction.
As a comparison, the current signals obtained as a time derivative of the charge signals are displayed in Fig. 5.5 for position (1).

## 5.3 The algorithm

The developed pulse shape analysis algorithm is discussed here. The algorithm is suitable for an on/off-line analysis of the preamplifier data, digitized both at 40 MHz (i.e. one data point every 25 ns) and at 100 MHz (i.e. one data point every 10 ns).

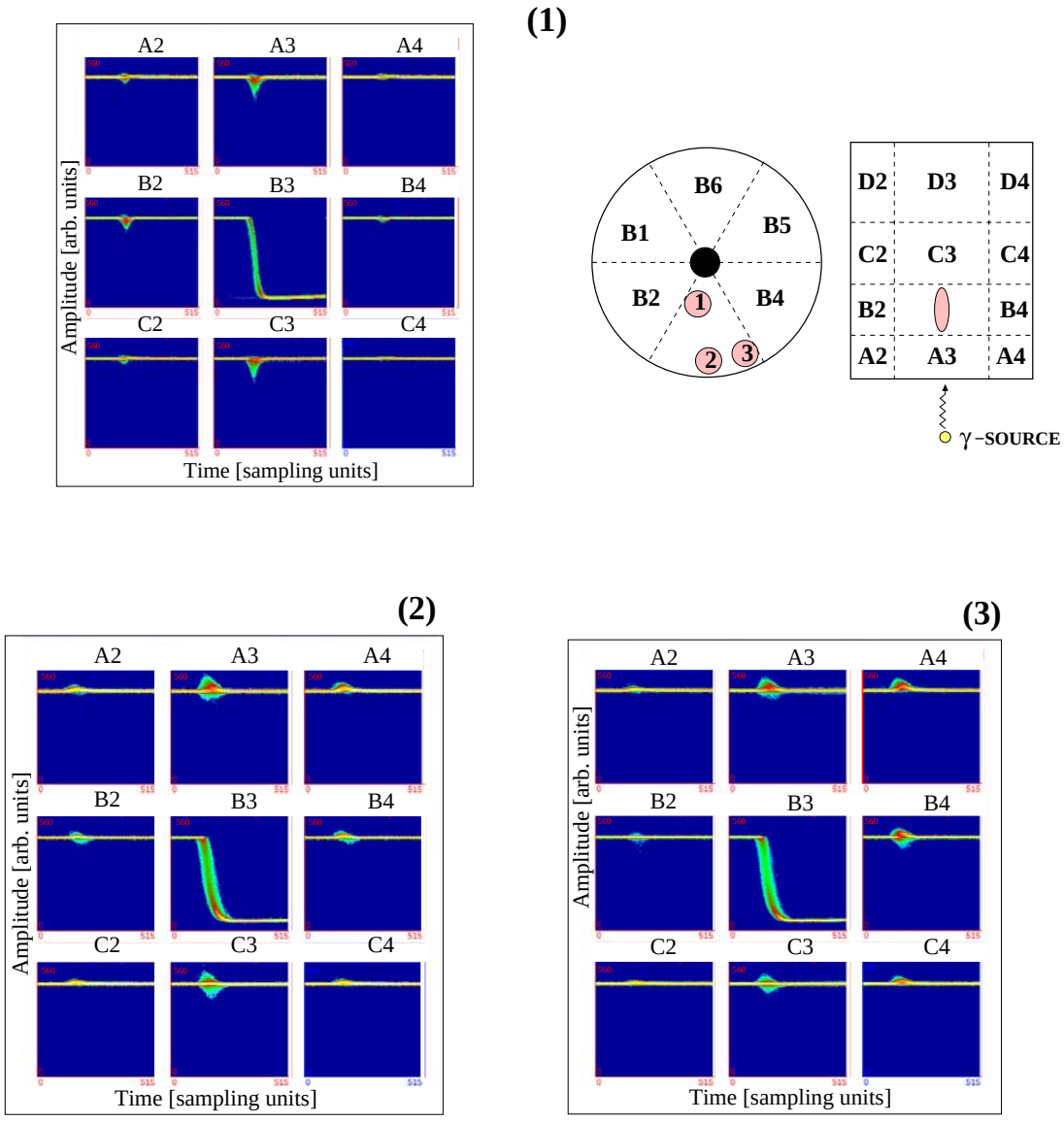


Figure 5.4: Examples of charge signals corresponding to the three different interaction positions. The figure number (1), (2) and (3) corresponds to positions (1), (2) and (3), respectively. For each interaction position, the real charge signal from contact B3, corresponding to a fully absorbed $\gamma$ ray, and the respective transient charge signal induced on the nine adjacent segments, are shown. The preamplifier pulses are displayed as digitized by the FADCs, the sampling unit corresponds to 25 ns. A typical amplitude of a 662 keV $\gamma$ ray is 800 mV.

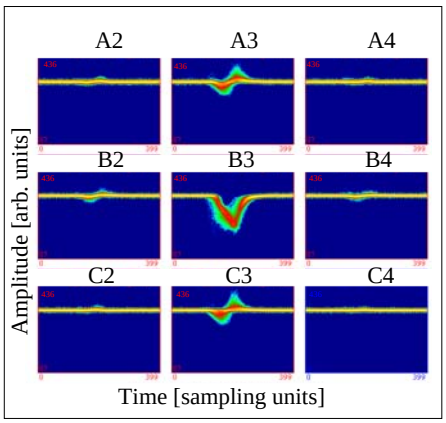


Figure 5.5: Example of current signals obtained as time derivatives of the charge signals for position (1) shown in Fig. 5.4.

Depending on the type of signal (net charge, transient charge or noise) and on the kind of information to be extracted (radial position, angular position or energy), the pulse shapes are allocated to different processing steps, as shown in the flow chart of Fig. 5.6.

The noise level of each incoming raw pulse shape is calculated as the standard deviation, $\sigma$, of the baseline fluctuations over a time window of 400 ns. This value provides an event-by-event threshold, which is used to distinguish between signals carrying real information and signals containing only noise oscillations. If the amplitude difference between the start and the end of the pulse, which is proportional to the charge created by the $\gamma$-ray interaction, is $\geq 3\sigma$, the signal is considered as a real charge pulse. Otherwise, in order to distinguish between noise and transient charge, the signal components are summed over a time window of 300 ns starting from the trigger point. If the integrated charge is $\geq 3\sigma$ the signal is considered as a transient charge pulse, otherwise it is considered as noise and rejected.

From analysis of the histogram data, the threshold value of $3\sigma$ also agrees with the noise calculation presented in section 4.2.4, being on average about 9 keV, i.e. twice the total integrated power. This value is also consistent with the peak-to-peak noise of $\sim$10 keV, measured from the pulse shape after amplification (the peak-to-peak noise measured from the preamplifier signal before amplification was 2.5 mV).

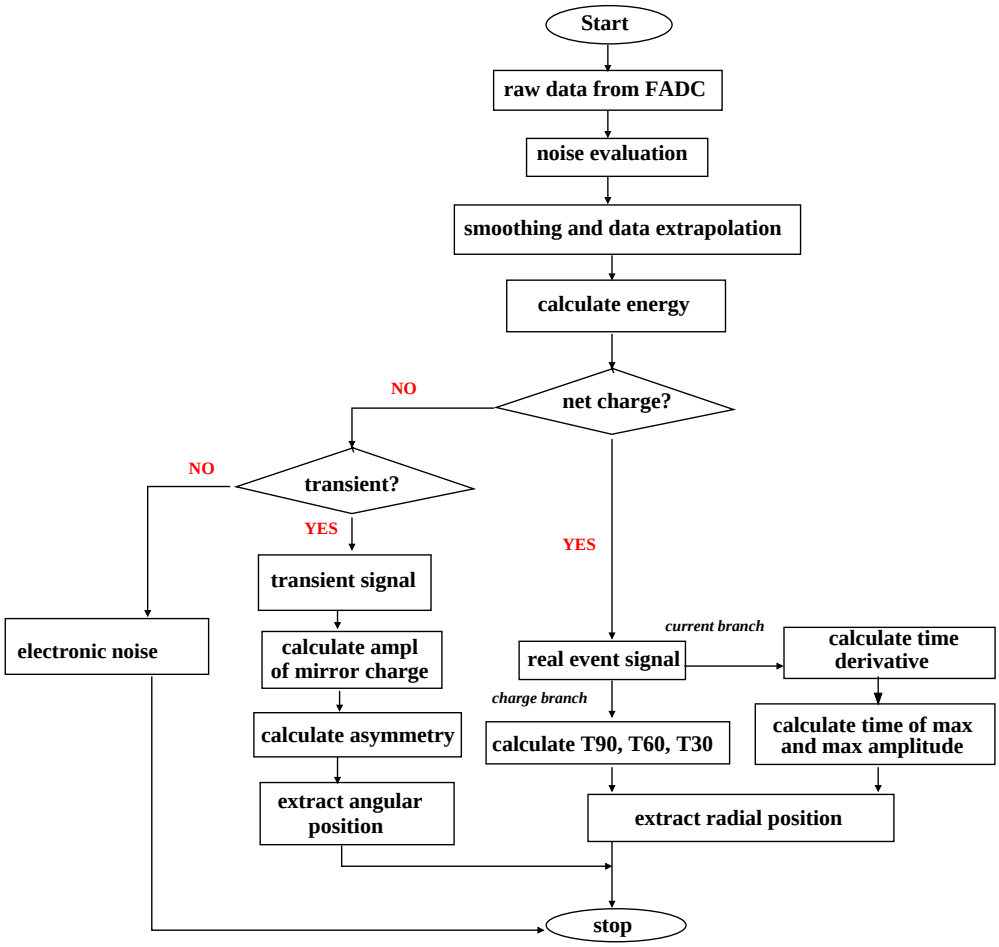


Figure 5.6: Flow chart of the pulse shape analysis algorithms.

From the real charge signal, T90, T60 and T30 times are calculated, the corresponding current pulse is obtained and the time-of-maximum is extracted. The values will provide a calibration for the radial dependence of the interaction position. The transient charge signal from the contacts adjacent to the one that fired, are then analysed to extract angular position information.

### 5.3.1 Pulse processing routine

The pulse shapes are filtered in order to minimise high frequency noise components and macroscopic fluctuations, induced by the digitization step, which are super-imposed on the

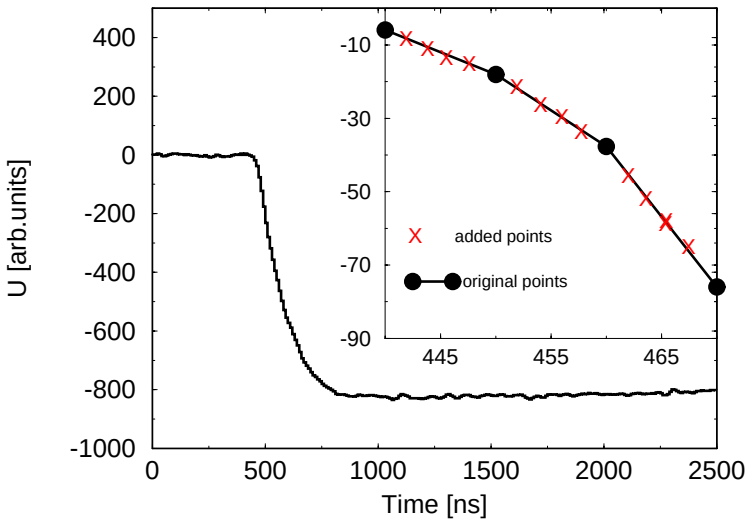


Figure 5.7: Example of a pulse shape digitized at 100 MHz. The effect of the data points interpolation is shown.

signal.

Filtering is a very important step in the pulse processing chain. The high frequency noise components are minimised by a *smoothing routine* based on a running average over three data points:

$$u(i) = \frac{1}{4}u(i-1) + \frac{1}{2}u(i) + \frac{1}{4}u(i+1), \tag{5.3}$$

where $u(i)$ is the amplitude of the signal at the time $i$. In order to facilitate a more precise extraction of the information and to overcome the limitations imposed by the finite sampling frequency of the FADCs (either 25 ns or 10 ns), the data are interpolated by means of a straight line fit. The line between each pair of data points is calculated and four interpolated data points are added in between every pair of original data points (see Fig. 5.7). Following this interpolation, the sampling interval is 5 ns (instead then 25 ns) for the 40 MHz card and 2 ns (instead than 10 ns) for the 100 MHz card. A running average with three data points is performed after the interpolation. This routine has the advantage (over a least squares or polynomial fitting algorithm) of being fast and easy to control.

For more information on digital filtering techniques such as the *wavelet transformations*, the reader is referred to [Mih00b].

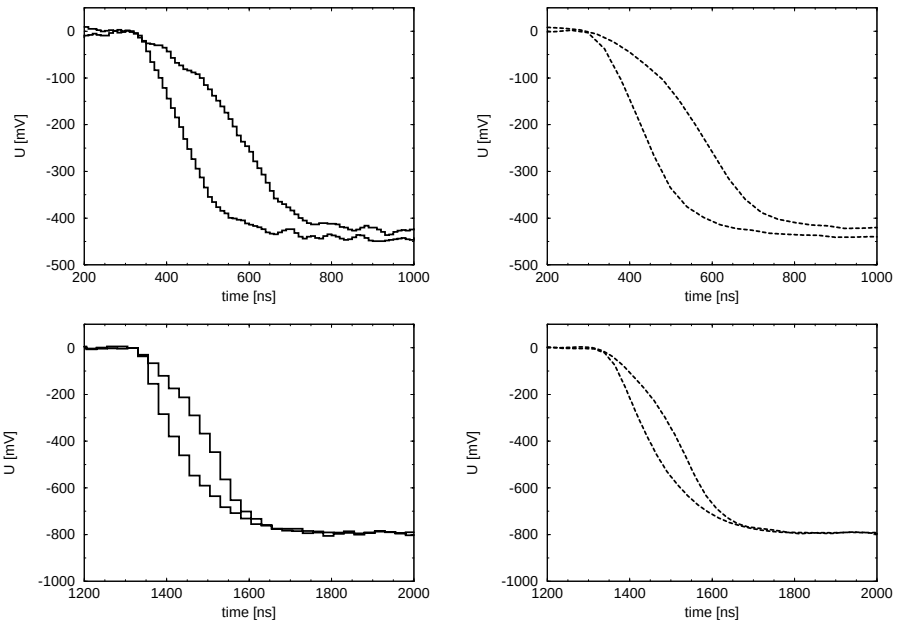


Figure 5.8: Pulses from the centre contact digitized with the 100 MHz card (one sample every 10 ns) and from an typical outer segment digitized with the 40 MHz card (one sample every 25 ns) are presented in the top left and bottom left part, respectively. The same pulses after smoothing have a sampling interval of 2 ns and 5 ns, respectively; they are presented in the top right and bottom right part.

### The Moving Window Deconvolution method

Following signal filtering, the energy is extracted from the amplitude of the preamplifier signal. A well-established method to obtain good energy resolution is the Moving Window Deconvolution (MWD) algorithm [Geo93].

The Moving Window Deconvolution method is based on a deconvolution step, which enables the reconstruction of the original charge distribution function, $g(t)$, from the detector output signal $U_p(t)$. It is known that the signal output from a semiconductor detector is described by a convolution integral between the charge distribution function $g(t)$and the preamplifier response $f(t)$:

$$U_p(t) = \int_{-\infty}^{+\infty} g(\tau) f(t-\tau), \tag{5.4}$$

where $\tau$ is an arbitrary time of reference. In the case of a digitized pulse shape, its discrete-

time representation is given by a convolution sum, one for each sampled point:

$$U_p(i) = \sum_{j=0}^{\infty} g(j) f(i-j), \tag{5.5}$$

where the sampling interval has been normalized to unity. To get the original charge distribution function, one should solve, for each value $i$, Eq. 5.5 with respect to $g(j)$. In fact, this problem can be solved by applying some simplification. First, the preamplifier response function is time-invariant and causal, i.e. it depends only on the present and past value of the input charge. The sum in Eq. 5.5 becomes right-side limited:

$$U_p(i) = \sum_{j=z}^{i} g(j) f(i-j); \quad for\ i \geq z \tag{5.6}$$

where $z$ is an arbitrary time reference. A second simplification arises considering that the charge function is time limited. The number of significant equations in (5.6) is therefore finite and equal to the normalized length of the observation interval, $M$. By describing the response function of resistive feedback preamplifier as delta function followed by an exponential decay, with decay constant equal to $\omega_c$:

$$f(i) = e^{-\omega_c i}, \tag{5.7}$$

the set of equations (5.6) can be solved with respect to $g(i)$. Then the total charge released in a time window of length $n$, $G(n)$, is given by:

$$G(n) = \sum_{i=z}^{z+M} g(i) = \sum_{i=n-M}^{n} g(i); \quad for\ n = z + M. \tag{5.8}$$

Since $z$ is an arbitrary time reference, a continuous sequence of $G(n)$ values can be calculated by shifting each window by one sampling interval. Considering that each shifted window has in common M-1 points, only the last equation in the new set (5.6) has to be solved and a recursive approach can be exploited to obtain the deconvoluted charge function. After further simplifications, the total charge deposited by the $\gamma$ ray in the first window and in any window shifted by one sampling interval, is calculated, respectively, as:

$$G(i) = \sum_{j=z}^{i} g(j) = U(i) + (1-k) \sum_{j=z}^{i-1} U(j); \quad for\ i \in (z, z+M) \tag{5.9}$$

$$G(n) = \sum_{j=n-M}^{n} g(j) = U(n) - U(n-M-1) + (1-k) \sum_{j=n-M-1}^{n-1} U(j); \quad for\ any\ n > z+M \tag{5.10}$$

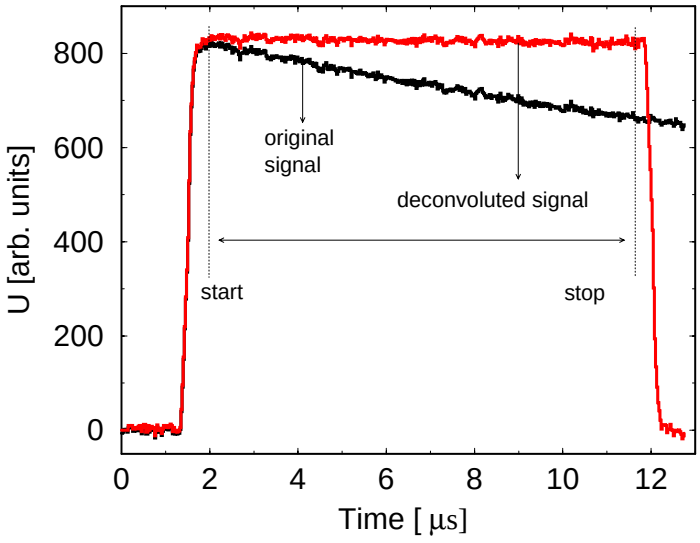


Figure 5.9: The original charge signal measured from a typical outer contact preamplifier (at 40 MHz) and the charge signal obtained following the application of the MWD routine. The MWD works almost as a trapezoidal filter; the total charge deposited by the $\gamma$-ray interaction is calculated as the average value between the start and the end of the flat top of the deconvolved pulse. In this example, a window of 420 data points (corresponding to a time window of 10.5 $\mu$s) has been used in the deconvolution step.

being $k = e^{-\omega_c}$.

An example of a signal shape before and after the deconvolution step, is presented in Fig. 5.9. From the deconvolved signal, the energy is simply calculated as the average flat top value, this results in a true ballistic measure of the energy information. Results from this approach are presented in section 5.5.

### The parabolic fit method

An alternative method used to obtain energy information has been developed, the parabolic fit method [Hert00]. The charge pulse is fitted to a parabolic function which then provides the current, whose integral is proportional to the deposited energy. The algorithm is based on a least squares minimisation method, that returns, for every group of sample points, the slope of the parabola that best fits the data. Given the series of data points ($x_i$, $y_i$), where $x_i$ represents the time and $y_i$ the charge value of the $i^{th}$ sampled point, the parabola

$y = ax^2 + bx + c$, that minimises the $\chi^2$:

$$S = \sum_{i=n-m}^{i=n+m} \left( ax_i^2 + bx_i + c - y_i \right)^2 \tag{5.11}$$

i.e. the parameters that satisfy the relations:

$$\frac{dS}{da} = 0, \ \frac{dS}{db} = 0, \ \frac{dS}{dc} = 0, \tag{5.12}$$

are calculated. In the above expression $n$ is the index of the data point under analysis and $2m$ is the length of the fitting interval. It follows that:

$$a \sum_{k=-m}^{k=m} (k\Delta x)^4 + b \sum_{k=-m}^{k=m} (k\Delta x)^3 + c \sum_{k=-m}^{k=m} (k\Delta x)^2 = \sum_{k=-m}^{k=m} y_k \, (k\Delta x)^2 \tag{5.13}$$

$$a \sum_{k=-m}^{k=m} (k\Delta x)^3 + b \sum_{k=-m}^{k=m} (k\Delta x)^2 + c \sum_{k=-m}^{k=m} (k\Delta x) = \sum_{k=-m}^{k=m} y_k \, (k\Delta x) \tag{5.14}$$

$$a \sum_{k=-m}^{k=m} (k\Delta x)^2 + b \sum_{k=-m}^{k=m} (k\Delta x) + c \sum_{k=-m}^{k=m} 1 = \sum_{k=-m}^{k=m} y_k, \tag{5.15}$$

where $k = i - n$ and $\Delta x$ is the sampling period[1]. This task would require a massive amount of calculation, but some considerations enable us to simplify the process. Firstly, the odd terms in the sum vanish. Secondly, since differentiated pulse shapes have to be obtained, the only coefficient of interest is the b coefficient. Practically, being interested only in the slope of the parabola, which is proportional to the current, the only equation needed to be solve is Eq. 5.14, which becomes:

$$b = \frac{\sum y_i \, (k\Delta x)}{\sum (k\Delta x)^2}. \tag{5.16}$$

The process is repeated for each data point along the pulse shape and the resulting b coefficients are stored in a new array. Examples of the original charge signals and the current signals calculated using this method are presented in Fig. 5.10 for a $^{137}$Cs $\gamma$-ray event in an outer segment. In the left part, the pulse shape has been fitted to a parabolic function using three data points, in the right part the data points used in the parabola were twenty seven. Energy resolution results from this approach are presented in section 5.5.

[1]Because the sampling period is constant, the time value can be written as $x_i = x_0 + i\Delta x$ and the time reference $x_0$ can be considered zero.

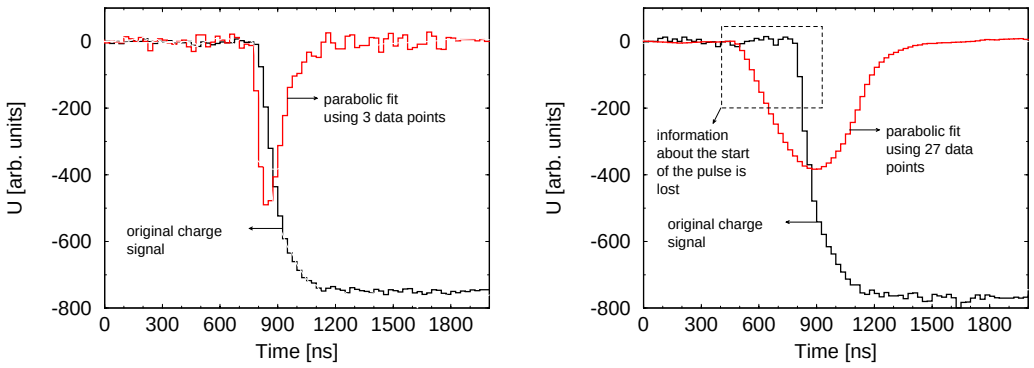


Figure 5.10: Example of current signal calculated utilising the parabolic fit method. The parabolic function was calculated using three (left) and twenty seven (right) data points in the fit.

### 5.3.2 Current signals for position determination

The extraction of the current signal from the charge signal can be used for position determination. In this section two methods will be presented to extract the time dependence of the current pulse shape.

As discussed in section 5.5, utilising the parabolic fit method, in order to smooth the microscopic noise oscillations in the pulse shape and to improve the achievable energy resolution, the number of data points which needed to be fitted to the parabola is large, namely 27 points. From the examples presented in Fig. 5.10, it becomes clear how the use of many data points has the drawback of smoothing the information contained in the beginning of the signal leading edge, which is vital for position determination. For this reason a maximum of 3 data points can be used in the fit, in order to preserve the features of the signal leading edge. Beside the parabolic fit method, the current pulse can be obtained as a first order **time derivative** of the charge pulse:

$$i(j) = \frac{q(j) - q(j-1)}{t(j) - t(j-1)}. \tag{5.17}$$

A comparison of the signal obtained using these two methods is presented in Fig. 5.11. The the parabolic fit method and the time derivative method provide very similar results. Since the calculation of the current signal with the time derivative method is faster and more convenient in terms of computing power, this latter method has been chosen to perform the

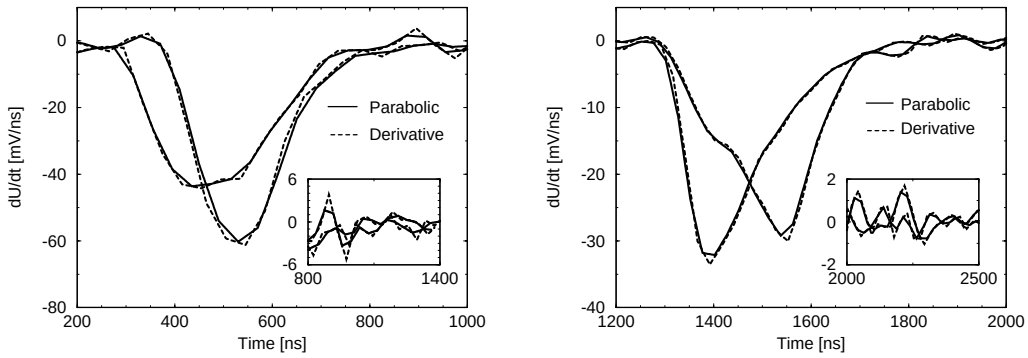


Figure 5.11: Comparison between the current pulse shape calculated using the parabolic fit (solid line) and the time derivative (dashed line) routine, for the centre (left) and for the outer contact B3 (right). The two methods provide a very similar result for the leading edge of the pulse, but the parabolic fit method helps in reducing the noise oscillations in the baseline (zoom).

following analysis.

## 5.4 Position resolution

The method developed in this work for position determination is based on the calculation of the collection time of the electron-hole pairs created by the $\gamma$-ray interaction.
In the energy range from 200 keV to a few MeV, Compton scattering is the predominant mechanism of interaction, which means that the absorption of a $\gamma$ ray requires more than one interaction point (see Appendix A.1). Interaction points belonging to the same $\gamma$ ray and occurring within the same detector segment cannot be detected separately, since the maximum time between interactions (of the order of hundreds picoseconds) is much shorter than the charge collection time (of the order of hundreds nanoseconds). The position of the individual interactions therefore has to be compared with the Compton scattering formula and the concept of the *main* and the *first* interaction has to be introduced. The main interaction is defined as the interaction which deposits most of the $\gamma$-ray energy and dominates the current pulse shape. The first interaction corresponds to the entry point of the $\gamma$ ray and therefore defines its direction. Considering the experimental set-up, position

determination is ambiguous: the use of the collimator provides the position of the entry point of the $\gamma$ ray, the algorithm yields the position of the main interaction. This ambiguity has to be considered while establishing a correlation between the pulse shape parameters and the position of the collimator. In particular, care must be exercised when performing a Doppler broadening correction, which requires the determination of the entry point of the $\gamma$ ray.

A much more demanding task is to determine the position of multiple interactions in multiple segments [Gat01]. In order to understand such a complex signal, the preamplifier output pulse shape must be decomposed into its individual components. In the framework of the $\gamma$-ray tracking community, deconvolution algorithms, like artificial neural networks (ANN) and genetic algorithms (GA), are currently being developed [Aga01]. In the following analysis, only fold-1 events, depositing all the energy in one segment, are examined. Over-complications arising from the superposition of two coincident interactions or an image charge superimposed to a real charge signal are beyond the scope of this work.

Examples of signal shapes for interactions occurring at three different positions are displayed in figures 5.12 and 5.13 for the centre and for a typical outer contact, respectively. The averaged signal, calculated by averaging the pulses at the same position, is also shown. The plots show a remarkable spread of signal shapes corresponding to the same position of the scanning table. This spread can be quantified by the full width at half maximum of the rise time distribution. Results on rise time distribution will be discussed in the next section. This spread, although not constituting an intrinsic limit to the achievable position resolution, represents the largest source of uncertainty in the calculation of the effective granularity of the detector. The spread in the signal shapes is mainly due to the uncertainty in the interaction position resulting from Compton scattering inside the same segments and from the finite opening angle of the collimator and not to the quality of the detector response itself.

This uncertainty prohibits, at this stage, an event-by-event signal classification and requires an averaging procedure to be used. Indeed, in order to obtain a signal, which represents the behaviour expected at the centre of the collimator, the pulse shapes have been sample-by-sample averaged.

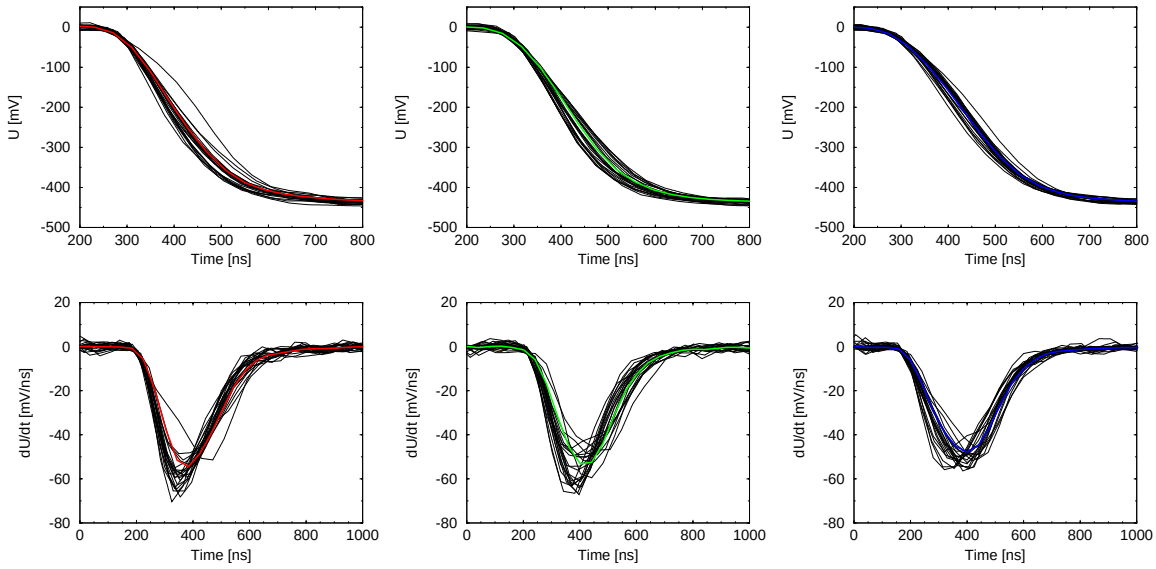


Figure 5.12: Measured set of charge pulses from the inner contact signal, digitized at 100 MHz, at three different interaction positions: close to the centre (top left), at intermediate radius (top middle) and close to the outside (top right). The averaged signal is shown for each position. In the bottom part of the plot the corresponding current signal are shown.

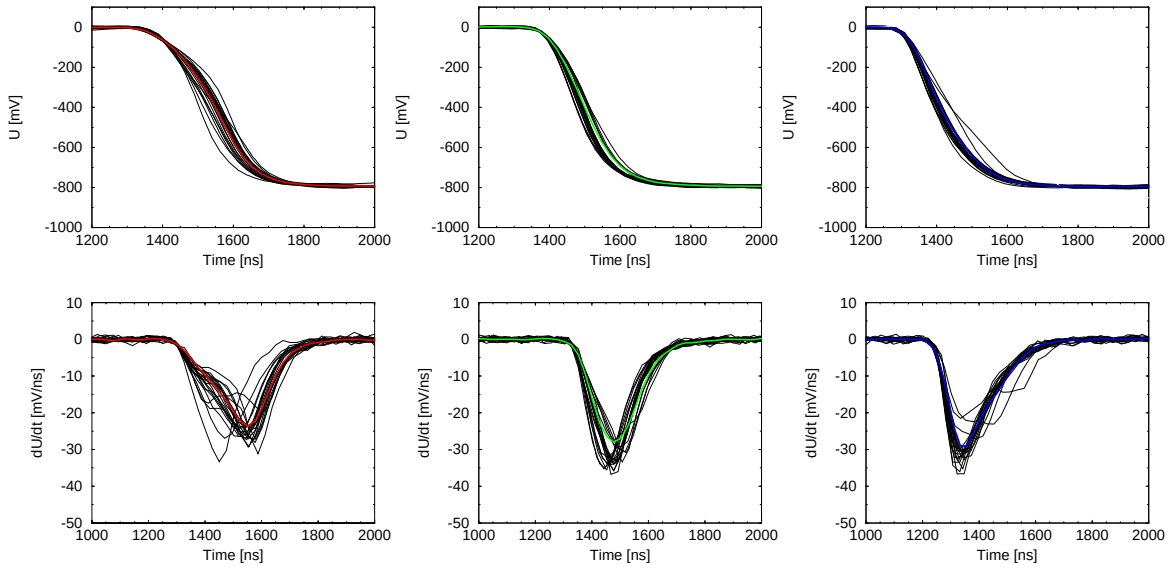


Figure 5.13: As above, but the set of pulses have been measured from a typical outer contact, digitized at 40 MHz.

### 5.4.1 Intrinsic limits

A distinction has to be made between the concepts of *position sensitivity* and *position resolution*:

- The position sensitivity measures the variation of the signal shape as a function of interaction position, relative to the noise level. Limitations in the position sensitivity are due only to the quality of the signal shapes (noise level in the detector, sampling frequency and dynamic range of the waveform digitizer). A position sensitivity better than 1 mm is achievable and it has been experimentally obtained from the GRETA prototype detector [Vet00].

- The position resolution indicates the minimum separation distance between interactions which can be distinguished. Intrinsic sources of uncertainty, which limit the achievable position resolution are:

  - The finite range of the primary electron in the crystal [Muk76]. At each interaction point, the $\gamma$ ray transfers energy to an electron, which, is stopped within a range $<$1 mm. The absorption of the primary electron occurs via the production of free charge carriers. Although it can be assumed that all charge carriers are generated within a point like volume, the range of the primary electrons may represent an uncertainty in position determination.

  - The uncertainty in the energy-angle relation of the Compton formula due to the Compton profile. In order to simplify the description of the Compton scattering mechanism, it is assumed that the binding energy and the initial momentum of the photo-electron are zero. If a very high position resolution is required, the momentum distribution of electrons in germanium has to be considered [Bri75]. The uncertainty arising from the Compton profile is of $\sim$0.7 mm.

  - The broadening of the distribution of the charge carriers travelling towards the electrodes. These effects have been calculated to be less than 0.1 mm and therefore do not represent a serious limitation [GRE00].

## 5.5 Energy information

The capability of extracting accurate energy information from the digitized pulse shape is fundamental for performing $\gamma$-ray tracking. In this section, results obtained with the moving window deconvolution method and the parabolic fit method, will be presented and compared.

### Moving window deconvolution results

The MWD method has been used to reconstruct the original charge event. The energy has been calculated as the average value of the total charge deposited by the $\gamma$-ray interaction and different energy spectra have been produced by varying the width of the window used to deconvolve the signals. An example of energy spectrum obtained from a typical outer contact signal digitized at 40 MHz (segment B3) is presented in Fig. 5.14. The energy resolution has been calculated as the FWHM of the 662 keV $^{137}$Cs peak. The FWHM values measured as a function of the window width are presented in Fig. 5.15. The results show that the method strongly depends on the width of the deconvolution window and a minimum window of 8 $\mu$s has to be used in order to obtain good energy resolution. The best achieved FWHM was 3.3 keV and was measured with a window of 11.25 $\mu$s (450 sampled points at 25 ns per sample).

An alternative energy resolution measurement, performed in the same experimental environment using conventional analogue electronics, provided a value of 2.8 keV. Although the FWHM obtained with the MWD method is 18% worse than the value measured with analogue electronics, the two results are consistent if an uncertainty of $\sim$5% is considered in the measurements. A further reason for the worse resolution performance of the digital electronics, can be the introduction of noise arising when all the electronic channels of the detector are connected to the readout FADCs. When the energy resolution was measured with conventional analogue electronics, only the channel under test was connected. Furthermore, a small noise pick-up from the stepper motor and reproducible periodic oscillations in the pulse base line were observed in the digital system.

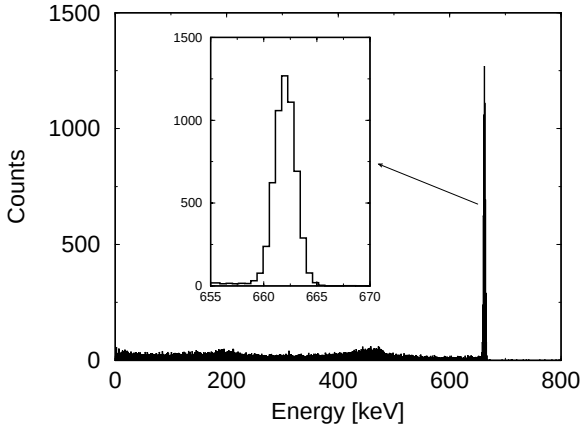


Figure 5.14: A typical energy spectrum obtained from contact B3 using a deconvolution window of 11.25 $\mu$s.

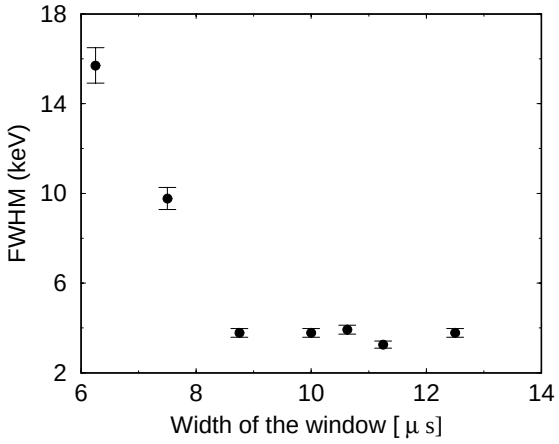


Figure 5.15: FWHM of the 662 keV peak, measured by using the MWD method from a typical outer contact signal (B3), as a function of the width of the deconvolution window. A window of $\sim$8 $\mu$s is required in order to obtain good energy resolution.

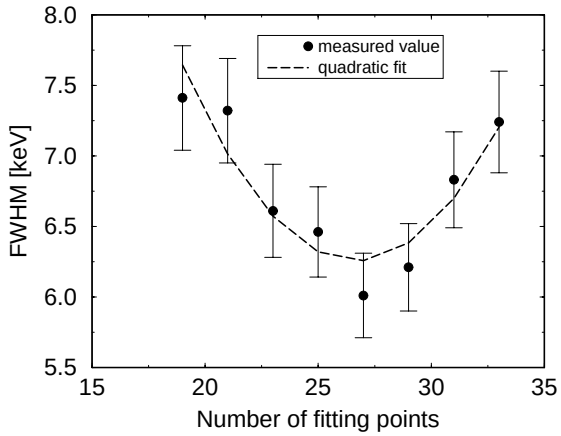


Figure 5.16: Plot of the FWHM as a function of the number of smoothing points used in the parabolic fit algorithm. The best energy resolution achieved corresponds to 27 fitting points. The errors on energy resolution measurements are typically $\leq$5 %.

### Parabolic fit results

The current signal has been extracted using the parabolic fit method and the energy spectrum has been obtained by calculating the energy as the integral of the current pulses. As above, the energy resolution refers to the FWHM of the 662 keV peak. The number of data points used in the fit was varied and the results showed a dependence of the energy resolution on the fitting points. The results obtained from contact B3 are reported in Fig. 5.16. The best achieved resolution was $\sim$6 keV, with a window of 27 points.

From the above results it can be concluded that the moving window deconvolution method provides the best performance in terms of energy resolution. Furthermore, as presented in Fig. 5.11, current pulses can also been calculated by means of a simple time derivative, which provides results very similar to those produced by the parabolic fit method, using a window of 3 fitting points. It was therefore decided to use the MWD routine to calculate the energy and the time derivative to extract the current signals in the developed PSA algorithm.

## 5.6 Position information

In this section, the feasibility of the pulse shape analysis method as a tool for extracting position information will be investigated. From pulse shapes corresponding to known positions of the scanning table, the rise time parameters are calculated and compared.

### 5.6.1 T30, T60 and T90 distributions

In order to understand fully the dependence of the rise time parameters on the interaction position of a $\gamma$ ray, the T30, T60 and T90 rise time values have been extracted in correspondence with each of the positions considered in the fine scan of the detector. Rise time values have been plotted as a function of the radial distance from the centre contact surface, in a 2D-contour plot representation. Results obtained from the centre contact are shown in Fig. 5.17, where the number of times each rise time value was measured is indicated by the colour scale; only events corresponding to a full energy deposition in a given segment of slice B have been considered in the analysis.

The T30 values increase as a function of the interaction radius. At small radii, the T30 rise time reaches a saturation value of about 35 ns. The T60 and T90 distributions, instead, present the characteristic V-shapes with minimum close to mid radii.
As explained in section 5.1, this behaviour is typical for the centre contact preamplifier pulse and arises from the particular shape of the signal leading edge. The fact that the T30 time reaches a saturation value at small radii is also a consequence of the time response of the preamplifier circuit and of the finite sampling interval of our measurement system, which does not allow a measure of very small rise time variations. In order to enlarge the spread in the rise time distributions, the preamplifier contribution was subtracted in quadrature from the measured value, as:

$$TX0 = \sqrt{TX0^2_{meas} - TX0^2_{pream}} \tag{5.18}$$

where $TX0$ stands for either T30, T60 or T90 and $T30_{pream}$=10 ns, $T60_{pream}$=19 ns, $T90_{pream}$=29 ns.
The minimum value in the T90 distribution is about 160 ns, which occurs at a radial distance of about 16 mm from the inner contact surface (i.e. at a radius of about 20 mm from the

centre of the detector). This result is in good agreement with the value of 15 mm, obtained from equation 5.1. The value of 160 ns also agrees with the theoretical saturation velocity.

The number of counts indicated by the colour scale has been normalised over the whole detector solid angle, in order to enable a fair comparison at small and at large radii. The larger number of counts observed at mid radii is a consequence of the larger photopeak efficiency in this part of the detector volume, as indicated in the previous chapter.

Results from the outer contacts B3 and C3 are presented, as typical examples, in figures 5.18 and 5.19. The T90 distributions show the same trend observed for the centre contact, while the T30 values decrease, as the radius of the interaction increases. The shape of the outer contact signal is the reflection symmetric image of the corresponding inner contact signal. The peak in the frequency distribution that appears at mid radii is again statistical and is due to the higher photopeak efficiency in the middle of the crystal.

In figures 5.20 and 5.21, results obtained in the front and back part of the detector are presented. The results show a complicated response with no clear distribution of rise time as a function of radial position. In the previous chapter it was discussed how the electric field in the closed-ended part and in the back part of the detector is not truly coaxial, being very weak at the front edge, nearly uniform at the front centre and complex at the back. The electric field distribution strongly influences the shapes of the signal, due to charge collection effects which, for interactions occurring in these regions of the detector, do not present the typical behaviour observed in the coaxial part. For interactions occurring in slice A, in front of the central contact, the holes are more likely to be collected at the front of the detector. In this case they do not have to travel the radial distance between the interaction point and the outer electrode, this results in a faster rise time. The analysis of the rise time distribution as a function of the radial position is also affected by the poor statistics obtained close to the crystal edge and at the back (D) of the detector, as was discussed in the previous chapter.

In order to extract meaningful information from the signal shape corresponding to interaction in the front and in the back part of the detector, a more sophisticated pulse shape analysis technique has to be developed. Understanding the experimental behaviour of the signal shape in these parts of the detector is beyond the scope of this work.

By taking slices of the above 2D-plots, the shape of the rise time distribution at a

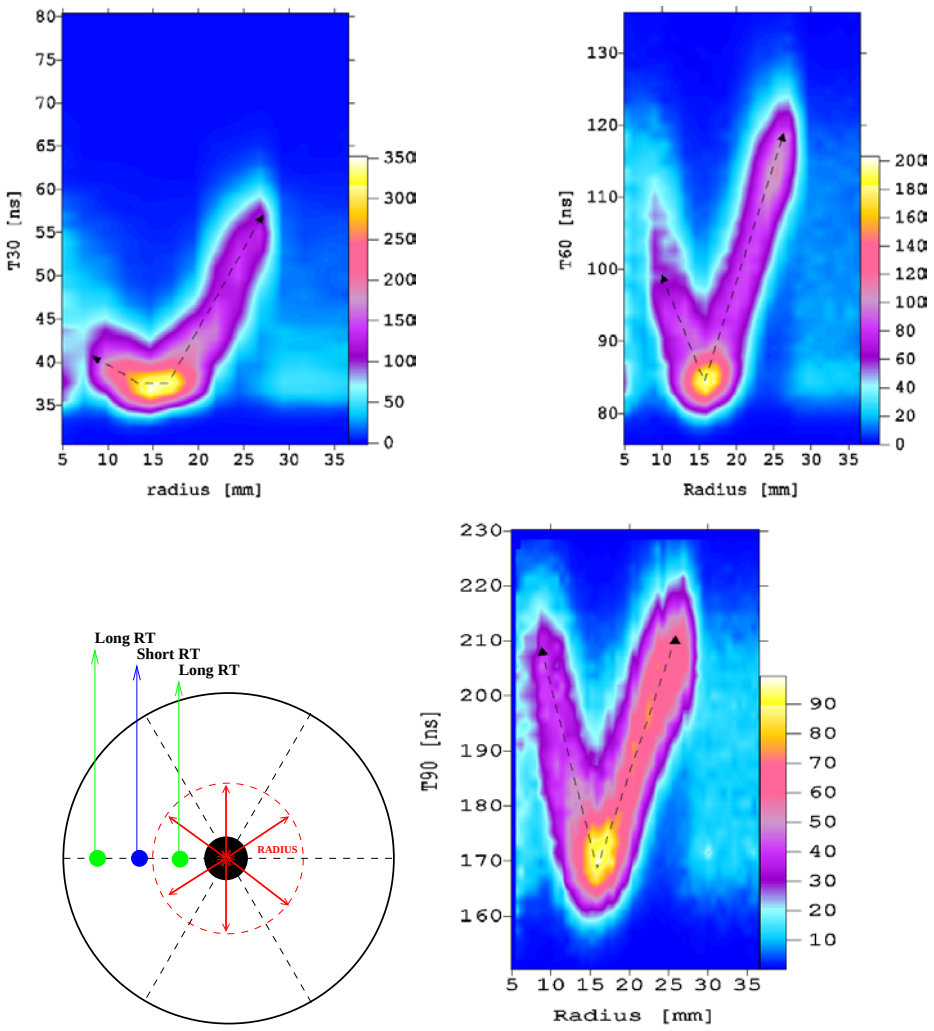


Figure 5.17: Distribution of T30 (top left), T60 (top right) and T90 (bottom right) values, measured on the centre contact signal, as a function of the radial position of the interaction. Full energy interactions occurring in any segment of slice B of the detector have been considered. The colour scale indicates the number of times that the same value has been measured. The frequency distributions have been normalised for the solid angle. The higher number of counts at mid radii (yellow blob in the plot) is statistical: the photopeak efficiency is higher in this part of the detector and decreases towards the centre and towards the edge. The T30 distribution decreases as the interaction radius increases, until it reaches a saturation value; the T60 and T90 distributions present the characteristic V-shape, with minimum at intermediate radii. The scale of the number of counts is reduced following the normalisation.

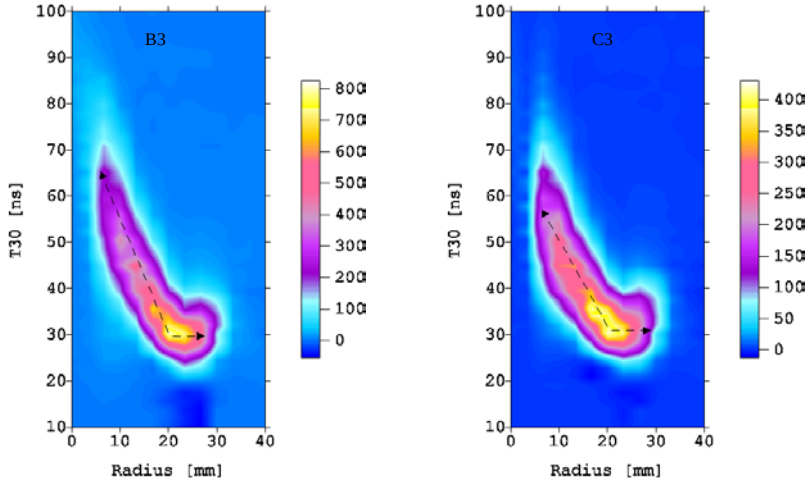


Figure 5.18: T30 distributions as a function of the radial position of the interaction, measured from outer contact B3 (left) and C3 (right). The frequency distributions have been normalised for the solid angle.

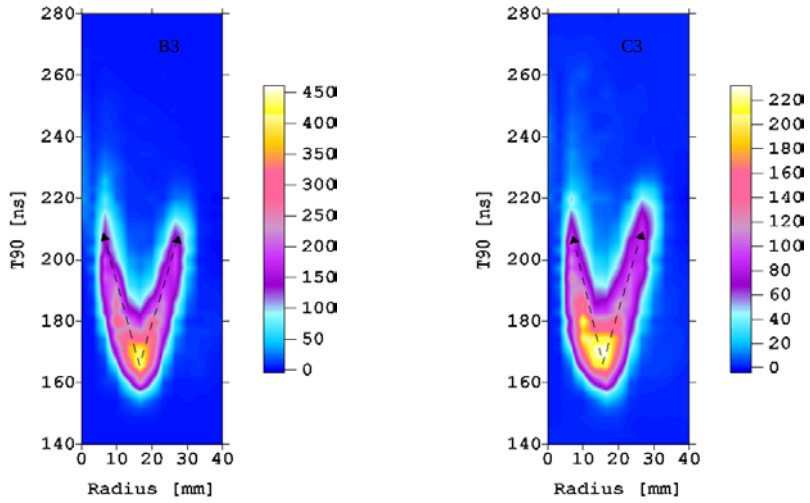


Figure 5.19: T90 distributions as a function of the radial position of the interaction, measured from contact B3 (left) and C3 (right). The frequency distribution has been normalised for the solid angle.

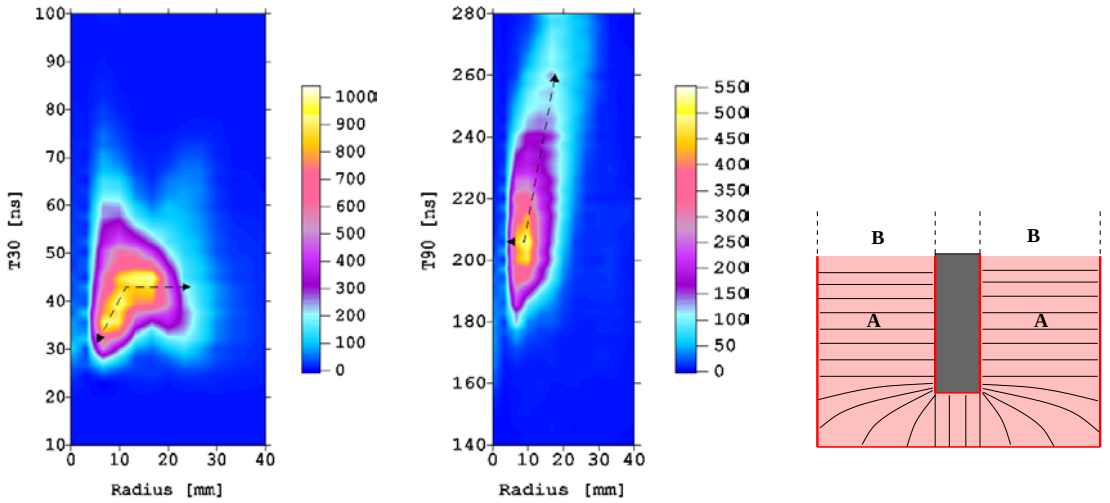


Figure 5.20: These plots show the T30 (left) and T90 (middle) distribution as a function of the radial position of the interaction, measured from contact A3, and the schematic electric field distribution in the front slice of the detector (right).

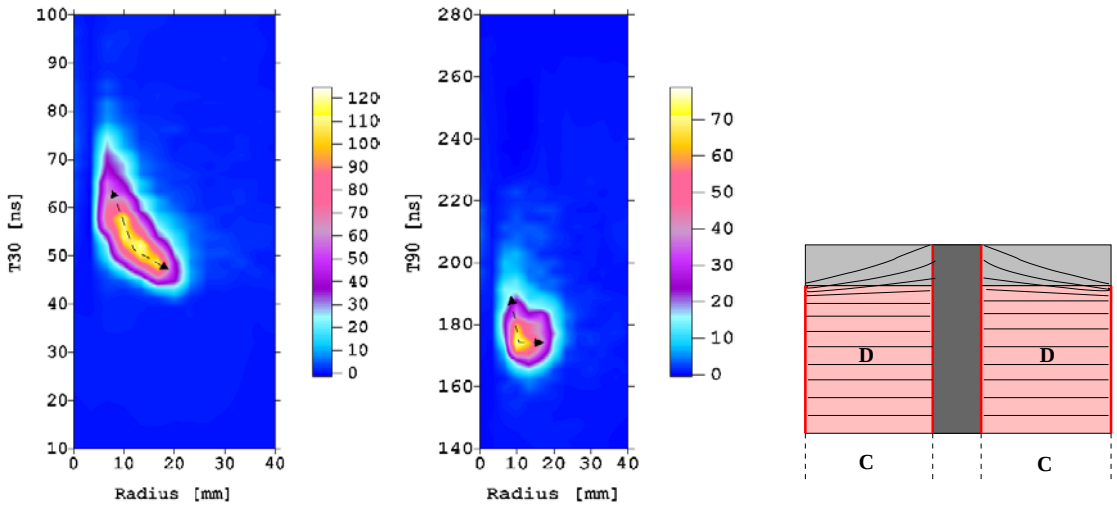


Figure 5.21: These plots show the T30 (left) and T90 (middle) distribution as a function of the radial position of the interaction, measured from contact D3, and the schematic electric field distribution in the back slice of the detector (right).

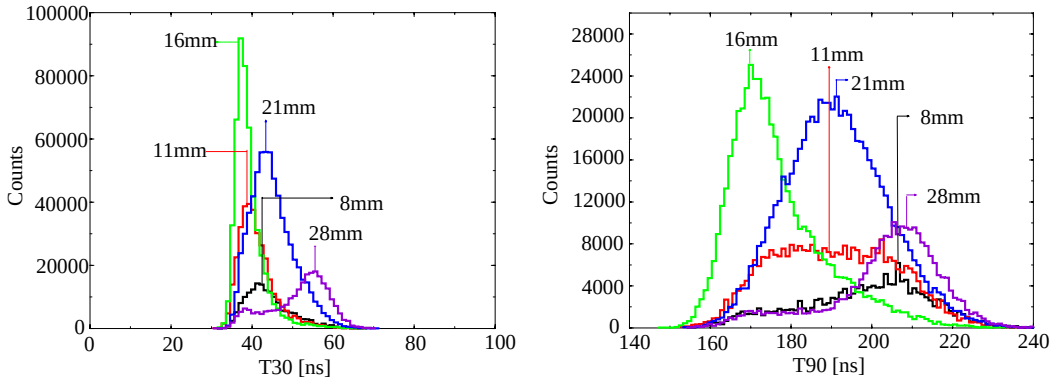


Figure 5.22: The T30 (left) and T90 (right) distribution at five different radial distances, namely 8 mm, 11 mm, 16 mm 21 mm and 28 mm, from the surface of the centre contact. The rise time values have been measured from the centre contact signal, in correspondence to photopeak events in any of the segments of slice B. All the data from the fine scan have been considered in the analysis.

given radial position is obtained. Fig. 5.22 shows the results for the centre contact signal at five given radial distances, namely 8 mm, 11 mm, 16 mm, 21 mm and 28 mm.

The T90 rise time distributions present marked non-Gaussian shapes, whose uncertainty depends on the radial position of the interaction. The distributions corresponding to 16 mm and 21 mm have more symmetric shapes, the FWHM is smaller at 16 mm ($\sim$18 ns) and larger at 21 mm ($\sim$30 ns). The distribution at 11 mm presents a wide flat top with a FWHM of $\sim$47 ns. The distributions at 8 mm and 28 mm have long tails, which extend over a large range of rise time values. Similar considerations apply for the T30 distributions. The reason for the very wide distribution of rise time values observed at extreme radii is not clear at this stage of the analysis.

Figures 5.23 and 5.24 present T30 and T90 rise time distributions, obtained by taking slices, at five different radial distances, of the 2D-plots measured from contacts B3 and C3. The histograms present the same characteristics discussed for the centre contact.

Evidence of the relationship existing between the rise time of the pulse and the radial position of the interaction has been qualitatively demonstrated. The following analysis is aimed to find a quantitative method, which will enable one to relate, on an event-by-event base, the measured rise time with the position of the interaction.

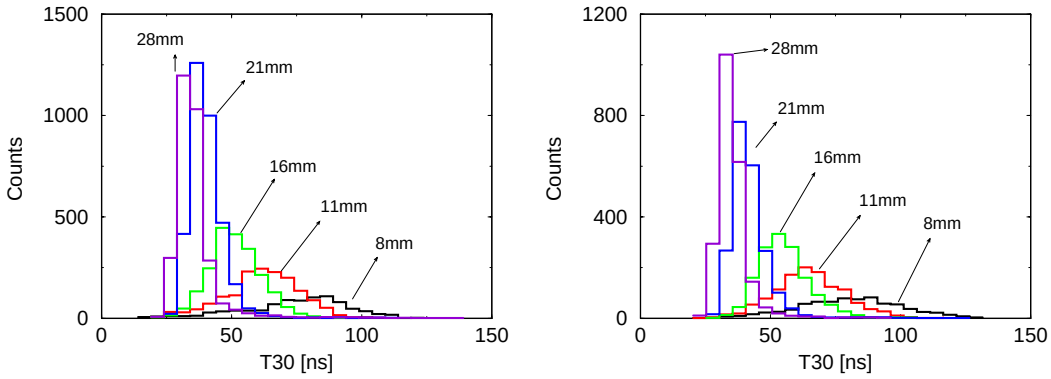


Figure 5.23: These plots show the T30 distribution measured from outer contact B3 (left) and C3 (right), at five different radial distance, namely 8 mm, 11 mm, 16 mm, 21 mm and 28 mm, from the surface of the centre contact. Only photopeak events have been considered in the analysis.

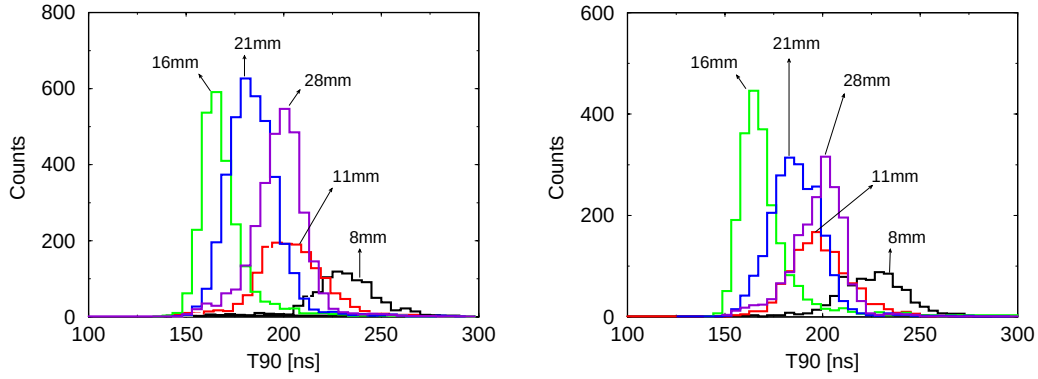


Figure 5.24: These plots show the T90 distribution measured from outer contact B3 (left) and C3 (right), at five different radial distance, namely 8 mm, 11 mm, 16 mm, 21 mm and 28 mm, from the surface of the centre contact. Only photopeak events have been considered in the analysis.

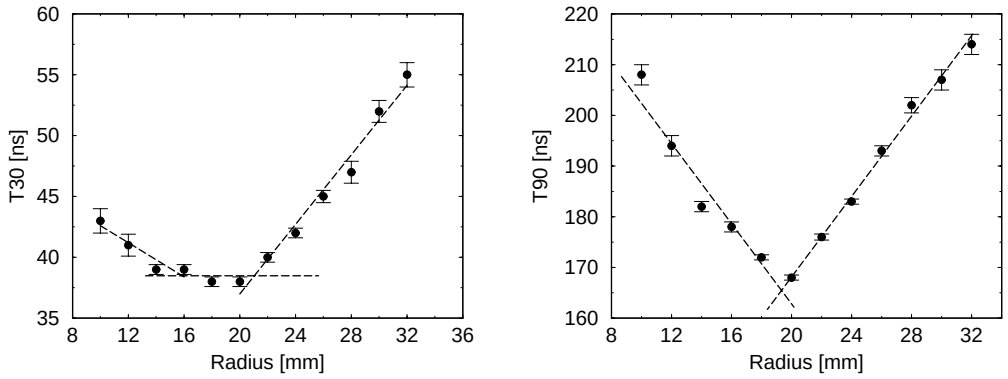


Figure 5.25: The plots show T30 (left) and T90 (right) centre contact values as a function of the radial position. The rise time values have been calculated as the centroid of the rise time distributions obtained by taking slices, at given radii, of the 2D-plots shown in Fig. 5.17. The errors have been estimated, point by point, on the basis of the spread of the rise time values at each given radius (see Fig. 5.22).

The centroids of the T30 and T90 distribution of figures 5.17, 5.18 and 5.19 have been calculated and plotted as a function of the radius. Results are presented in Fig. 5.25 for the centre contact signal and in Fig. 5.26 for the outer contact B3. The error on the centroid has been estimated from a visual inspection of the rise time distributions and ranges from 0.5 ns to 5 ns. Due to the asymmetric shape of the peak, this estimate was considered more reliable than any calculations. As a consequence, the following analysis will be appropriate only for the data which fall in the peak and not for those forming the tail (i.e. $\sim$20% of the events). The plots show evidence of a linear relationship between rise time and radial position. Therefore, two straight lines of the form:

$$y_i = ax_i + b, \tag{5.19}$$

have been fitted to the data for radii $\leq$19 mm and $>$19 mm. In the above expression, $y_i$ are the measured rise time values and $x_i$ are the known radial positions of the collimator. The slope, $a$, the intercept, $b$, and the respective errors, $\sigma_a$ and $\sigma_b$, have been calculated assuming that: (1) the values ($x_i$, $y_i$) were statistically independent, (2) the uncertainty of the radial position was much smaller than the uncertainty of the rise time value ($\sigma_x \ll \sigma_y$), (3) the uncertainties of the $y_i$ values are all the same (or very similar).

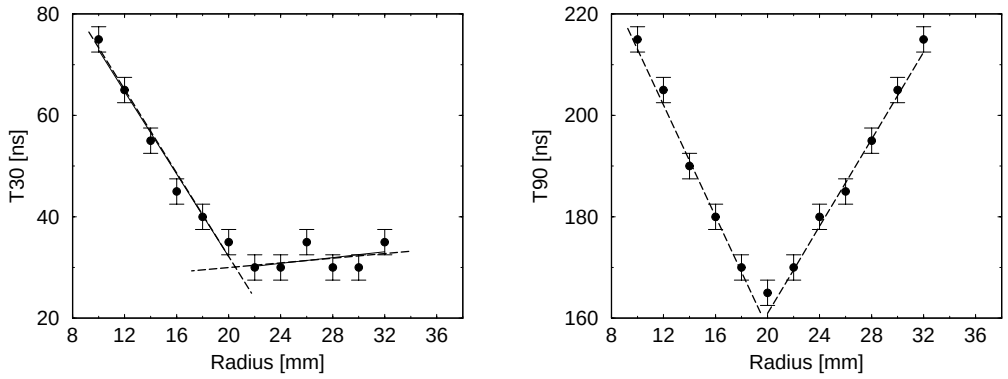


Figure 5.26: The plots show T30 (left) and T90 (right) outer contact (B3) values as a function of the radial position. The rise time values have been calculated as the centroid of the rise time distributions obtained by taking slices, at given radii, of the the 2D-plot shown in figures 5.18 and 5.19. The errors have been estimated, point by point, on the basis of the spread of the rise time values at each given radius (see figures 5.23 and 5.24).

Following the fit, an additional estimate of the uncertainty of the rise time determination, $\sigma_y$, is calculated from the expression [Lor94]:

$$\sigma_y^2 = \frac{\sum_i [(ax_i + b) - y_i]^2}{N - 2}. \tag{5.20}$$

This value represents the uncertainty associated to the measured rise time. The results from the fit are summarised in Tab. 5.1, both for the centre and for the outer contact.

Using the parameters of the fit, for any given rise time value, it is possible to reconstruct the radial position of the interaction, $x_i$ and its error, $\sigma_{x_i}$:

$$x_i = \frac{y_i - b}{a}, \tag{5.21}$$

$$\sigma_{x_i} = x_i \sqrt{\frac{\sigma_a^2 + \sigma_y^2}{(y_i - a)^2} + \left(\frac{\sigma_b}{b}\right)^2}. \tag{5.22}$$

In order to verify the accuracy of the method, 100 pulse shapes from the centre contact signal, corresponding to a radial collimator position of 27 mm, were analysed and the T90 and T30 values were extracted. Fig. 5.27 shows, for each pulse shape, the T30 value plotted against the T90 value. The (T90,T30) values show a considerable spread, as expected following the discussion reported in section 5.4.

| Fit | $a$ [ns/mm] | $\sigma_a$ [ns/mm] | $b$ [ns] | $\sigma_b$ [ns] | $\sigma_y[ns]$ | $\chi^2$ |
|---|---|---|---|---|---|---|
| Centre contact | | | | | | |
| T90 ($r \leq$19 mm) | -4.40 | 0.39 | 248 | 6 | 3.93 | 2.47 |
| T90 ($r >$19 mm) | +3.99 | 0.11 | 88 | 2 | 2.57 | 0.94 |
| T30 ($r \leq$19 mm) | -0.70 | 0.22 | 49 | 3 | 0.77 | 0.60 |
| T30 ($r >$19 mm) | +1.43 | 0.94 | 8 | 2 | 2.62 | 1.02 |
| Outer contact | | | | | | |
| T90 ($r \leq$19 mm) | -5.44 | 0.18 | 267 | 3 | 2.03 | 1.79 |
| T90 ($r >$19 mm) | 4.29 | 0.22 | 75 | 6 | 2.57 | 1.49 |
| T30 ($r \leq$19 mm) | -4.07 | 0.30 | 113 | 4 | 2.60 | 1.08 |
| T30 ($r >$19 mm) | 0.28 | 0.29 | 23 | 8 | 2.63 | 1.10 |

Table 5.1: The rise time values as a function of the radial position have been fitted with a straight line. The parameters extracted from the centre contact and from a typical outer contact (B3) are reported here. The $\chi^2$ gives an indication on the quality of the fit.

By ignoring the knowledge of the collimator position, it is possible to reconstruct the position of the interaction by using equation 5.21. Given a T90 value, *a priori*, there is no reason for choosing between the fit extracted for $r >$19 mm or $r \leq$19 mm. The ambiguity is removed by calculating the radial position from the T30 values. Radial positions were calculated from each T90 and T30 value using both fits. Fig. 5.28 shows the the radial position obtained from the T90 fit plotted against that obtained from the T30 fit, for $r >$19 mm. The results have been averaged in order to obtain a reasonable estimate of the true position of the interaction. As already explained, due to the finite opening angle of the collimator and Compton scattering, the various interactions do not occur at the same position in the detector. It can therefore be assumed that the average value corresponds to the average position of the collimator, i.e. the collimator centre. The average T90 value is 194.8±2.6 ns (the relative error is 1.3%), the average T30 value is 48.0±2.6 ns (the relative error is 5.5%). Results for the radial position are reported in Tab. 5.2. It is evident the only possible solution is 26.7 mm, which is in very good agreement[2] with the position of the collimator (27 mm).

[2]A physical quantity $X_{true}$ and its experimental value $X_{meas}$ are consistent if $\tau = \frac{X_{true}-X_{meas}}{\sigma} <3$. In this case $\tau$=0.22, showing a very good agreement.

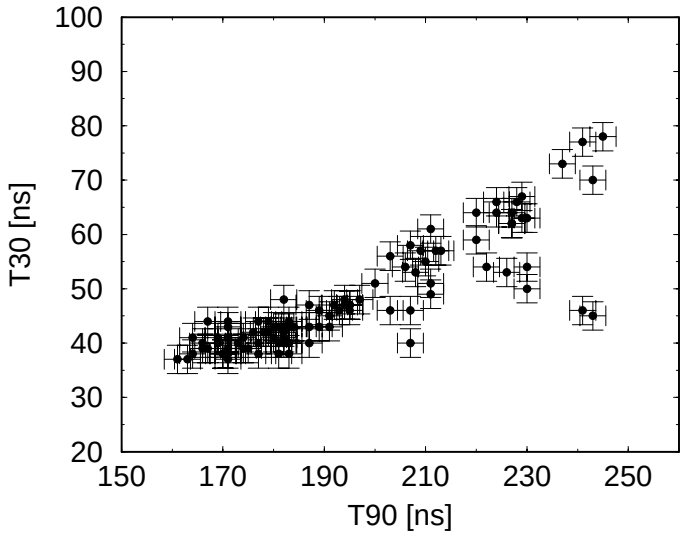


Figure 5.27: T30 versus T90 values, calculated for 100 pulse shapes at the known collimator radial distance of 27 mm. The pulse shapes were measured from the centre contact signal. For the 100 pulse shapes, the average T90 value is 194.77±2.57 ns, the average T30 value is 47.97±2.62, where the errors have been extracted from the fit ($\sigma_y$).

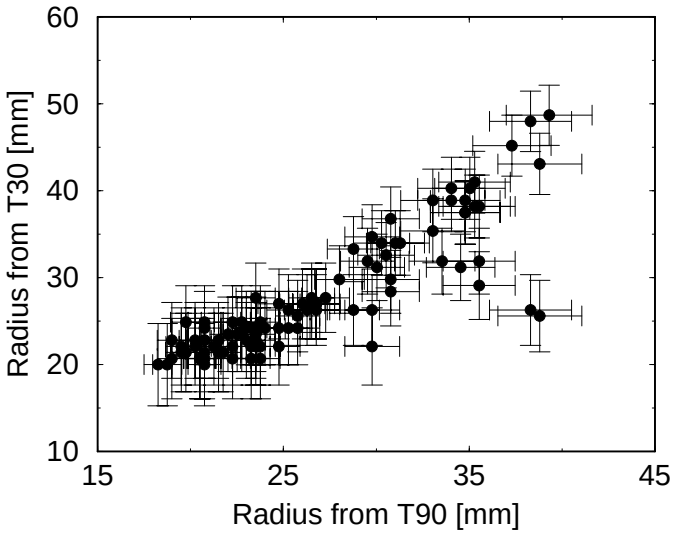


Figure 5.28: For the 100 pulse shapes, the radial position of the interaction from the T30 fit has been plotted versus that from the T90 fit, for $r$ >19 mm. The errors have been extracted from equation 5.22.

| From fit | T90 ($r \leq 19$) | T90 ($r > 19$) | T30 ($r \leq 19$) | T30 ($r > 19$) |
|---|---|---|---|---|
| radius [mm] | 12.1±0.4 | **26.7±1.3** | 1.5±0.5 | **27.7±4.1** |

Table 5.2: Radial position of the interaction obtained from the specified fit. The results are consistent with a radial position of 27 mm.

Due to the smaller uncertainty provided by the T90 fit, it has been decided to consider, as the estimate of the radial position, the value 26.7±1.3 mm, instead of the average value between the T90 fit and the T30 fit, i.e. 27.2±4.3 mm. The uncertainty in the T90 radial position determination is 4.8%.

In general, the T90 fit enables the radial position of the interaction to be obtained, with an uncertainty of 4% for radii larger than 19 mm and of 19% otherwise. This means that the position resolution achievable ranges from 0.6 mm to 3.3 mm.
These results provide the radial calibration of the response function of the detector and the experimental uncertainty in the position determination.

### Polar plot

A very useful method for studying the rise time variation as a function of the interaction position is provided by the polar plot. A polar plot is obtained by incrementing in the x-y plane the position of the collimator with the most probable value of the rise time measured at that position. The centroid of the distribution was calculated as discussed in the previous section. Results produced with this method are presented in Fig. 5.29. The plots show the T30, T60 and T90 rise time values measured from the centre contact in correspondence to fold-1 photopeak events. The value of the rise time at each position is given by the colour scale. The polar plots show the same dependence of the rise time values on the radial position of the interaction observed in the V-shape plots; indeed the V-shape plots can be considered as slices of these polar plots.
The results show a clear asymmetry in the rise time distribution due to crystal orientation effects. For a given radius, the rise time is shorter along the $\langle 100 \rangle$ direction, where the drift velocity of the charge carriers is larger, and larger along $\langle 110 \rangle$ direction, where the drift velocity is smaller (see Fig. 2.12). Polar plots enable a qualitative measurement of

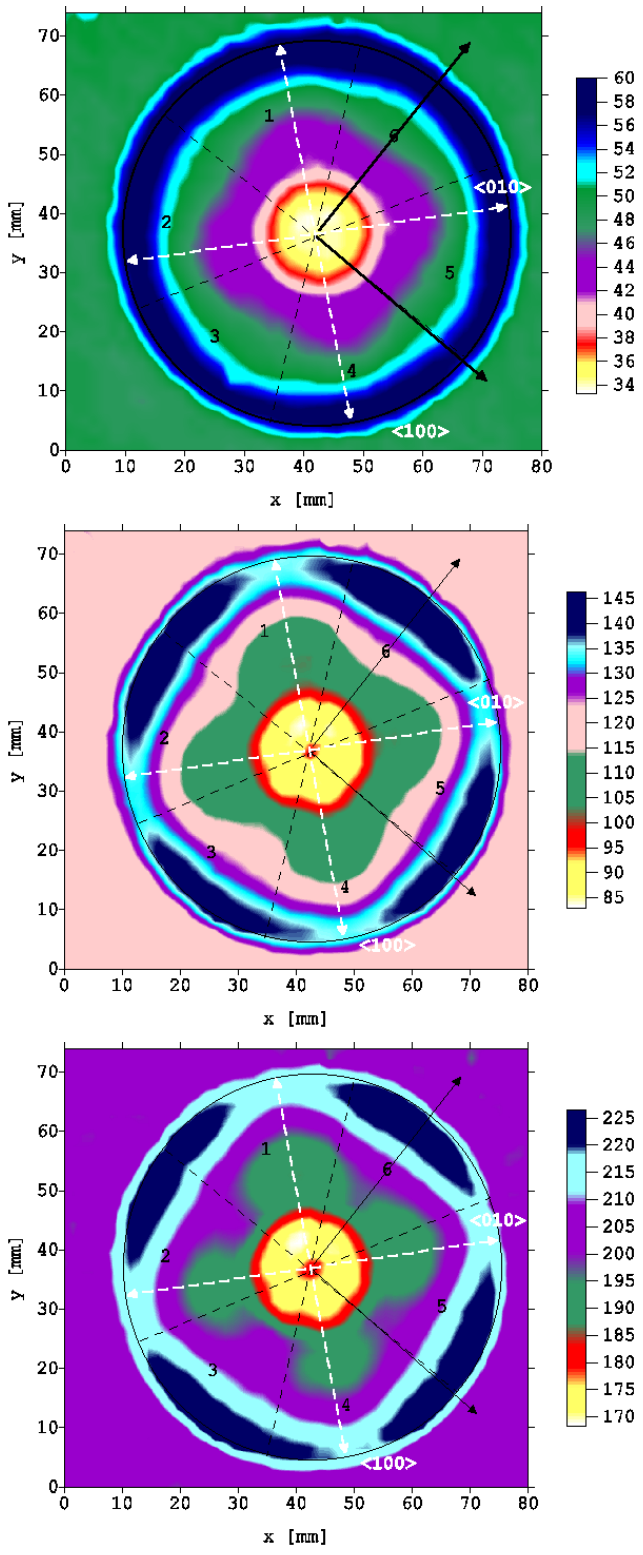


Figure 5.29: Polar plots showing the rise time T30 (top), T60 (middle) and T90 (bottom) as a function of the position of the scanning table. The results refer to $\gamma$-ray events fully absorbed within a single segment and measured from the centre contact signal. The units of the colour scale are nanoseconds.

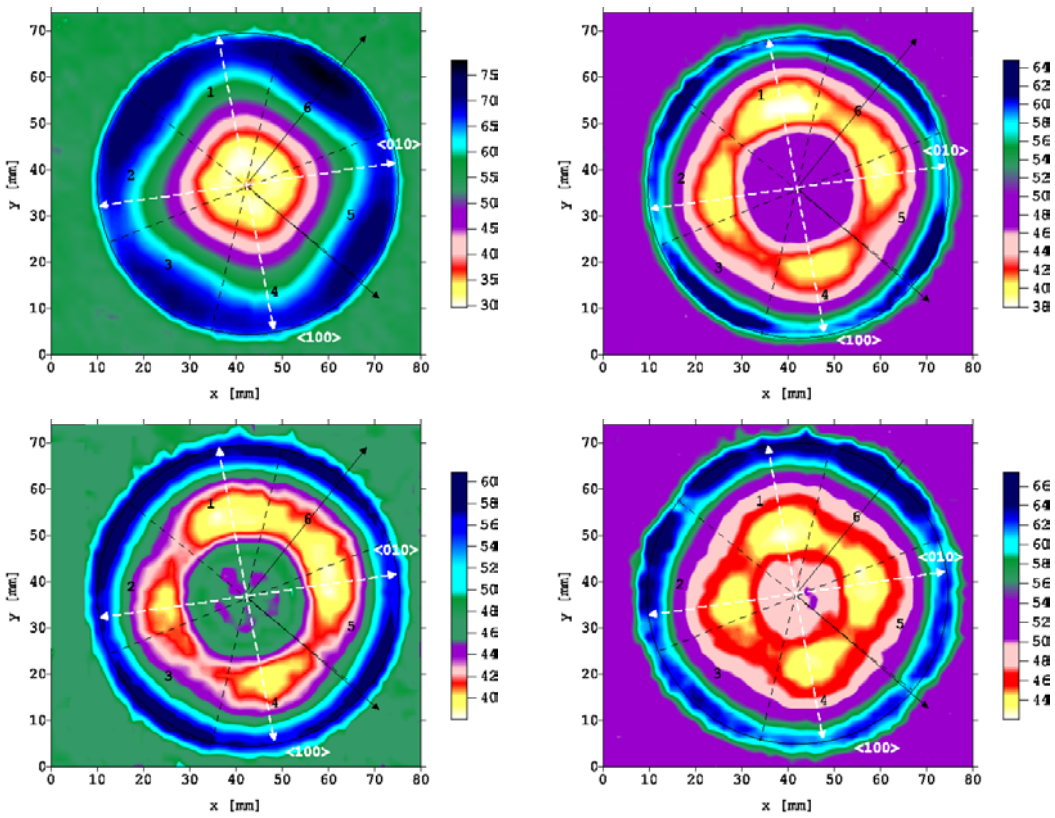


Figure 5.30: T30 polar plots corresponding to photopeak events in slice A (top left), slice B (top right), slice C (bottom left) and slice D (bottom right). The T30 rise time values have been measured from the centre contact. The units of the colour scale are nanoseconds.

the crystallographic orientation of the germanium lattice to be obtained. The assignment of crystallographic orientation was based on these results.

In order to study the influence of crystallographic orientation effects, and allow us to draw more conclusions on the influence of the electric field on charge collection, the polar plots have been produced for each slice of the detector, by considering separately photopeak events occurring in each segment of each given slice. T30, T60 and T90 polar plots for slices A, B, C and D of the detector, are presented in figures 5.30, 5.31 and 5.32, respectively.

The response function of slice A is always different from that of the other slices. In slice A, the T30, T60 and T90 rise times increase monotonically from the centre to the outside of the detector, as expected considering the different electric field distribution. The rise time values measured for events occurring close to the crystal edge, are about 14%

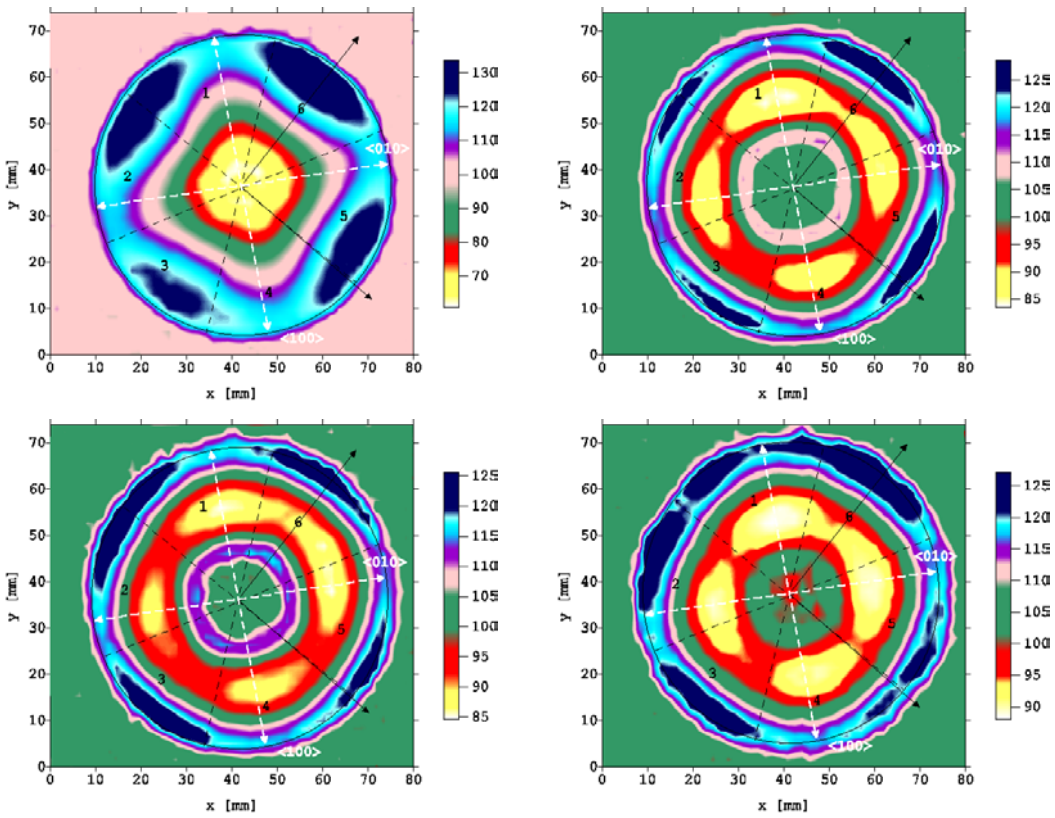


Figure 5.31: T60 polar plots corresponding to photopeak events in slice A (top left), slice B (top right), slice C (bottom left) and slice D (bottom right). The T60 rise time values have been measured from the centre contact. The units of the colour scale are nanoseconds.

larger than in the other slices, due to the weak electric field. The rise time measured for events occurring close to the centre, are systematically shorter. This result is a consequence of the different path travelled by the holes, which can be collected at the front face of the detector. The increase of the rise time along the $\langle 100 \rangle$ and $\langle 010 \rangle$ directions is clearly visible.

The rise time measured for events occurring in the other slices (B, C and D) reveal the typical behaviour as a function of the radial distance, observed in the V-shape plot. A marked dependence of the rise time values on the azimuthal position of the interaction is also observed.

In order to obtain a quantitative estimate of the effects of the anisotropy on the pulse shape rise time, the T90 values, measured from the centre contact in correspondence with fold-1 photopeak events in any of the segments of slice B, have been plotted as a function of

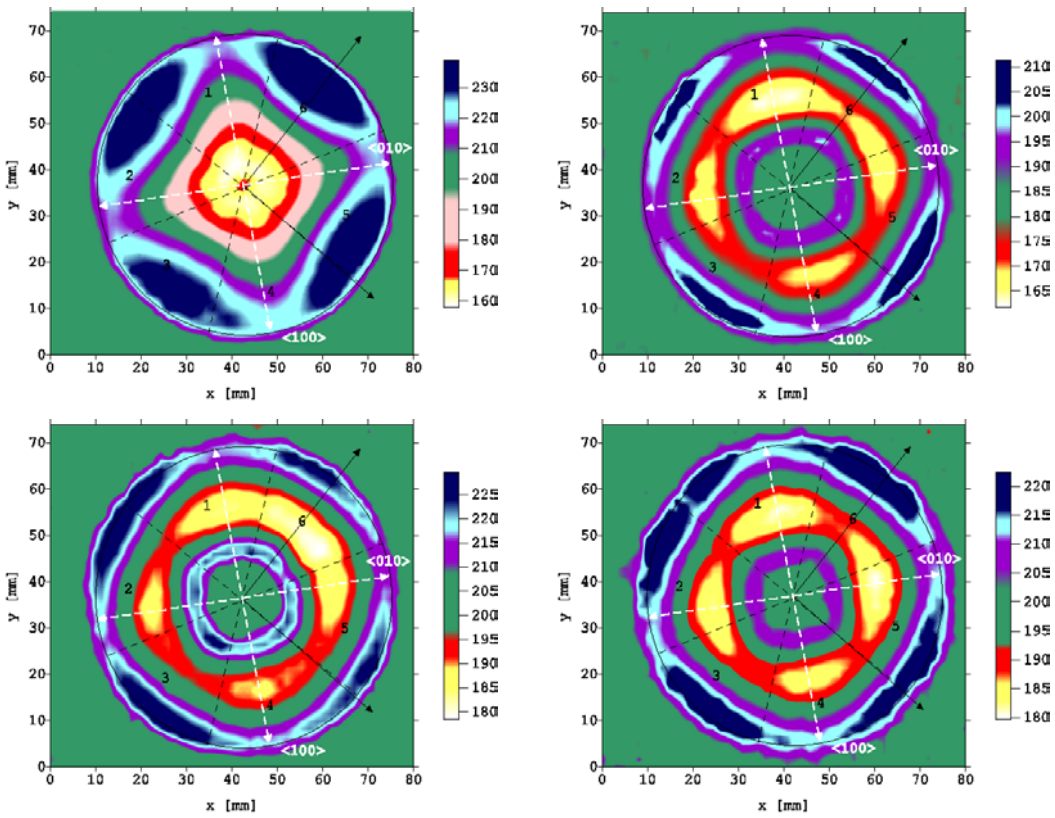


Figure 5.32: T90 polar plots corresponding to photopeak events in slice A (top left), slice B (top right), slice C (bottom left) and slice D (bottom right). The T90 rise time values have been measured from the centre contact. The units of the colour scale are nanoseconds.

the azimuthal angle of the interaction, $\phi$. Results are presented in Fig. 5.33 for two radial distances from the centre, namely 2.4 cm and 3.2 cm. Due to the symmetrical geometry of the detector, the variation of the rise time is a periodic function of the azimuthal angle and an overall variation of about 15 ns, at the same radial distance, is observed. This variation corresponds to a 25% increase in the rise time.

### 5.6.2 Analysis of the current pulses

As explained in section 5.2, a useful parameter for position determination is the time-to-maximum, $T_{max}$, of the current pulses. A polar plot showing the the time-to-maximum of the centre contact current pulses as a function of the collimator position is presented in Fig. 5.34. As in the previous analysis, only fold-1 full energy events have been considered.

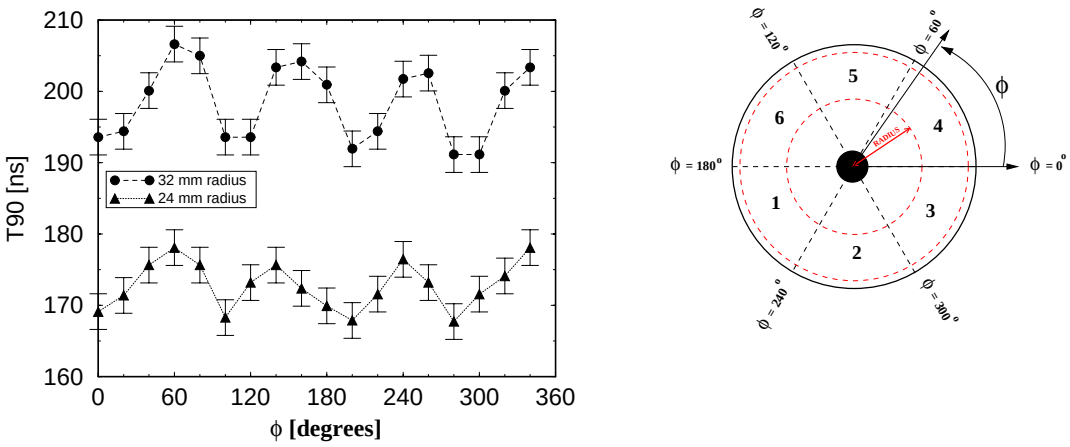


Figure 5.33: Variation of the T90 rise time as a function of the azimuthal angle $\phi$. The angle was measured, in degrees, starting from the boundary between sector-3 and sector-4. These results correspond to the T90 values measured from the centre contact signal, in correspondence with a fold-1 full energy event in slice B.

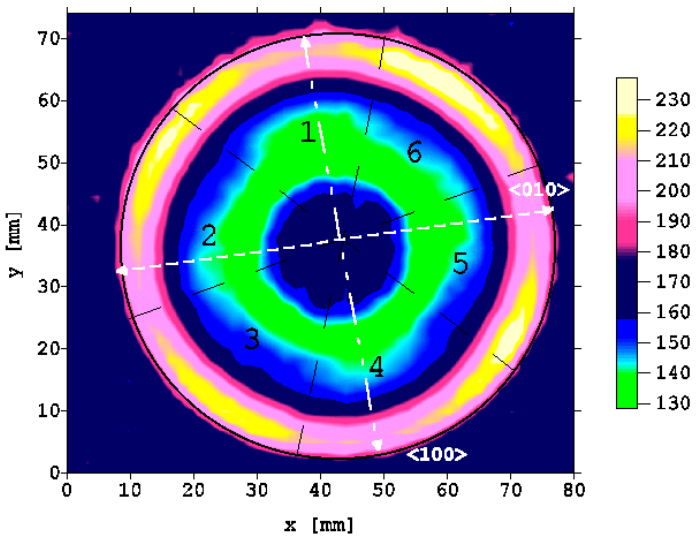


Figure 5.34: Polar plot showing the time-to-maximum of the current pulses measured from the centre contact. The units of the colour scale are nanoseconds.

As expected, the $T_{max}$, which corresponds to the collection time of the electrons, is long at the edge of the crystal and short near the centre. The sensitivity in measuring the short time-to-maximum near the inner contact is limited by the finite sampling interval of the FADCs and these values have the largest uncertainty.
The $T_{max}$ response is also influenced by crystallographic orientation effects and presents the same behaviour observed in the T90 polar plots.

**Azimuthal position information**

This section describes how to determine the azimuthal position of the interaction by exploiting the features of the transient charge signals. The asymmetry associated with a photopeak event in a given segment is calculated, accordingly to equation 5.2, as the difference between the amplitude of the transient charge signals induced in the two adjacent segments. Polar plots showing the value of the asymmetry, as a function of the position of the collimator, have been produced for fold-1 full energy events. The results for slice A and C are displayed in Fig. 5.35.
Because of the geometry of TIGRE, the plots show axial symmetry. Segment A2 can be considered as example. For interactions in the middle of the segment, the difference between the amplitude of the image charge induced in segments A1 and A3, is virtually zero. The transient charge signals observed in A1 and A3 have both the same small amplitude. The asymmetry then increases towards the boundary with segment A1 and decreases, becoming negative, towards the boundary with segment A3. If the interaction occurs closer to segment A1, the image charge induced in A1 is larger and that induced in segment A3 is smaller. The measurement of the asymmetry, therefore, provides azimuthal position information.
In the middle of the detector active volume, the asymmetry plots for slice A and for slice C present different characteristics. In slice C, at mid radii, the asymmetry is virtually zero not only in the middle of the segment, but also in a region which extends along the azimuthal direction. This behaviour is a consequence of the small amplitude of the transient signal in this part of the detector. At mid radii, the contribution to the transient charge due to the electrons and to the holes are nearly equal and they effectively cancel out. In slice A, due to the different electric field distribution and, therefore, the different trajectories that electrons and holes have to travel (see Fig. 2.13), such compensation is not observed.

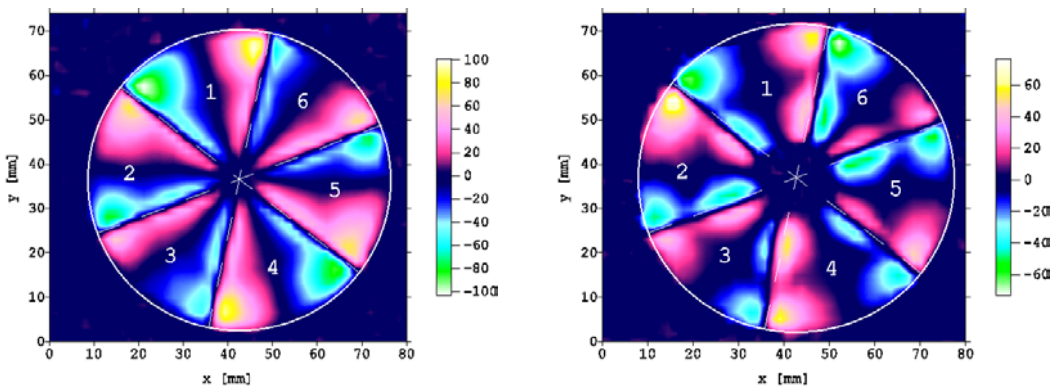


Figure 5.35: Polar plot showing the asymmetry distributions as a function of the position of the collimator, measured for slice A (left) and C (right).

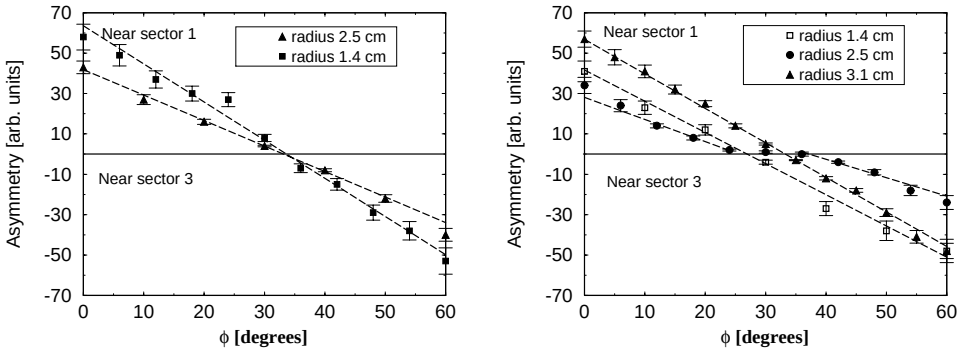


Figure 5.36: Asymmetry values as a function of the azimuthal angle $\phi$ of the interaction, measured on contact A2 at two different radii, namely 1.4 cm and 2.5 cm (left), and C2 at three different radii, namely 1.4 cm, 2.5 cm and 3.1 cm (right). The angle $\phi$ is 0° at the boundary between sector one and sector two, 60° at the boundary between sector two and three.

In Fig. 5.36 the asymmetry values are plotted as a function of the azimuthal angle $\phi$ of the interaction. The asymmetry was measured from contact A2, at two different radii (1.4 cm and 2.5 cm), and C2, at three different radii (1.4 cm, 2.5 cm and 3.1 cm). In the case of segment A2, a linear relationship between the asymmetry and the azimuthal position of the interaction is evident both at a radial distance of 1.4 cm and at a radial distance of 2.5 cm. In the case of segment C3, the relationship is linear at 1.4 cm and at 3.1 cm, while at 2.5 cm, i.e. at mid radii, it shows a plateau between 24° and 46°, where it is virtually equal to zero. This means that, at this radial distance and in this angular window the transient charge signals cannot provide useful information for position determination. In order to extract quantitative information from this linear dependence, the data have been fitted to straight lines (see equations 5.19, 5.20, 5.21 and 5.22, where $y_i$ is the measured asymmetry and $x_i$ is the angles $\phi$). The same assumptions discussed for the fit of rise time as a function of the radial position are still valid. In the case of the data from segment C2 measured at a radius of 25 mm, two different lines have been fitted to the data, one before and one after the plateau at zero. The results are reported in Tab. 5.3.

Considering equation 5.2, the error of the asymmetry is due to the uncertainty associated

| Fit for | $a$ [FADCu/deg.] | $\sigma_a$ [FADCu/deg.] | $b$ [FADCu] | $\sigma_b$ [FADCu] | $\sigma_y$ [FADCu] | $\chi^2$ |
|---|---|---|---|---|---|---|
| Contact C2 | | | | | | |
| 14 mm | -1.55 | 0.09 | 41 | 2 | 3.86 | 1.21 |
| 25 mm ($\phi$ <24°) | -1.09 | 0.07 | 28 | 1 | 3.75 | 1.35 |
| 25 mm ($\phi$ >36°) | -0.91 | 0.09 | 34 | 4 | 2.50 | 1.32 |
| 31 mm | -1.71 | 0.03 | 57 | 1 | 2.58 | 1.05 |
| Contact A2 | | | | | | |
| 14 mm | -1.26 | 0.04 | 42 | 1 | 2.98 | 1.17 |
| 25 mm | -1.89 | 0.08 | 64 | 2 | 4.17 | 1.17 |

Table 5.3: Asymmetry versus angular position of the interaction. The parameters extracted from the outer contacts C2 and A2 are here reported. The notation FADCu stands for the FADC arbitrary units.

with the measurements of the magnitude of the transient charge pulses. This uncertainty

arises from the noise fluctuations in the baseline and was estimated to be 25 FADC arbitrary units (recalling section 4.1.3, the peak-to-peak noise oscillations are ∼12.5 mV, after a factor 5 amplification, and the FADC gain is equal to 0.5 mV/unit), as shown in Fig. 4.19. This means that image charge amplitude smaller than 25 FADC units cannot be distinguished above the noise level. To be precise, the error of the asymmetry should be calculated as:

$$\sigma_{Asym} = \sqrt{\sigma^2_{A_{left}} + \sigma^2_{A_{right}}} = \sigma_A\sqrt{2}, \tag{5.23}$$

assuming $\sigma_{A_{left}}$=$\sigma_{A_{right}}$=$\sigma_A$. This would result in a $\sigma_{Asym}$ of 35 arbitrary units. The value of $\sigma_y$ calculated following the fit, as reported in Tab. 5.3, are ten times smaller than the estimate obtained for each individual data point. This result, again, demonstrates the need to utilise the average information carried by all the pulse shapes corresponding to a given position for calibrating the response function of the detector. The results reported in Tab. 5.3 show that the slope of the fit and the accuracy in determining the angle $\phi$ are radially dependent. The errors on the angle (calculated from equation 5.22), which represent an estimate of the azimuthal position resolution, vary between 1.6° and 2.0° at a radial distance of 31 mm, between 2.6° and 4.5° at a radial distance of 14 mm and between 3.7° and 8.3° at a radial distance of 25 mm, this last being the worse case scenario. The magnitude of the gradient of the fit to asymmetry at different radii strongly effects the azimuthal position resolution. Therefore at large radii this technique provide superior information. It has to be pointed out that, at the radial distance of 25 mm and in the angular window of 22° in the middle of the segment, it is not possible to determine the angle $\phi$ of the interaction.

Some examples of the achievable position resolution at three given radial distances are presented in Tab. 5.4. It can be concluded that the radial position information provided by the T90-T30 method in conjunction with the linear and unambiguous dependence of the asymmetry as a function of $\phi$ enables one to reconstruct the 2D-position of the interaction.

**Effective granularity of the detector**

The effective granularity of a segmented detector is defined as the number of unique positions that can be identified within the detector volume; it is given by the number of segments times the number of unique positions which can be distinguished within the same segment. In the previous sections the position resolution of the detector has been calculated and it has

| r [mm] | $\Delta r$ [mm] | $\phi$ [deg.] | $\Delta\phi$ [deg] | $\Delta\phi$ [mm] |
|---|---|---|---|---|
| 14.0 | 2.7 | 5° | 2.6° | 0.63 |
| | | 20° | 3.2° | 0.77 |
| | | 55° | 4.1° | 0.97 |
| 25.0 | 0.9 | 5° | 3.7° | 1.60 |
| | | 20° | 4.0° | 1.76 |
| | | 55° | 7.6° | 3.31 |
| 31.0 | 1.1 | 5° | 1.6° | 0.86 |
| | | 20° | 1.7° | 0.92 |
| | | 55° | 2.2° | 1.19 |

Table 5.4: 2D-position resolution values, calculated at the radial distances of 14 mm, 25 mm and 31 mm. The radial position resolution ($\Delta r$) correspond to the uncertainty on the radial position determination, while the angular position resolution ($\Delta\phi$) corresponds to the uncertainty on the angular position determination. The results for the angular position resolution are presented both in degrees and in millimeters.

been demonstrated that this resolution varies over the detector volume. This information will be used to estimate the effective granularity of TIGRE.

Fig. 5.37 shows a segment of the detector, whose volume has been divided into five parts, which have different position resolution. The position resolution of each part has been estimated on the basis of the above discussion: (1) for radii between 4 mm and 16 mm the radial position resolution is $\sim$2 mm and the angular position resolution is $\sim$4°, (2) for radii between 16 mm and 26 mm the radial position resolution is $\sim$3 mm and the angular position resolution is $\sim$8°, outside the sector of 22°, in which the angular position information is missing, (3) for radii between 26 mm and 32 mm the radial position resolution is $\sim$1 mm and the angular position resolution is $\sim$2°. This means that a total of 290 unique positions can be distinguished within a sector in the true coaxial part of the detector.

By extending the validity of this method to the other segments in the coaxial part of the detector, a total of 290$\times$12=3480 positions can be distinguished. The additional information on the depth of the interaction, provided by the magnitude of the transient charge signals along the z-direction, enables, conservatively, this number to be doubled. The analysis performed so far has been restricted to the coaxial part of the detector, there-

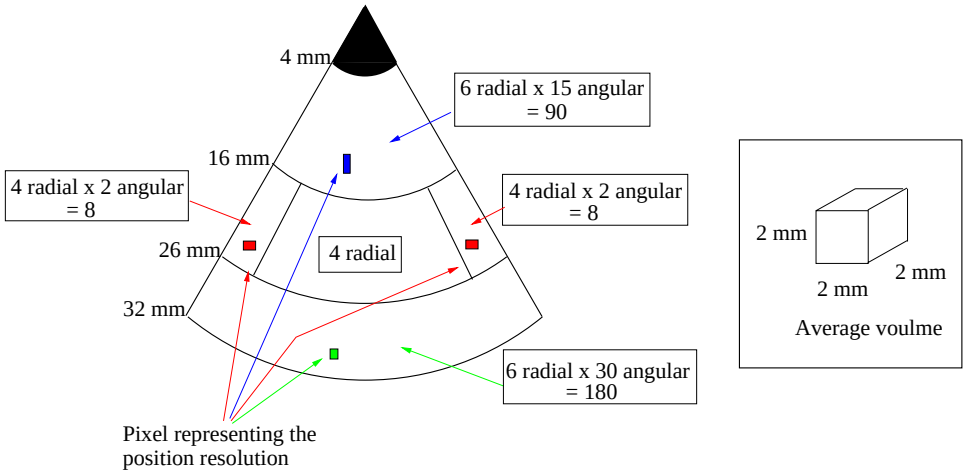


Figure 5.37: A qualitative indication of the achievable position resolution. The pixels show, at each given position, the uncertainty in the 2D-position determination. By performing pulse shape analysis, ∼290 unique positions can be distinguished. The cube on the right part gives an indication of the average position resolution. The figures are not in scale.

fore, no conclusions can be drawn on the closed-ended and on the back part of the detector. An estimate of the effective granularity of the TIGRE detector in the true coaxial region is:

$$G_{eff} \geq [(3480 \times 2)] = 6960. \tag{5.24}$$

From this result, the average size of a cube representing the volume in which the position of the interaction can be resolved (i.e. the 3D-position resolution) has been qualitatively estimated. According to the azimuthal position information obtained from the analysis of the transient charge signals, it should be possible to identify at least four unique positions along the depth of the detector. In this assumption, an effective granularity of 13920 is obtained. This means that a cube of dimension $\sim 2 \times 2 \times 2$ mm$^3$ can be identified.

In order to provide qualitative visual evidence of the feasibility of the method, 2D-matrices have been produced at the nine positions of the collimator sketched in Fig. 5.38. The analysis has been restricted to fold-1 full energy events occurring in segment B2 and C2. Nine 2D-matrices were produced by plotting, for all the pulse shapes corresponding to each given position, the time-to-maximum of the current pulses measured from the centre contact

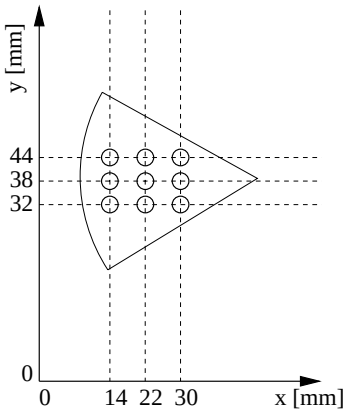


Figure 5.38: The nine collimator positions within sector two considered in the analysis.

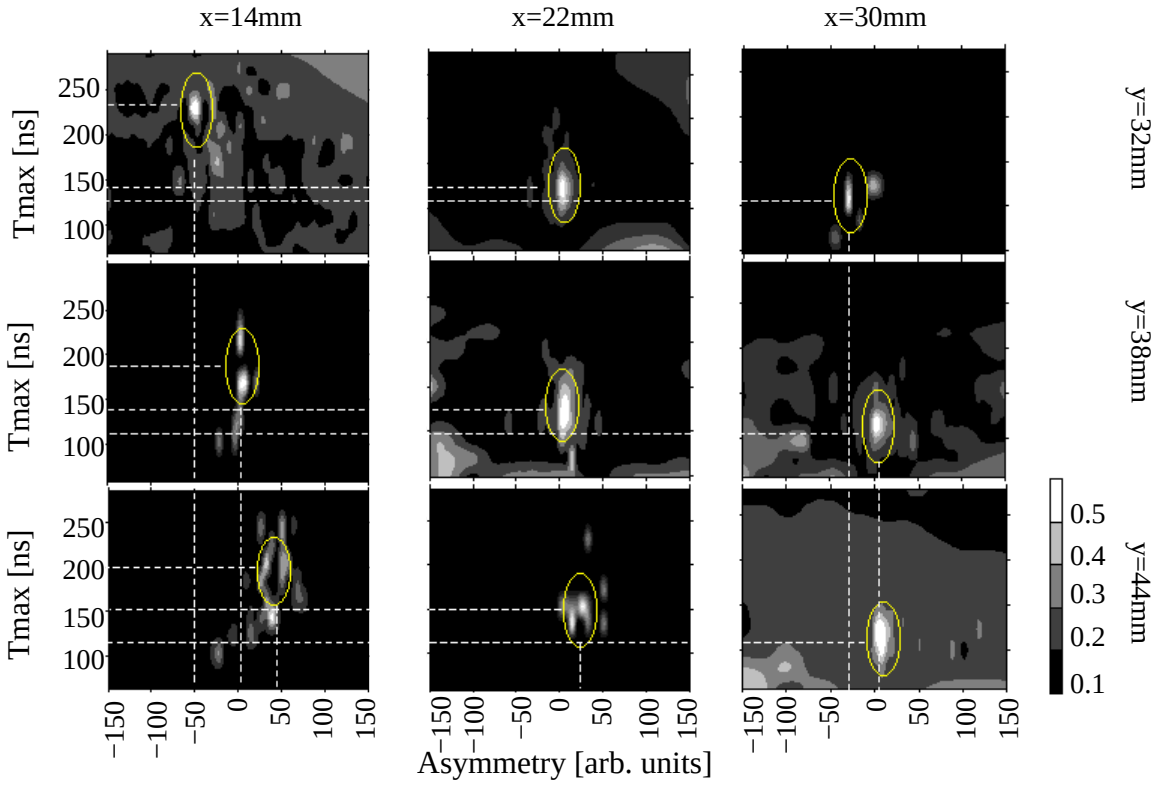


Figure 5.39: 2-dimensional position response of sector 2: the time-to-maximum of the current pulse is plotted against the asymmetry for the nine positions of Fig. 5.38. The spatial coordinates of each position are indicated on the top and on the right hand side of the graph. The highlighted areas indicate the general trend of the data.

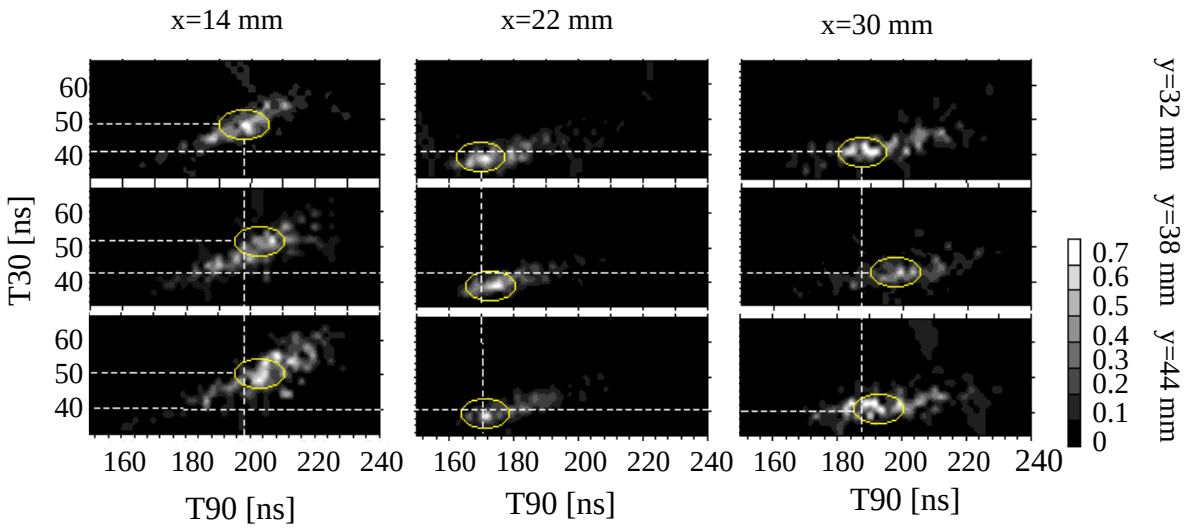


Figure 5.40: 2-dimensional position response of sector 2: the T30-time is plotted against the T90-time for the same nine positions of the scanning table. The spatial coordinates of each position are indicated on the top and on the right hand side of the graph. The spatial coordinates of each position are indicated on the top and on the right hand side of the graph. The highlighted areas indicate the general trend of the data.

against the asymmetry value. Results are presented in Fig. 5.39. The time-to-maximum, differently from the T90 time, increases monotonically as a function of the radial distance, therefore it enables the position to be unambiguously determined.

For each pulse shape, the 2D-position of the interaction arises from the position occupied by the $(Asym, T_{max})$ point on the 2D-plot. The average interaction position, which corresponds to the position of the collimator, is represented by the point on the plot with the largest number of counts. For each 2D-plot in Fig. 5.39, a circle of constant area has been drawn around the position, which is believed to represent the average interaction position. Indeed, the lack of a grouping procedure in incrementing the matrices results in very low statistics: the maximum channel contains only ∼10 counts.

A visual inspection of the plots shows evidence that the circle moves depending on the angular and radial position. In the representation of Fig. 5.39, the plots corresponding to x=14mm have the same $T_{max}$ (∼200 ns), being at nearly the same radial distance from the

centre, but very different $Asym$ (-50 for y=32 mm, 0 for y=38 mm and 50 for y=44 mm); for the same reason, the plots corresponding to x=22 mm have the same $T_{max}$ ($\sim$150 ns) but no useful information is contained in the $Asym$ (in the central part of the segment); the plots corresponding to x=30 mm have the same $T_{max}$ ($\sim$110 ns) and different $Asym$ (azimuthal position information is recovered at smaller radii).

Similar results are presented in Fig. 5.40, where the T30 time is plotted against the T90 time for charge pulses measured from the centre contact signal. The three plots corresponding to x=14 mm and the three plots corresponding to x=30 mm have all very similar T90 ($\sim$190 ns), being at two radial positions which are symmetrical with respect to the middle of the active volume, but have different T30 (T30 $\sim$50 ns for x=14 mm and T30 $\sim$40 for x=30 mm). The plots corresponding to x=22, instead, show a shorter T90 ($\sim$170 ns).

Although the plots of figures 5.40 and 5.39 show evidence of the relationship between the parameters extracted from the pulse shape and the position of the interaction, the above discussion is purely qualitative.

# Chapter 6

# Conclusions

The development of a new detection system is required in $\gamma$-ray spectroscopy experiments in order to study the structure of exotic nuclei produced in radioactive ion beam (RIB) reactions. This system will consist of many highly sensitive HPGe detectors, which will provide superior energy and position resolution. The new detection technique will be based on the concept of $\gamma$-ray tracking, requiring the use of digital signal processing electronics for the analysis of the preamplifier signals. In this work, the performance of a highly segmented HPGe detector has been characterised and a pulse shape analysis algorithm has been developed. The principal aim of the analysis was to determine experimentally the position resolution of the detector. This information is fundamental for the development of $\gamma$-ray tracking techniques.

The developed algorithm enables the response of the detector to be calibrated as a function of the interaction position. The algorithm is based on the analysis of the pulse shape leading edge and on the extraction of meaningful parameters, such as the T90 rise time, the T30 rise time and the asymmetry in the amplitude of transient charge signals. The T90 rise time has been used to extract the radial position of the interaction, with an ambiguity arising from a similar value given by interactions occurring at the two positions which are symmetric with respect to the centre of the segment. The T30 rise time has been used to resolve the ambiguity and to obtain a unique radial position determination. Once the radius is known, by choosing the appropriate fit from the asymmetry data, the azimuthal position of the interaction can be recovered.

The use of a collimation system precludes the calibration on an event-by-event basis

and requires an average to be made over a number of data points. This was achieved by extracting all the pulses stored at a given position, enabling the average position of the interaction (which corresponds to the collimator centre) to be reconstructed.

It has been demonstrated that pulse shape analysis techniques provide a powerful tool for position determination and that the response function of the detector depends on the position of the interaction. The position resolution ranges between 0.6 mm and 3 mm in radius, and between 2° and 8° in azimuthal angle. The position resolution achieved in the most sensitive part of the detector satisfies the requirement of 1 mm for efficient $\gamma$-ray tracking.

The effective granularity has been calculated for one segment in the true coaxial part of the detector. At least 580 unique positions could be unambiguously identified. Due to the cylindrically symmetric geometry of the detector, the results can be extended to all the segments in the coaxial part. This results in a total of 6960 distinguishable positions in the slices B and C. The results cannot be extended to the closed-ended and back parts of the detector (ring A and D) due to the difficulties arising from the complex electric field configurations.

The characteristics of the charge collection process in the coaxial and in the closed-ended part of the detector have been experimentally investigated. Evidence for an anisotropy in the drift velocity of the charge carriers, and the consequent crystallographic orientation effects, have been shown. The problems arising from the weak electric field in the closed-ended part of the detector can be reduced by over-biasing the detector, i.e. by the application of an increased high voltage. This will result in an improved electric field at the front corners and therefore result in better charge collection performance.

## 6.1 Future work

In order to calculate the 3D-position resolution of the detector, a scan should be performed along the length of the detector. The additional position information along the z-direction, in conjunction with the 2D-position information, would provide an appropriate number for the effective granularity of the detector.

In order to calibrate the detector response on an event-by-event basis, a coincident measurement needs to be performed [Vet00]. This measurement has the advantage of

providing precise position determination; however this is achieved with low statistics and requires very long measurement time.

An in-beam test of the TIGRE detector should be performed. The aim of the experiment would be to prove the feasibility of performing $\gamma$-ray tracking, by the capability of Doppler correction. From the Doppler correction of $\gamma$ rays emitted in flight, the accuracy in determining their entry point in the detector will be measured. This experiment was successfully performed with the MARS prototype detector [Krö02].

# Appendix A

# Monte Carlo simulation

In this work simulation calculations have been performed using the Monte Carlo codes MCNP [Mcn94] and GEANT 3.21 [Gea94]. This section concerns the results obtained using GEANT.

GEANT is a detector description and simulation tool, which simulates the passage of elementary particles through matter, enabling particle tracking to be performed. The simulation provides the energy and the coordinates of each individual interaction point, required by the absorption of a $\gamma$ ray in a solid medium.

The principal aim of the simulations was to investigate the theoretical response of the detector to a known incident $\gamma$-radiation field and to set an upper limit on the position resolution which can be achieved with the developed pulse shape analysis method. Information on the localisation of individual interaction events and comparison with experimental observables such as the number of segments firing (fold) and the peak-to-total ratio will be presented.

In the calculations, the geometry of the TIGRE detector has been considered. The bulletised corners at the front face and the hole for the centre contact have been included in the definition of the volume, while the effects of the boron and lithium contacts and of the aluminium can which hosts the crystal have been neglected. A picture of the simulated geometry is illustrated in Fig. A.1. The detector has been placed into a cubic vacuum volume where the transport of the radiation has been confined.

In order to reproduce the collimated radiation source utilised in this work (see section 4.1.3), an isotropic, mono-energetic source has been considered. The source was placed on the symmetry axis of the detector at a distance of 16 cm from the detector front face and

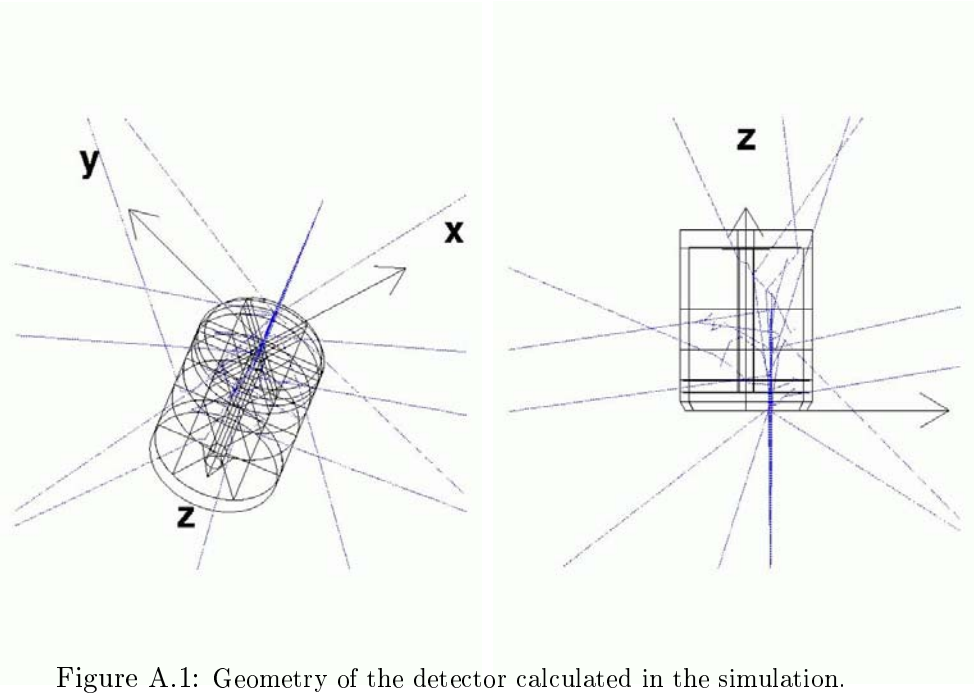


Figure A.1: Geometry of the detector calculated in the simulation.

the emitted photons have been focused into a cone of 2 mm diameter. Calculations have been carried out at different $\gamma$-ray energies, from 100 keV to 2 MeV. In order to ensure statistically significant results, a minimum of $10^5$ events has been considered in each run. The statistical uncertainty of the results is typically less than 10%.

## A.1 Characteristics of photon interaction

The interactions of primary interest for spectroscopic studies are $\gamma$ rays fully absorbed in the detector volume (photopeak events), therefore only these events will be considered in the analysis.

The fraction of photopeak events to the total number of events interacting in the detector has been calculated as a function of the $\gamma$-ray energy. Results are reported in Fig. A.2. As the $\gamma$-ray energy increases, the probability that a $\gamma$ ray will Compton scatter out of the detector increases and the number of $\gamma$ rays fully absorbed in the detector decreases. In the context of this work, at 662 keV approximately 32% of incident events are fully absorbed in the detector.

The number and the type of interactions leading to a photopeak event has been investigated as a function of the $\gamma$-ray energy. In figure A.3 the fraction of the possible

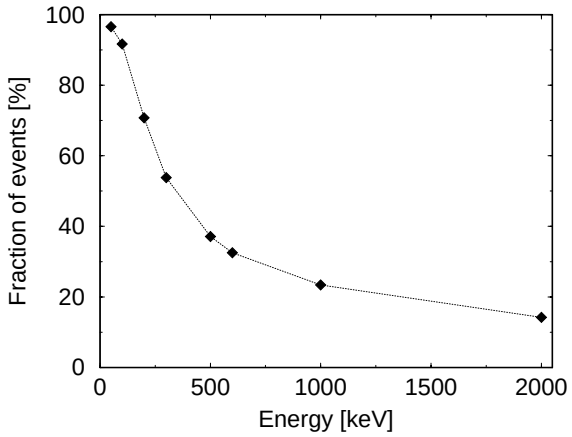


Figure A.2: Fraction of full energy events as a function of the $\gamma$-ray energy. Uncertainties in the measurements are statistical and typically $\leq$10%.

interaction chains is plotted as a function of the photon energy. At low energies, the interaction process mainly consists of a single photoelectric absorption at the first interaction point. The photoelectric effect is the dominant process until about 170 keV, at this energy a sharp transition between single and multiple events can be distinguished. At higher energies the photon absorption requires more than one interaction (between 3 and 4 at 1 MeV), typically a few Compton scatters followed by the final photoelectric absorption. At about 220 keV events which are single photoelectric, single Compton plus photoelectric and multiple Compton plus photoelectric have roughly the same strength. As the energy increases, multiple Compton events become most probable.

### A.1.1 Fold distributions

Since the number of interactions required by the absorption of a $\gamma$ ray varies depending on the $\gamma$-ray energy and the mean free path between interactions ranges from a few millimeters to a few centimeters, Compton scattering between adjacent segments in the TIGRE detector is very likely. Typically, a 662 keV $\gamma$ ray is absorbed in 2-3 interactions.

The number of segments that fire in coincidence is defined as the *fold*. The Monte Carlo code was used to produce a simulated fold distribution. The fold multiplicity depends on the number of interactions which each $\gamma$ ray undergoes, and hence on the $\gamma$-ray energy.

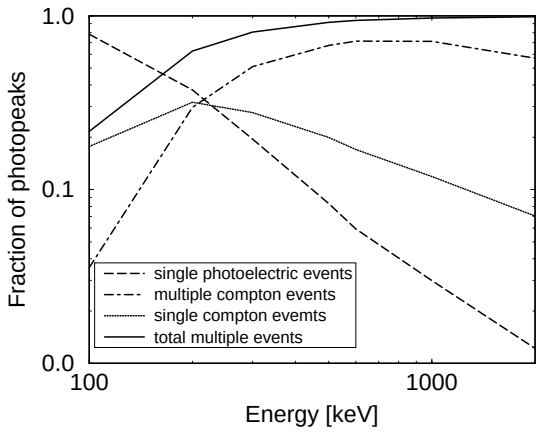


Figure A.3: Relative strength of possible interaction mechanisms leading to a full energy event in the TIGRE detector.

The results are displayed in figure A.4 at various energies for both photopeak and partially absorbed events. If all the events are considered, the dominant contribution to the fold distribution comes from fold-1 events, and for higher energies the contribution at higher fold increases. If only photopeak events are considered, the fold distribution above 500 keV consists mainly of fold-2 events. The ratio of fold-2 to fold-1 events increases as the energy increases. Even at very high energy, events with fold higher than four contribute less than 1% to the photopeak. For this reason, add-back events up to fold-4 can be considered significant.

### A.1.2 Energy distribution

In this section, the distribution of the event energy among the individual interactions will be discussed. The localization of the energy deposition allows a limit to be set on the position resolution which can be achieved utilising the developed pulse shape analysis method. In section 5.4 the concept of *first* and *main* interaction was introduced. Recalling the work of Palafox [Pal97], the following analysis is focused on understanding how well the coordinates of the first interaction point can be determined by measuring the position of the main interaction. This knowledge is necessary in order to reconstruct the entry point of the $\gamma$ ray and to enable a Doppler broadening correction to be performed. Strictly, only for $\gamma$-ray

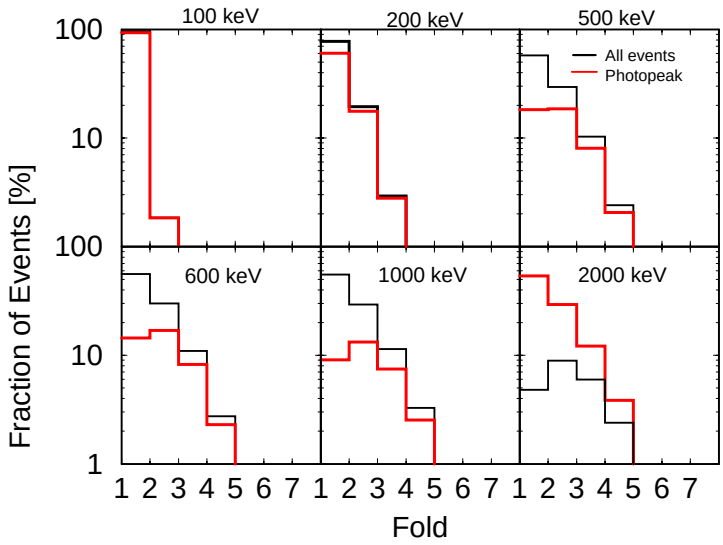


Figure A.4: Fold distribution at various $\gamma$-ray energies.

events, in which the first is also the main interaction, the entry point can be unambiguously determined.

Fig. A.5 shows the fraction of full energy events, where the first interaction is also the main interaction, plotted against the energy of the incident $\gamma$ ray. The definition of the scattering angle between the two interactions is shown in Fig. A.6. At low energy (100 keV), for most the events, the first interaction is also the main interaction, since the absorption of the $\gamma$ ray is dominated by the photoelectric effect. As the energy increases, the fraction of events where the first interaction is also the main one decreases; this is because the number of interactions required for the full absorption of the $\gamma$ ray increases and the energy can be spread over a larger number of interactions. Above 500 keV the fraction of such events starts increasing again; only events which deposit a large fraction of their energy in the first interaction would contribute to a full energy event.

If the first interaction is not the main interaction, the accuracy in the determination of the entry radius of the $\gamma$ ray is limited by the radial distance between the first and the main interaction. In figures A.7 and A.8, the average distance between the first and the main interaction and their angular separation are presented as a function of energy. Linear and angular distance show the same trend. The distance rises steeply with the energy, reaching

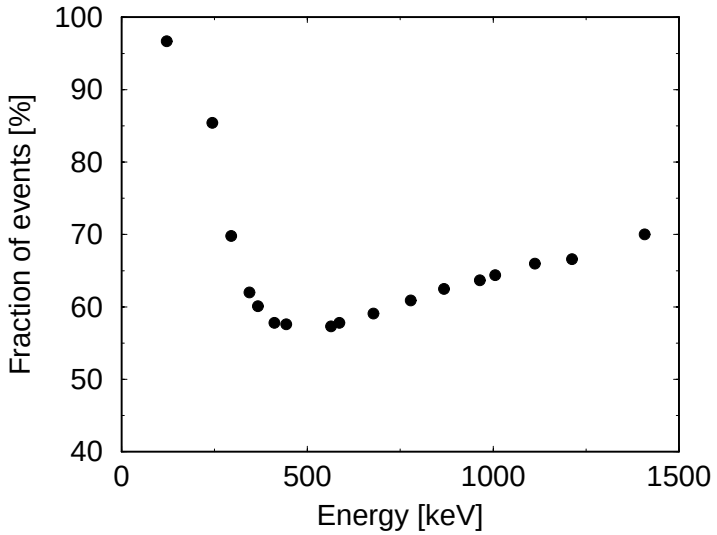


Figure A.5: The fraction of full energy events where the first interaction is also the main interaction is plotted versus the energy of the incident $\gamma$ ray.

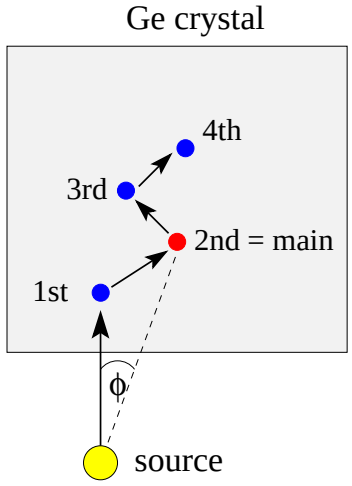


Figure A.6: Scattering path of a $\gamma$ ray inside the detector material, where the first interaction is not the main interaction.

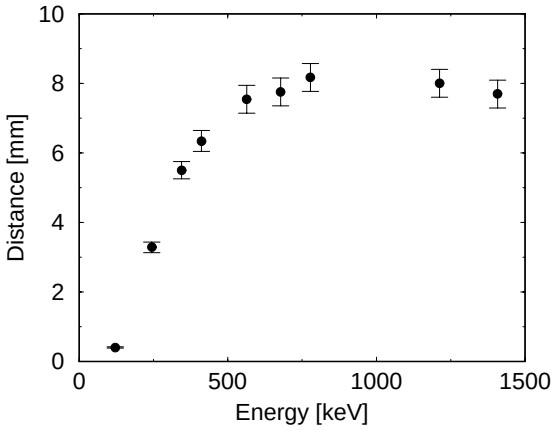


Figure A.7: Average distance between the first and main interaction for full energy events in which the first interaction is not the main interaction.

a plateau value of ∼8 mm linear and ∼12° angular, above 500 keV. This factor limits the position resolution which can be achieved if no $\gamma$-ray tracking is used to determine the scattering sequence of the $\gamma$ ray.

**Segment energy distributions**

The segment energy distribution across coincident segments has been investigated. The aim of the analysis was to determine a criterion, based on the observation of the energy distribution, which enables one to identify for multiple hit events the segment hosting the first interaction in order to perform a better Doppler broadening correction.

The fraction of events in which the first interaction segment (FIS) corresponds to the main interaction segment (MIS) has been calculated for fold-2, photopeak and partially absorbed events. The results shown in Fig. A.9 show that, as the energy increases, the fraction of events in which the FIS is also the MIS increases, and for energies above 500 keV the FIS is most likely to be the one with the greatest fraction of the initial $\gamma$-ray energy; above this energy the FIS corresponds to the MIS for about 80% of the photopeak events. The systematic difference, above 200 keV, between the fraction of photopeak and the fraction of partially absorbed events is due to the different efficiency in detecting high energy photons: at high energy, only events where one of the early Compton scattering releases a big fraction of the initial energy become full energy events.

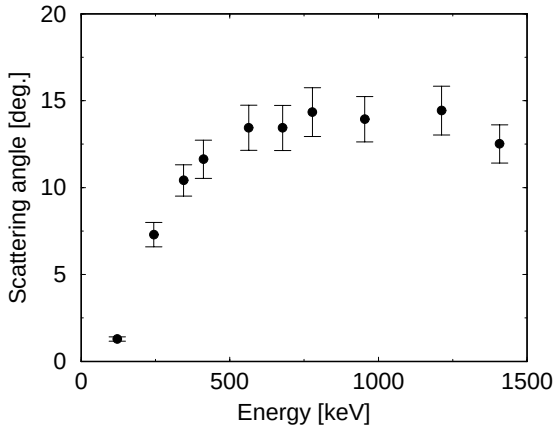


Figure A.8: The average angular separation between the first and main interaction, for full energy events in which the first interaction is not the main interactions. The angular separation was calculated by considering a source-detector distance of 16 cm.

| Ring | A | B | C | D |
|---|---|---|---|---|
| Fraction of first hit events [%] | 44 | 27 | 18 | 11 |

Table A.1: Fraction of events having the first interaction in a given slice.

It can be concluded that, for fold-2 events, at low energy (below 500 keV) the segment with the lowest energy is the FIS, at high energy (above 500 keV) the segment with the highest energy is the FIS and at intermediate energy (around 500 keV), due to the large distribution of the energy deposition, it is not possible to identify the FIS from the energy distribution.

Knowledge of the entry point of a $\gamma$-ray photon in the detector volume is required in order to calibrate the PSA algorithms. Following the first interaction $\gamma$ ray will scatter over a large angle $\phi$, leading to a loss of the known position information. Due to the good intrinsic electric field in slices B and C in the detector volume, the experimental calibration has been restricted to these slices. In order to predict the fraction of events with the first interaction in a given slice, a simulation has been carried out. The results are shown in Tab. A.1. It was concluded that the fraction of events having the first interaction in the coaxial part of the detector would have been statistically significant. This means that the

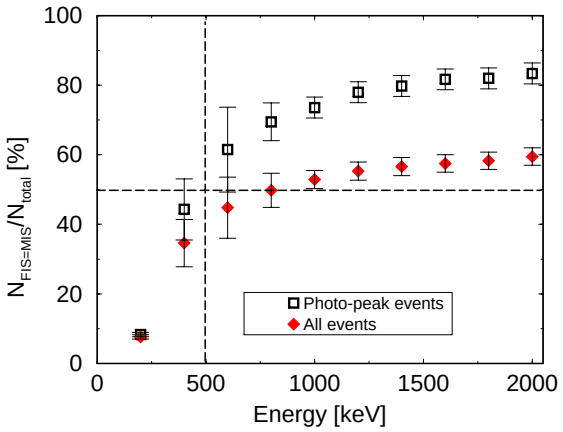


Figure A.9: Fraction of fold-2 events where the first hit segment is also the segment in which most of the initial $\gamma$-ray energy has been released. Both all events and only photopeak events have been considered.

developed pulse shape analysis algorithm could be tested on a significant sample of data.

## A.2 Comparison with the experimental measurements

In this section, the response of the TIGRE detector to collimated radiation will be investigated, by comparing simulated and experimental results. A source in the centre of sector one, at a distance of 8 cm, has been considered. The peak-to-total (P/T) has been defined *ad hoc* as the ratio of the events in the 662 keV channel to the total number of counts in the whole spectrum.

Hit pattern results are presented in Tab. A.2. The simulated and the measured values agree well (the maximum discrepancy is $\sim$2%) and show the same trend.

The fold distribution results are presented in Tab. A.3. The experimental and the simulated values show the same trend but a maximum discrepancy of $\sim$6%, arising from the fact that in the Monte Carlo calculation the electric field distribution was not considered. In the simulation, the fold distribution has also been obtained for all the events occurring in the detector, even if not fully absorbed. These results have not been compared with the experimental measurements because the experimental setup was not appropriate (the threshold for the data acquisition trigger was set just below the 662 keV $\gamma$-ray line). The

| Segment | Fraction of Events [%] | | Segment | Fraction of Events [%] | |
|---|---|---|---|---|---|
| | Simulated | Experimental | | Simulated | Experimental |
| A1 | 27.3 | 25.0 | C1 | 15.3 | 16.7 |
| A2 | 2.0 | 1.7 | C2 | 2.7 | 1.5 |
| A3 | 0.5 | 0.8 | C3 | 2.0 | 0.6 |
| A4 | 0.4 | 0.8 | C4 | 0.8 | 0.7 |
| A5 | 0.5 | 1.2 | C5 | 2.0 | 1.1 |
| A6 | 2.0 | 4.2 | C6 | 2.7 | 4.1 |
| B1 | 20.4 | 18.1 | D1 | 9.4 | 10.6 |
| B2 | 2.6 | 1.4 | D2 | 2.1 | 1.4 |
| B3 | 0.7 | 0.5 | D3 | 0.9 | 0.6 |
| B4 | 0.6 | 0.5 | D4 | 0.8 | 0.7 |
| B5 | 0.7 | 0.9 | D5 | 0.9 | 1.2 |
| B6 | 2.5 | 3.3 | D6 | 2.1 | 2.3 |

Table A.2: Hit pattern distribution at 662 keV.

fold distribution table shows that >70% of the fully absorbed events have triggered more than one segment, this means that a large fraction of photopeak events consists of scattered events between several segments.

In Tab. A.4 add-back results are presented for the sum of different contributions to the total fold. The experimental and theoretical spectra are shown in Fig. A.10. The results

| Fold | All events [% | Photo-peak events [%] | |
|---|---|---|---|
| | Simulated | Simulated | Experimental |
| 1 | 48.7 | 33.8 | 28.9 |
| 2 | 34.0 | 39.4 | 33.8 |
| 3 | 13.3 | 19.9 | 21.2 |
| 4 | 3.4 | 5.7 | 10.3 |
| 5 | 0.6 | 1.0 | 4.0 |
| 6 | 0.06 | 0.1 | 1.2 |

Table A.3: Fold distribution at 662 keV.

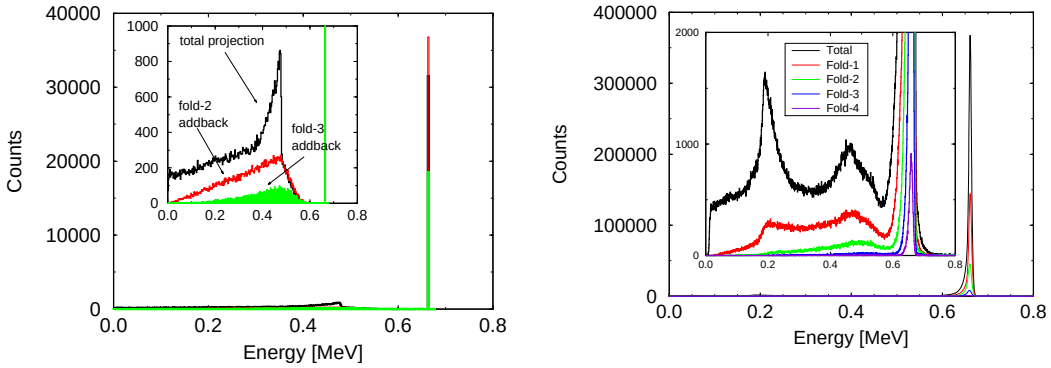


Figure A.10: Simulated (left) and experimental (right) add-back spectra for different fold activated.

manifest typical behaviour for add-back spectra, with very few counts at low energy where Compton scattering is not important.

From these results it can be concluded that a large improvement in the peak-to-total ratio

| Fold | P/T [%] | | Peak counts | |
|---|---|---|---|---|
| | Simulated | Experimental | Simulated | Experimental |
| 1 | 34 | 45 | 31525 | 1032342 |
| 2 | 57 | 59 | 36774 | 1338307 |
| 3 | 73 | 73 | 18516 | 612691 |
| 4 | 83 | 83 | 5368 | 142387 |
| 5 | 89 | 89 | 959 | 18757 |

Table A.4: Peak-to-total ratio for different fold activated. Fold one event corresponds to the energy spectrum in all the germanium crystal if only one contact is involved in the $\gamma$-ray event, while fold two (three, etc.) corresponds to the energy spectrum recovered by adding-back the two (three, etc.) partial energies deposited in the segments involved in the $\gamma$-ray event.

is obtained by summing the energy deposited in coincident segments and that up to four segments should be considered in the add-back spectrum.

# References


[Aga01] J. Gerl and W. Korten, Technical Proposal for *An Advanced Gamma Tracking Array for the European Gamma Spectroscopy Community* (2001).

[Baz92] D. Bazzacco, Proc. Workshop on Large Gamma-Ray Detector Arrays (Chalk River, Ontario, Canada) AECL 10613 (1992), 376.

[Baz99] D. Bazzacco *et al.*, LNL Annual Report 1999, *Test of the MARS prototype segmented germanium detector*, INFN and Dipartimento di Fisica, Padova, Italy.
web page:$http://axpd30.pd.infn.it/MARS$.

[Baz00] D. Bazzacco, Talk given at the TMR user Meeting (Cologne, Germany) June 2000.

[Bea92] C.W. Beausang *et al.*, Nucl. Instr. Meth. A313 (1992) 37.

[Bea96] C.W. Beausang and J. Simpson, J. Phys. G: Nucl. Part. Phys. 22 (1996) 527-558.

[Bec92] F.A. Beck, Prog. Part. Nucl. Phys. 28 (1992) 443.

[Bec93] F.A. Beck *et al.*, Nucl. Phys. A557 (1993) 67c.

[Ber02] *Opportunities in nuclear science, a long-range plan for the next decade*, document produced by the Berkeley Lab Technical and Electronic Information Department in collaboration with the Nuclear Science Advisory Committee (2002).

[Bra91] G.J. Bramford, IEEE Trans. Nucl. Sci., Vol. 38, No. 2 (1991) 200.

[Bro02] B.A. Brown *et al.*, Phys. Rev. C 65 (2002) 045802-1.

[Bri75] F. Briggs *et al.*, Atomic Data Nuclear Data Tables 16 (1975) 201.

[Can74] C. Canali *et al.*, Solid State Comm. 15 (1974) 1213.

[Can77] L. Reggiani *et al.*, Phys. Rev. 16B (1977) 2781.

[CAS] SIRIUS Web page: *http* : *//www.dl.ac.uk/NPG/sirius.html*.

[Dab89] W. Dabrowski, Prog. Quant. Electr. 13, (1989) 233-266.

[Davi98] C.N. Davids, Phys. Rev. Lett. 80 (1998) 1849.

[Dav68] C.M. Davisson, Interaction of Gamma Radiation with Matter in *Alpha-, Beta- and Gamma ray Spectroscopy* , ed. by K. Siegbahn, North-Holland, Amsterdam (1968).

[Del88] M.A. Delaplanque and R.M. Diamond, Gammasphere Proposal *A National Gamma-ray Facility* (1988).

[Del99] M.A. Delaplanque *et al.*, Nucl. Instr. Meth. A430 (1999) 292-310.
Web page: *http* : *//greta.lbl.gov*.

[Des70] R.Y. Deshpande, Nucl. Instr. Meth. 82 (1970) 51.

[Dia84] R.M. Diamond and F.S.Stephens, Proc. Conf. on Instrumentation for Heavy Ion Nuclear Research, ed. D. Shapira: Vol.7 in the Nucl. Sci. Research Conf. Series (Harwood, New York) 1984, 259.

[Dob96] J. Dobaczewsky *et al.*, Phys. Rev. C53, (1996) 2809.

[Dob02] J. Dobaczewsky, Web page: *http* : *//www.fuw.edu.pl/ dobaczew*.

[Duc92] G. Duchêne *et al.*, Proc. Workshop on Large Gamma-Ray Detector Arrays (Chalk River, Ontario, Canada) AECL 10613 (1992), 359-364.

[Duc99] G. Duchêne *et al.*, Nucl. Instr. Meth. A432 (1999) 90-110.

[Ebe92] J. Eberth *et al.*, Prog. Part. Nucl. Phys. 28 (1992) 495.

[Ebe96] J. Eberth *et al.*, Nucl. Instr. Meth. A369 (1996) 135.

[Ebe97] J. Eberth *et al.*, Prog. Part. Nucl. Phys. 38 (1997) 29-37.

[Ebe00] J. Eberth, Talk given at the 22nd International School of Nuclear Physics (2000) Erice, Trapani, Sicily .

[Fan47] U. Fano, Phys. Rev. 72, 26 (1947).

[Fra96] G. de France *et al.*, Phys. Rev. C 53 (1996) R1070.

[Frau01] S. Frauendorf, Rev. Mod. Phys. 73 (2001) 463.

[Gas80] W. Gast *et al.*, Nucl. Instrum. Meth. A171 (1980) 49.

[Gat82] E. Gatti *et al.*, Nucl. Instr. Meth. 193 (1982) 651-653.

[Gat01] E. Gatti *et al.*, Nucl. Instr. Meth. A458 (2001) 738-744.

[Gea94] GEANT Detector Description and Simulation Tool, CERN Program Library, W5013, 1994.

[GER] web page: *http* : *//www.chemicalelements.com*

[Geo93] A. Georgiev and W. Gast, IEEE Trans. Nucl. Sci., Vol. NS-40 (1993) 770.

[Ger92] J. Gerl and R.M. Lieder, Euroball III GSI Darmstadt Report (1992).

[Gil98] G. Gilmore and J. Hemingway, Practical Gamma-ray spectrometry, John Wiley & Sons (1998), 220.

[Gla98] T. Glasmacher, Annu. Rev. Nucl. Part. Sci 48 (1998) 1.

[Gou72] F.S. Goulding, Nucl. Instr. Meth. 100 (1972) 493-504.

[Gou82] F.S. Goulding and D.A. Landis, IEEE Trans. Nucl. Sci. NS-29, 3 (1982) 1125-1140.

[GRE] GRETA Web page: *greta.lbl.gov* and reference therein.

[GRE00] Proposal for a Greta module cluster, Nuclear Science Division, Lawrence Berkeley National Laboratory (2000), 45.

[GSI] GSI Web page: *http://www-aix.gsi.de/GSI-Future/project/*.

[Hao90] J. Haoquiang, Program EFFIC-NEW manual, *A routine to automate peak-fitting, energy calibration, and efficiency calibration*, 1990.

[Has97] D.S. Haslip *et al.*, Phys. Rev. Lett. 78 (1997) 3447.

[Her85] B. Herskind *et al.*, Nucl. Phys. A447 (1985) 353c.

[Hert00] R-D. Herzberg, private communication.

[Hub99] B. Hubbard-Nelson *et al.*, Nucl. Instrum. Meth. A422 (1999) 411.

[Iba95] H. Ibach and H. Lüth, Solid-State Physics, Springer-Verlag, Second Edition (1995).

[Iba95a] H. Ibach and H. Lüth, Solid-State Physics, Springer-Verlag, Second Edition (1995), 332ff.

[Iba95b] H. Ibach and H. Lüth, Solid-State Physics, Springer-Verlag, Second Edition (1995), 349.

[Iba95c] H. Ibach and H. Lüth, Solid-State Physics, Springer-Verlag, Second Edition (1995), 344.

[Iba95d] H. Ibach and H. Lüth, Solid-State Physics, Springer-Verlag, Second Edition (1995), 330.

[Inn00a] The *M6x/cM6X* Development Package Manual, Innovative Integration, (2000). Web page: *http://www.innovative-dsp.com*.

[Inn00b] Innovative Integration, OMNIBUS User's Manual (2000). Web page: *http://www.innovative-dsp.com*.

[Jac81] C. Jacoboni *et al.*, Phys. Rev. B24 (1981) 1014-1026.

[Jac83] C. Jacoboni and L. Reggiani, Rev. Mod. Phys. 55 (1983) 645.

[Joe02] Joerger Enterprises MODEL VTR10012 Manual, JOERGER ENTERPRISES, INC. (New York, USA) 2002. Web page: *http://www.joergerinc.com*.

[Kel01] N.S. Kelsall, Phys. Rev. C64 (2001) 024309-1.

[Kes01] O. Kester *et al.* in Proceedings of the 2001 PArticle Accellerator Conference, *Commissioning of the REX-ISOLDE LINAC*, Chicago, USA, 2001.
Web page: $http://isolde.web.cern.ch/ISOLDE/$.

[Kno00] G.F. Knoll, Radiation detection and measurement, John Wiley & Sons, tird edition (2000).

[Kno00a] G.F. Knoll, Radiation detection and measurement, John Wiley & Sons, tird edition (2000) 411.

[Kno00b] G.F. Knoll, Radiation detection and measurement, John Wiley & Sons, tird edition (2000) 611.

[Kno00c] G.F. Knoll, Radiation detection and measurement, John Wiley & Sons, tird edition (2000) 51.

[Kno00d] G.F. Knoll, Radiation detection and measurement, John Wiley & Sons, tird edition (2000) 666.

[Kor02] A. Korichi, Journal of Nuclear and Radiochemical Science, Vol. 3 (2002) 213-215.

[Kra88] K.S. Krane, Introductory Nuclear Physics, John Wiley & Sons, (1988) 388.

[Krö01] Th. Kröll and D. Bazzacco, Nucl. Instrum. Meth. A463 (2001) 227-249.

[Krö02] Th. Kröll *et al.*, *Gamma-ray tracking with the MARS detector.*, Proc. Conf on Nuclear Structure with large $\gamma$-arrays, Padova, Italy, Sept 2002.

[Kos99] M.J. Koskelo *et al.*, Nucl. Instr. and Meth. A422 (1999) 373-378.

[Laz01] Web page: $http;//npg.dl.ac.uk/documentation/AGATA/electronics$.
Web page: $http://npg.dl.ac.uk/GRT/whydpp.htm$.

[Lee90] I.Y. Lee, Nucl. Phys. A520 (1990) 641c.

[Lee99] I.Y. Lee, Nucl. Instr. and Meth. A422 (1999) 195.

[Lee02] I.Y. Lee, Proc. Conference on Frontiers on Nuclear Structure (Clark Kerr Campus, UC Berkeley, CA) LBNL-50598 Abs. (2002) 134.

[Leo93] William R. Leo, Techniques for Nuclear and Particle Physics Experiments, Second Revised Edition, Springer-Veralg (1993).

[Leo93a] William R. Leo, Techniques for Nuclear and Particle Physics Experiments, Second Edition, Springer-Veralg (1993), 56 cc.

[Leo93b] William R. Leo, Techniques for Nuclear and Particle Physics Experiments, Second Edition, Springer-Veralg (1993), 37 cc.

[Lie97] M. Lieuvin and the SPIRAL group, *The commissioning of SPIRAL*, GANIL, Caen, France, 1997.
Web page: $http// : www.ganil.fr/spiral/$.

[Lie97] R. Lieder, Experimental Techniques in Nuclear Physics, ed. D.N. Poenaru and W. Greiner, W. de Gruyter Berlin, 137 (1997).

[Lis00] C. Lister *et al.*, *Development of HpGeDSSD Planar Detectors for the Gamma-Ray Box (GARBO)* ,Physics Division Annual Report ANL-01/19, 2000.

[Lop96] A. Lopez-Martens *et al.*, Phys. Lett. B 380 (1996) 18.

[Lor94] S. Ciampolillo and M. Loreti, *Introduzione alle Esperimentazioni di Fisica I, Teoria degli errori e analisi dei dati*, Quarta edizione, Edizioni Libreria Progetto, Padova 1994.

[Mac94] A.O. Macchiavelli *et al.*, Proc. Conf. on Physics from Large $\gamma$-ray Detector arrays (Berkeley, CA) LBL 35687, CONF 940888, UC 413 (1994) 149.

[Mai99] M.R. Maier *et al.*, Measurements of the energy and time response of a highly segmented coaxial germanium detector to gammarays: test of the GRETA prototype, submitted to the Proceedings of the IEEE symposyum on Nuclear Science, Seattle, Oct 1999.

[Mark01] K. Markenroth, Explorin the Exotic, Experimental investigation far from stability, Ph.D. Thesis, Chalmers University of Technology, Göteborg, Sweden (2001).

[Mart69] M. Martini and G. Ottaviani, Nucl. Instr. Meth. 67 (1969) 177-178.

[Mar99] J. van der Marel and B. Cederwall, Nucl. Instrum Meth. A437 (1999) 538-551.

[Mcn94] MCNP User Manual, A General Monte Carlo N-Particles Transport Code, version 4A, Judith F. Briesmeister Editor, October 1994.

[Mih00] L. Mihailescu *et al.*, Nucl. Instr. Meth. A447 (2000) 350.

[Mih00b] L. Mihailescu, Principles and methods for $\gamma$-ray tracking with large volume germanium detectors, Ph.D. Thesis, Forschungszentrum Juelich, Nov 2000.

[MSU] NSCL Web page: *http* : *//www.nscl.msu.edu/*.

[Mue00] W.F. Mueller, *Thirty-two-fold segmentes germanium detector to identify gamma rays from intermediate-energy exotic beams (2000)*, to be published .

[Muk76] T. Mukoyama, Nucl. Instr. Meth. 134 (1976) 125-127.

[Nat63] M.I. Nathan, Phys. Rev. 130 (1963) 2201.

[Nol79] P.J. Nolan and J.F. Sharpey-Schafer, Rep. Prog. Phys 42 (1979) 1.

[Nol85a] P.J. Nolan *et al.*, Nucl. Instr. Meth. A236 (1985) 95.

[Nol85b] P.J. Nolan *et al.*, J. Phys. G11, L17 (1985).

[Nol94a] P.J. Nolan, Annu. Rev. Part. Sci. 45 (1994) 561-607.

[Nol94b] P.J. Nolan *et al.*, Ann. Rev. Nucl. Part. Sci. 44 (1994) 561.

[ORN] HRIBF Web page: *http* : *//www.phy.ornl.gov/hribf/*.

[Ott75] G. Ottaviani *et al.*, IEEE Trans. on Nucl. Sci. NS-22 (1975) 192.

[Pal97] L. Palafox Gamir, *A new method for the determination of the entry position of $\gamma$-rays in high purity germanium detectors by current pulse analysis*, Ph.D. Thesis, Cranfiel University, College of Aereonautics (1997).

[Par00] Parker Automation Catalog 8081/USA (2000), 401/402XR Mini-Positioning Tables.
website: *http : //www.parker − emd.com.*
PDFX Series Ministep Drive User Guide, Electromechanical Division of Parker Hannifin plc, 2000.

[Pas96] A. Pascolini, *Lezioni di metodi matematici della fisica*, ed. Libreria Progetto, Padova 1996.

[Pasi01] M. Pasini and R.E. Laxdal, TIUMF design note TRI-DN-01-08, *ISAC-II: Beam Studies with Multi-charge Beams*, Vancouver, 2001.

[Pea01] C.J. Pearson *et al.*, to be published in IEEE Trans. Nucl. Sci. (2001).

[Pei92] A. Peisert, INFN report on Silicon microstrip detectors (1992).

[Pei92a] A. Peisert, INFN report on Silicon microstrip detectors (1992) 28.

[Poi99] R.L. Poirier *et al.* in Proceedings of the 1999 Particle Accellerator Conference,*RF system of the TRIUMF ISAC facility*, New York, 1999.

[Pre99] W.H. Press et al., Numerical Recipes in C, The Art of Scientific Computing, Cambridge University Press (1999) Second Edition, 549.

[Rad88] V. Radeka, Ann. Rev. Nucl. Part. Sci. 38 (1988) 217-277.

[Rad88a] V. Radeka, Ann. Rev. Nucl. Part. Sci. 38 (1988) 224.

[Ram39] Ramo, P.I.R.E. 27 (1939) 584.

[Reg78] L. Reggiani, Phys. Rev. 17B (1978) 2800.

[RIA] RIA Web page: *http : //www.phy.anl.gov.ria/.*

[Ros93] C. Rossi-Alvarez, Nucl. Phys. News Europe 3 (1993) 10.

[Rot84] J. Roth *et al.*, IEEE Trans. on Nucl. Sci., Vol. NS-31, No 1 (1984) 367.

[Sam00] J. Sampson, MTsort Language, Edition 2.20 (2000),
Web page: *http : //nnsa.dl.ac.uk/MIDAS/manual.*

[Sas56] W. Sasaki and M. Shibuya, J. Phys. Soc. Japan 11 (1956) 1202.

[Sas58] W. Sasaki *et al.*, J. Phys. Soc. Japan 13 (1958) 456.

[Sat01] W. Satula and R. Wyss, Phys. Rev. Lett. 86 (2001) 4488.

[Schl94] B. Schlitt *et al.*, Nucl. Instr. and Meth. A337 (1994) 416-426.
P.M. Jones *et al.*, Nucl. Instr. and Meth. A362 (1995) 556-560.

[Sch98] G.J. Schmid *et al.*, Nucl. Instr. Meth. A417 (1998), 95-110.

[Sch99] G.J. Schmid *et al.*, Nucl. Instr. Meth. A430 (1999), 68-83.

[She74] I.S. Shermann and M.G. Strauss, Nucl. Instr. Meth. 117 (1774) 285-294.

[Shep99] S.L. Shepherd *et al.*, Nucl. Instr. Meth. A434 (1999) 373-386.

[Shi55] M. Shibuya, Phys. Rev. 99 (1955) 1189.

[Sim97] J. Simpson, Z. Phys A358 (1997) 139.

[Sim00] J. Simpson *et al.*, APH N.S. Heavy Ion Physics 11 (2000) 159.

[Sin01] J. Singh, Semiconductor Devices Basic Principles, John Wiley & Sons, tird edition (2001) 63.

[Sme99] M.H. Smedberg *et al.*, Phys. Lett. B 452 (1999) 1-7.

[Str72] M.G. Strauss and I.S. Shermann, IEEE Trans. on Nucl. Sci. Vol. 19, No. 3 (1972) 219-225.

[Sze95] Simon M. Sze, Dispositivi a semiconduttore, comportamento fisico e tecnologia, Ed. Ulrico Hoepli, Milano, $4^a$ ristampa (1995).

[Sze95a] Simon M. Sze, Dispositivi a semiconduttore, comportamento fisico e tecnologia, Ed. Ulrico Hoepli, Milano, $4^a$ ristampa (1995) 98ff.

[Sze95b] Simon M. Sze, Dispositivi a semiconduttore, comportamento fisico e tecnologia, Ed. Ulrico Hoepli, Milano, $4^a$ ristampa (1995) 88.

[Sze95c] Simon M. Sze, Dispositivi a semiconduttore, comportamento fisico e tecnologia, Ed. Ulrico Hoepli, Milano, $4^a$ ristampa (1995) 57.

[Tar83] P. Taras *et al.*, The $8\pi$ Proposal, October 1983.
J.P. Martin *et al.*, Nucl. Instr. Meth. A257 (1987) 301.

[Twi83] P.J. Twin *et al.*, Nucl. Phys. A409 (1983) 343c-352c.

[Twi86] P.J. Twin et al., Phys. Rev. Lett. 57 (1986) 811.

[Vas70] D.G. Vass, Nucl. Instr. Meth. 86 (1970) 5-11.

[Vet00] K. Vetter *et al.*, Nucl. Instr. Meth. A452 (2000) 105-114 and Nucl. Instr. Meth. A452 (2000) 223-238.

[Vet01] K. Vetter *et al.*, Nucl. Phys. A582 (2001) 286c.

[Vol02] A. Volya *et al.* Phys. Rev. C 65 (2002) 054312-1.